Title

Ferroelectric Polarization in Perovskite Metal Oxide Photocatalysts and Photoelectrodes for Solar Water Splitting

Author

Assavachin, Samutr

Publication Date

2023

Ferroelectric Polarization in Perovskite Metal Oxide Photocatalysts and Photoelectrodes for Solar Water Splitting

By

SAMUTR ASSAVACHIN
DISSERTATION

Submitted in partial satisfaction of the requirements for the degree of

DOCTOR OF PHILOSOPHY

in

Chemistry

in the

OFFICE OF GRADUATE STUDIES

of the

UNIVERSITY OF CALIFORNIA

DAVIS

Approved:

Frank E. Osterloh, Chair

Susan M. Kauzlarich

Jesús M. Velázquez

Committee in Charge

2023

Acknowledgements

The research contained within this dissertation was made possible by the support of the National Science Foundation (grant CHE 1900136).

First, I would like to express my gratitude to Professor Frank E. Osterloh for providing me with the opportunity to join his research group and for his guidance, patience, and support. His mentorship has been instrumental to my development as a researcher and my personal growth. I admire his expertise and hope to one day become as venerated and knowledgeable as he is. I would like to acknowledge the contributions of Professor Susan M. Kauzlarich and Professor Jesús M. Velázquez as members of my dissertation committee. I would like to express my appreciation to Professor Louise Berben, Professor Jesús M. Velázquez, Professor David Britt, and Professor Yayoi Takamura for their contributions as members of my qualifying exam committee. I am grateful to my graduate advisor, Professor Alan Balch, and Brad Wolf for their encouragement which convinced me to persevere the PhD program. I would also like to thank Professor David T. Westmoreland and Professor Michelle Personick for their guidance during my undergraduate chemistry studies. Lastly, I extend my gratitude to Professor Davide Donadio for our collaboration projects.

To my parents, Prapasri Tapanakornvut and Thepnimitr Assavachin, I want to express my appreciation for your unconditional love throughout my life. I consider myself fortunate to be your child and I hope that I have made you proud. Your encouragement has been instrumental towards my success, and I am grateful for the values and guidance you have provided. To all my friends and family in Thailand, I am deeply grateful for your unwavering support and love. Nattha Nitiwarangkoon, your presence brings immense joy and inspiration to my life, and I am truly thankful for your care and affection that have helped me navigate life's challenges. Teerapat Anananuchatkul, Pongpat Thongpat, Jirasin Wattanatornpitak, Weeraya Rosendahl, and Saranda Lertsrijatuporn, I want to express my gratitude for your friendship and sincerity. I also want to extend my appreciation to the calisthenics community of Thailand, which reminds me of the importance of life beyond work. Mr. Jonathon Siminoe and Mr. Year Seraypheap, my high school teachers

who never gave up on me, I am grateful for your belief in me. To all my friends and family, though I cannot mention each of you by name, please know that I deeply value and cherish each and every one of you. Your presence and positivity have propelled me forward and instilled in me the determination to never give up.

To the Osterloh Lab, a cluster of camaraderie that endures the PhD emotional rollercoaster and propels each other to the glorious finish line. Kathleen Becker, I am immensely grateful for your friendship, support, and presence in my life. You are truly invaluable, and I am genuinely happy to have met you. Anna Kundmann, I hold you in high regard as a powerhouse of productivity, your dedication and proactiveness are truly inspiring. Rachel Doughty, thank you for your mentorship and guidance throughout my journey. Your support, both emotionally and intellectually, has been vital to me. Chengcan Xiao, your friendship and genuine sincerity mean a lot to me. Your advice and kindness have kept my research on track during tough times. I also want to extend my appreciation to Alex de Denko, Zeqiong Zhao, Ye Cheng, Ruirui Han, Sherdil Khan, Sahar Daemi, Tatiana Mamani, Andrew Li, Hervin Errol, Li Wang, Zainab Najaf, Mayha Salmanion, and Rajesh Kandel thank you for your help, advice, and for making the lab a vibrant and enjoyable environment. I cherish the memories we have made together.

To the Thai community of UC Davis, I want to express my deepest appreciation for providing me a sense of belonging with my time here. Nuchada Maneejantra, you have been like a sister to me, bringing everyone together and offering unwavering support, care, love, and guidance. Your presence has been a constant source of encouragement, especially during my toughest moments. Nalina Aiempichitkijkarn, Kreingkrai Nonkum, Supatirada Wongchanla, Siripat Watakajaturaphon, and Piyaporn Eiamcharoen, you are my second family, and I consider myself blessed to have the privilege of knowing each and every one of you. From the depths of my heart, thank you for being an integral part of my journey.

Last but not least, I want to thank me. I want to thank me for believing in me. I want to thank me for doing all this hard work. I want to thank me for having no days off. I want to thank me for never quitting. I want to thank me for always being a giver and trying to give more than I receive. I want to thank me for trying to do more right than wrong. I want to thank me for just being me at all times.

Ferroelectric Polarization in Perovskite Metal Oxide Photocatalysts and Photoelectrodes for Solar Water Splitting

Abstract

Solar water splitting offers a clean and renewable alternative to fossil fuel for energy production. This dissertation investigates a novel concept of utilizing ferroelectric polarization in photocatalysts to enhance overall solar water splitting activity. Our approach encompasses material synthesis, thin film fabrication, material doping, ferroelectric polarization, and surface photovoltage spectroscopy. Characterization mainly consists of electron microscopy, optical spectroscopy, powdered X-ray diffraction, and X-ray photoelectron spectroscopy. Photoelectrochemical activity is measured under simulated conditions using gas chromatography and electrochemistry. Our goal is to gain a better understanding of the origin of ferroelectrics in perovskite metal oxides and how it can alter photocatalytic activity, thereby improving the overall efficiency for solar water splitting.

In chapter 2, chromium-doped strontium titanate ($SrTiO_3$:Cr) nanocrystals of perovskite structure type and 45 nm (±15 nm) edge lengths were obtained by hydrothermal synthesis in water from titanium oxide, strontium hydroxide, and chromium(III) nitrate. According to XPS, the majority of the surface chromium (68.3%) is present in the 3+ state and the remainder (32.2%) in the 6+ state. Optical spectroscopy confirms a broad absorption at 2.3-2.9 eV from Cr^{3+} dopant states, in addition to the 3.2 eV band edge of the $SrTiO_3$ host. After modification with Pt nanoparticles, Cr-doped $SrTiO_3$ nanocrystals catalyze photochemical H_2 evolution from aqueous methanol under visible light illumination (>400 nm) and with an apparent quantum yield of 0.66 % at 435 nm. According to surface photovoltage spectroscopy (SPS), Cr-doped $SrTiO_3$ nanocrystals deposited onto gold substrates are n-type and have an effective band gap of 1.75 eV. SPS and transient illumination experiments at 2.50 eV reveal an anomalous surface photovoltage that increases with prior light exposure to values of up to -6.3 V. This photovoltage is assigned to ferroelectric polarization of

the material in the space charge layer at the Au/$SrTiO_3$:Cr interface. The polarization is stable for 24 h in vacuum but disappears after 12 h when samples are stored in air. The electric polarizability of $SrTiO_3$:Cr is confirmed when films are exposed to static electric fields (1.20 MV m^{-1}) in a fixed capacitor configuration. The discovery of a ferroelectric effect in Cr-doped $SrTiO_3$ could be significant for the development of improved photocatalysts for the conversion of solar energy into fuel.

In chapter 3, we demonstrate an unexpected ferroelectric effect in oxygen deficient $SrTiO_{3-x}$ and its application to improve photoelectrochemical water oxidation, a pathway to solar hydrogen fuel. After hydrogen-annealed $SrTiO_{3-x}$ is polarized under an electric field of 8.65 kV cm^{-1} under Ar flow the anodic water oxidation photocurrent is found to increase from 0.99 to 2.22 mA cm^{-2} at 1.23 V RHE (60 $mWcm^{-2}$, UV illumination), or to decrease to 0.50 mA cm^{-2}, for the opposite field orientation. The polarization also increases or decreases the surface photovoltage signal of the material and it modifies it flat band potential, based on Mott-Schottky measurements. These findings are attributed to the presence of an electric dipole near the $SrTiO_{3-x}$ surface, which modifies the potential drop across the depletion layer and affects the photochemical charge separation. Based on XPS, the electric polarization does not change the composition near the $SrTiO_{3-x}$ surface. Instead, the polarization effect is attributed to the electric field-induced migration of oxygen vacancies in $SrTiO_{3-x}$ surface region. This is supported by DFT calculations, which show that V_O transfer from the surface to the sub-surface layer strongly invert the electric dipole near the surface. Such a surface effect also explains the limited lifetime of the polarization effect and its dependence on the environment (24 h in air and 48 h under argon). The ability to induce an electrical polarization in a non-ferroelectric material after introduction of oxygen vacancies is of interest for solar energy conversion and information technology applications.

In chapter 4, the results of a systematic study on the facet-dependence of photoelectrochemical water oxidation with hydrogen annealed $SrTiO_3$ single crystals are demonstrated. After H_2 annealing, [100, 110, and 111] oriented $SrTiO_{3-x}$ single crystals exhibit variable water oxidation photocurrents (0.34, 0.82, 1.36 mA cm^{-2}, respectively) at 1.23 V versus RHE under UV illumination (60 mW cm^{-2}). The average

photocurrent onsets were observed at -0.172, -0.286, and -0.294 V RHE for [100], [110], [111] $SrTiO_{3-x}$ crystals, respectively. Surface photovoltage spectra of the crystals exposed to 0.50 M aqueous Na_2SO_4 show surface photovoltage signals of -0.31, -0.57, and -0.67 V for the [100], [110], [111] crystals respectively. Mott Schottky measurements in aqueous $K_{3/4}[Fe(CN)_6]$ show facet-dependent flatband positions of -0.60, -0.69, and -0.75 V RHE for the [100], [110], and [111] crystals respectively. These collective results confirm that the photoelectrochemical water oxidation performance of $SrTiO_{3-x}$ crystals is facet-dependent and controlled by the barrier height of the junctions at each facet. These results provide an explanation for the facet-dependent charge separation in $SrTiO_3$ photocatalysts.

In chapter 5, we demonstrate ferroelectric enhancement (FE) in photocatalytic hydrogen evolution and photoelectrochemical water oxidation with barium titanate nanocrystals. Nanocrystals of the ferroelectric tetragonal structure type were obtained by hydrothermal synthesis from TiO_2 and barium hydroxide in 63% yield. $BaTiO_3$ nanocrystal films on tantalum substrates exhibit water oxidation photocurrents of 0.141 mA cm^{-2} at 1.23 V RHE under UV light (60 mW cm^{-2}) illumination. Electric polarization at 80 kV cm^{-1} increases the photocurrent by a factor of 2 or decreases it by a factor of 3.5, depending on the field orientation. It also shifts the onset potential by -0.15 V or +0.09 V, depending on the polarity of the applied field, and it modifies the surface photovoltage signal. Lastly, exposure to an electric field increases the H_2 evolution rate of $Pt/BaTiO_3$ by a factor of ~1.5 and it raises the selectivity of photodeposition of silver onto the (001) facets of the nanocrystal. All FE enhancements can be removed by heating samples above the Curie temperature of $BaTiO_3$. These findings can be explained with FE dipole-induced changes to the potential drop across the space charge layer of the material. The ability to use the ferroelectric effect to enhance hydrogen evolution and water oxidation is of potential interest for the development of improved solar energy-to-fuel conversion systems.

Table of Contents

List of Figures

List of Tables

Chapter 1 – Introduction

1.1 Introduction to Solar Water Splitting

It is projected that global energy demand in 2050 will increase by 15 % from today.[1] To abide by the Paris Agreement: "to limit global warming to well below 2° Celsius and preferably limit it to 1.5° Celsius, compared to pre-industrial levels" will require an aggressive shift from fossil fuels to renewable energy. Earth's surface receives about 1.3 x 10^5 TW of solar energy annually, around 6,800 times more than the global demand, making solar energy one of the most abundant renewable energy source to be harnessed. Solar energy utilization involves three major components: solar capture, conversion, and storage. Photovoltaics (PVs) are the most common solar technology with monocrystalline silicon panels dominating the global market at over 20 % efficiency; multi-junction cells can even reach up to 47 % efficiency.[2] PVs require high purity light absorber materials that provide sufficient photogenerated charge carrier lifetimes for effective charge separation and collection on a macroscopic scale. Usage of solar electricity is also limited by the diurnal variations of local insolation and requires an efficient electric energy storage system. Given the projected five-fold increase in demand for lithium by 2030, solar electricity is unlikely going to be cost-competitive with fossil fuel due to its requirement for an effective energy storage system.[3] These obstacles must be overcome for PVs to successfully compete with fossil fuel.[4-5] An alternative solution for solar energy utilization is direct solar water splitting where solar energy electrolyzes water into hydrogen and oxygen gas (Equation 1.1).

$$H_2O_{(l)} \rightarrow H_{2\,(g)} + \tfrac{1}{2}\, O_{2\,(g)};\ \Delta G = +237\ \text{kJ} \bullet \text{mol}^{-1} \qquad (1.1)$$

In the early 1970s Fujishima and Honda demonstrated photoelectrochemical water splitting with a titanium oxide single crystal photoanode.[6]

Hydrogen, with its high energy density of 143 MJ kg^{-1}, offers a viable solution for overcoming the challenges associated with electrical storage in batteries. Its ability to be stored, transported, and utilized in a variety of industrial processes, including liquid fuel production, hydrogenation of aromatic compounds, direct reduction of iron, and green ammonia production, makes it a versatile and convenient energy carrier. [7-11] It is important to note that hydrogen has a low volumetric energy density and requires pressurization to achieve the desired energy storage capacity. The United States Department of Energy (US DOE) has estimated the required cost of hydrogen to be \$2.00 - \$4.00 per kilogram H_2 to serve as an economically viable fuel source to compete with fossil fuel. [12]

Four types of reactors have been proposed as solar hydrogen production systems (**Figure 1.1**). [13] Type I and II reactors employ photocatalyst suspensions in plastic bags, which reduce capital costs and can potentially achieve the target hydrogen price of \$2.00 - \$4.00 per kilogram. However, these systems raise safety concerns due to the congregation of H_2 and O_2 gases. Type III reactors utilize photoelectrochemical systems based on a fixed planar configuration (assuming a solar-to-hydrogen (STH) efficiency of 10 % and a ten-year lifetime), resulting in a hydrogen price of \$10.4 per kilogram. On the other hand, Type IV reactors are planar systems equipped with tracking solar concentrator arrays, which set the hydrogen price at \$4.0 per kilogram (assuming a STH efficiency of 15 % and a ten-year lifetime). Although Type III and IV systems have higher capital costs (\$10.40 and \$4.10 per kilogram, respectively), the use of improved materials can potentially reduce prices.

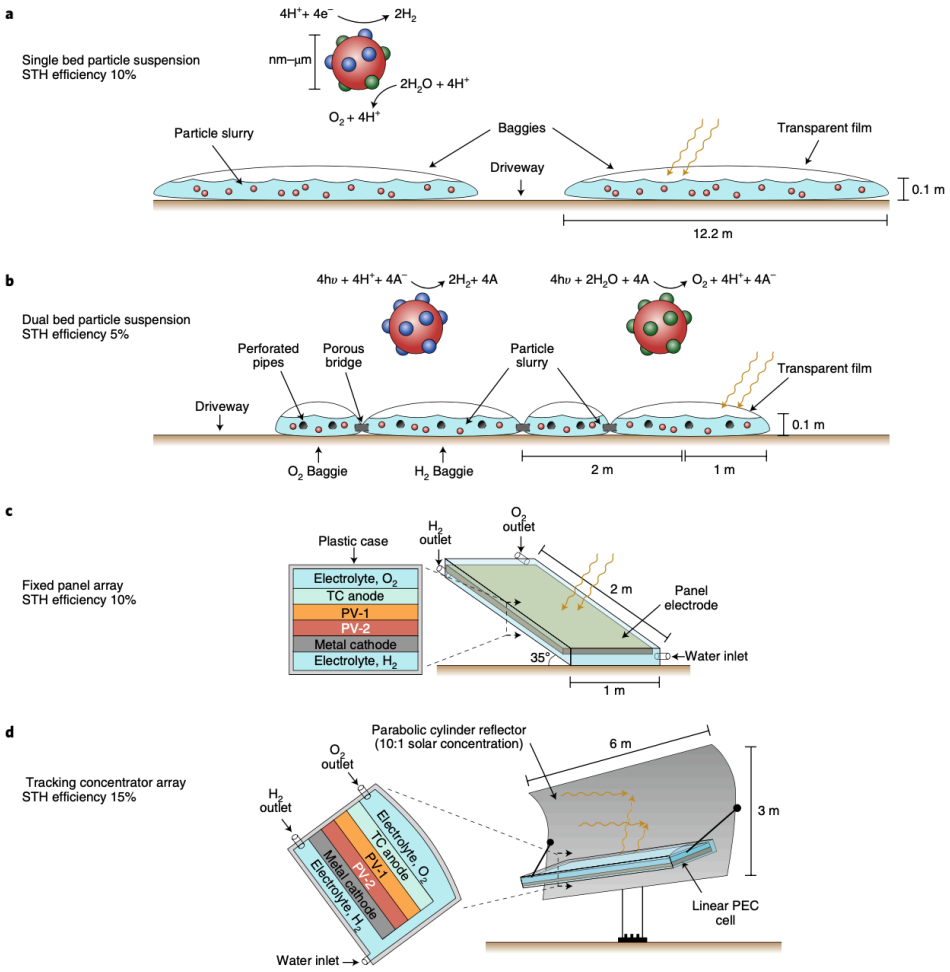

Figure 1.1. Schematics of four reactor types. a) Type I reactor cross-section showing the particle slurry contained within bags separated by an access driveway. b) Type II reactor cross-section showing the particle slurries contained within bag assemblies with alternating full and half size bags for H_2 and O_2 evolution. c) Type III reactor design showing the encased composite panel oriented toward the sun with buoyant separation of gases. d) Type IV reactor design with an offset parabolic cylinder receiver that concentrates sunlight onto a linear photoelectrochemical (PEC) cell. Drawings not to scale. Used with permission of Royal Society of Chemistry, from *Technical and economic feasibility of centralized facilities for solar hydrogen production via photocatalysis and Photoelectrochemistry*, Pinaud et al., *6*, **2013**; permission conveyed through Copyright Clearance Center, Inc. [13]

Despite the simplicity of Type I and II reactors, they suffer from significant drawbacks, including: i) the lack of efficient photocatalysts with long lifetimes, ii) the need for H_2 and O_2 gas separation systems and the associated safety risks, which can increase capital costs, and iii) mass transport issues with particle suspensions. Type IV reactors are considered ideal; however, the increased capital costs for solar concentrators and tracking systems can compromise the total electricity output, which is why a STH efficiency of 15% is required. Type III reactors represent the most viable approach due to their straightforward construction and the balance they strike between cost, efficiency, and scalability.

Japan stands as the first country to demonstrate a remarkable proof-of-concept for panel-type III reactors, successfully scaling up Type III reactors to 1.0 m^2 in 2018, as shown by Goto et al. [14] Photocatalytic water splitting was accomplished under natural sunlight with a STH efficiency of 0.4 %. The system utilized a particulate $RhCrO_x/SrTiO_3$:Al photocatalyst with an apparent quantum yield (AQY) of 56 % at 365 nm, fixed onto flat sheets applied onto the panel reactor (**Figure 1.2**). However, a 60 % loss of activity was observed after 6 hours, highlighting the need to enhance STH efficiency by developing higher efficiency and narrower bandgap photocatalysts. Later in 2021, the system was successfully scaled up to 100 m^2 reaching maximum STH efficiency of 0.76 %. [15] After 7 months of operation under outdoor insolation of 7.6 kWh m^{-2} per day STH efficiency remained above 0.40 % over 1,600 hours.

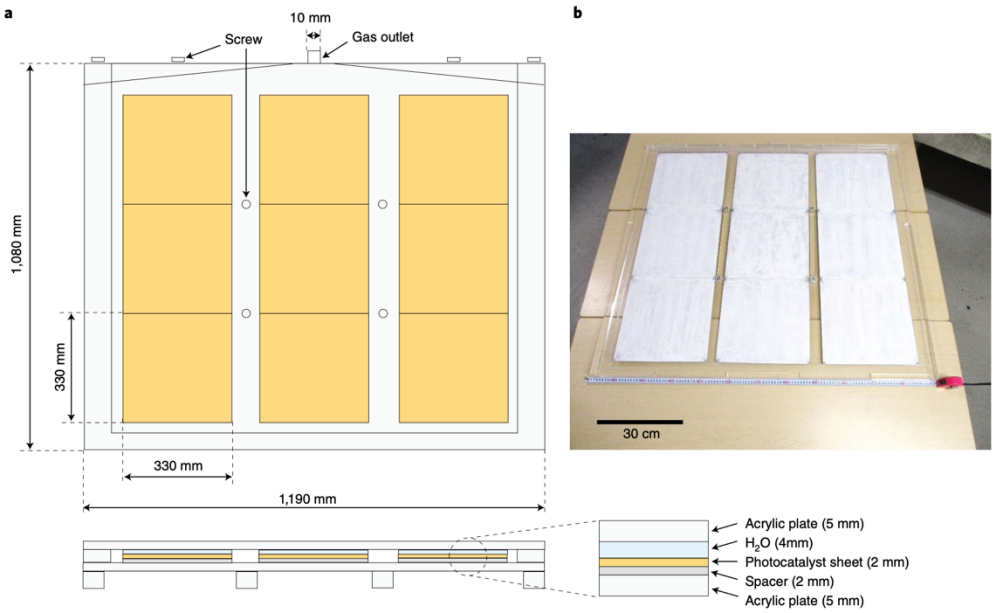

Figure 1.2. a) Schematics of the 1 x 1 m water-splitting panel. Nine photocatalyst sheets of 33 x 33 cm each were arrayed in the reactor. A hydrophilized acrylic plate was used as the window. The panel had a 10º tilt. The weight of water in this panel was approximately 4 kg because a surplus depth of 4 mm was adopted in consideration of the distortion of the panel under its own weight. b) A photograph of a 1 x 1 m $SrTiO_3$:Al panel. Reprinted from Joule, 2 (3), Goto et al., *A Particulate Photocatalyst Water-Splitting Panel for Large-Scale Solar Hydrogen Generation*, p. 509-520, Copyright© 2017, with permission from Elsevier. [14]

In the past decade, significant progress has been made in research aimed at improving photocatalysts for photoelectrochemical (PEC) systems. In 2015, Juan Liu et al. reported the fabrication of a carbon nanodot-carbon nitride (C_3N_4) composite photocatalyst with a STH efficiency of 2.0 % and quantum efficiency (QE) of 16 % and 6.3 % at 420 nm and 580 nm, respectively. [16] This photocatalyst possessed the advantage of a wider bandgap, extending up to 620 nm, which maximized solar spectrum absorption. It also demonstrated the ability to achieve solar water splitting from seawater, although its overall activity in seawater decreased, resulting in a STH efficiency of 0.45 % and QE_{420nm} of 3.86 %. Additionally, the photocatalyst exhibited a

robust lifetime of over 200 days under active solar water splitting. In 2019, P. Varanda et al. utilized the epitaxial lift-off and transfer technique to fabricate an inverted tandem device of InGaP/GaAs cells, resulting in a STH efficiency of 6 % and a lifetime of over 150 hours. [17] This achievement is an improvement for unassisted solar water splitting device, but the output of oxygen declined after two hours due to photoelectrode corrosion.

In 2020, the Domen group achieved a milestone by reporting the first photocatalyst with an external quantum efficiency (EQE) of unity at 350 nm. [18] This means that every electron-hole pair generated from photoexcitation successfully participates in proton reduction and water oxidation. The result was accomplished through several key advancements: i) Defect removal by aluminum doping: Through the introduction of aluminum (Al^{3+}) doping and flux synthesis, the complete removal of Ti^{3+} defect states was achieved. This defect removal process minimized charge recombination and resulted in highly faceted particles. ii) Synthesis of faceted photocatalysts: The controlled synthesis of faceted photocatalysts played a crucial role in enhancing the overall performance. The faceted structure further reduced charge recombination and improved the efficiency of the photocatalyst. iii) Selective co-catalyst deposition: By depositing specific co-catalysts (Rh/Cr_2O_3 for hydrogen evolution and CoOOH for oxygen evolution) with spatial separation of the redox sites, recombination and back reaction are mitigated allowing optimal performance. This precise co-catalyst deposition, enabled by photoirradiation, contributed to the EQE of unity. However, despite these advancements, the large bandgap of $SrTiO_3$ (3.2 eV) limited the solar-to-hydrogen (STH) efficiency to only 0.65 % under 1 sun illumination. Although the Domen group's previous study demonstrated the stability of Al-doped $SrTiO_3$ with a lifetime exceeding 1,000 hours (~41 days), the activity drop observed was attributed to the dissolution of co-catalysts. [19] It is important to note that this system represents a type I reactor with a particulate suspension, and while the lifetime is noteworthy, the achieved STH efficiency of 0.65 % falls significantly short of the DOE's target efficiency of 10 % necessary to meet the hydrogen price goal.

In 2021, Ekspong et al. reported a STH efficiency of 13.8% using a NiFeMo electrocatalyst coupled with solution-processed perovskite solar cells, which is one of the highest reported values to date. [20] Although the high STH efficiency surpasses the DOE's target for cost-competitive hydrogen devices, challenges arise from the complex fabrication process and the lack of information on the device lifetime. In 2023, Peng Zhou et al. successfully developed an InGaN/GaN type III device for solar water splitting. [21] This device achieved a STH efficiency of 9.2 % in pure water over a duration of 74 hours. The higher STH efficiency was partly attributed to the device operating temperature of 70°C which increases overall water splitting activity. Additionally, the device is capable of overall water splitting in tap water and sea water achieving STH efficiencies of 7.4 % and 6.6 % over 10 hours respectively. Despite recent developments, the lifetime, stability, and cost of these devices are still lagging behind the DOE mandated goal requiring further research in photoelectrochemical (PEC) and photocatalytic water splitting.

1.2 Introduction to Ferroelectric Materials

Ferroelectric materials belong to a subgroup of dielectric materials known as piezoelectrics and pyroelectrics. These materials exhibit spontaneous electric polarization, which can be reversed and reoriented by an external applied electric field, as depicted in the classic hysteresis loop (**Figure 1.3**). [22] In contrast, paraelectric and dielectric materials experience polarization (P) only in the presence of an applied electric field (E), and this polarization disappears once the field is removed. The discovery of the first ferroelectric material was made by Joseph Valasek, who identified it in Rochelle salt ($KNaC_4H_4O_6 \cdot 4H_2O$) in 1920. [23] A significant breakthrough in ferroelectric research occurred during World War II in 1944 when barium titanate ($BaTiO_3$) was discovered, showcasing a high dielectric constant (4,000) and subsequently finding immediate applications in sonar technology. [24]

The polarizable characteristic of ferroelectric materials arises from their transition between a high-temperature, high-symmetry paraelectric phase and a low-temperature, low-symmetry ferroelectric phase. The temperature at which this transition occurs is known as the Curie temperature (T_C). Additionally, phase transitions can also occur by film straining or ionic substitution (**Figure 1.3**). [25,26] In a cubic ABO_3 perovskite structure, the centrosymmetric unit cell does not exhibit a dipole moment. However, when the B-site is substituted, structural distortion can occur, leading to the development of a ferroelectric dipole. Ferroelectric materials belong to one of the 10 polar point groups, which encompass 68 polar space groups. Among them, 88 point groups can potentially undergo paraelectric-to-ferroelectric phase transitions, as shown in **Table 1.1**. [27, 28]

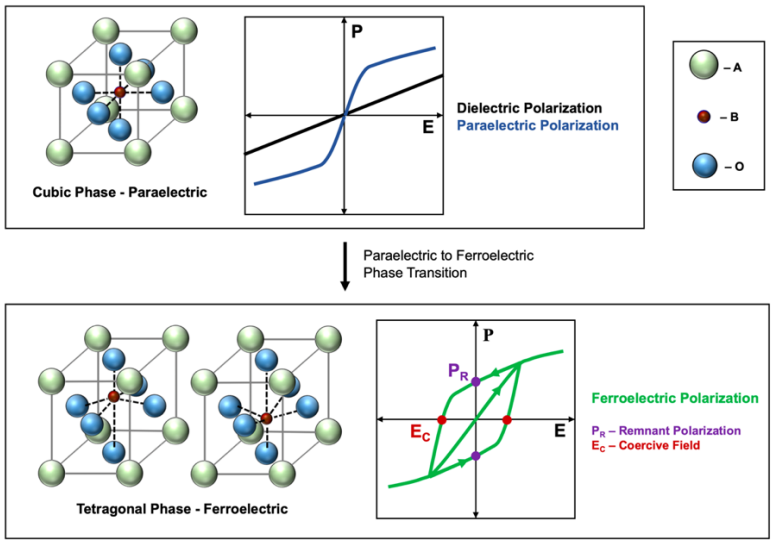

Figure 1.3. High-to-low symmetry transition in ABO_3 perovskite from the cubic phase (paraelectric; top) to the tetragonal phase (ferroelectric; bottom) with corresponding hysteresis loops. P – polarization. E – applied electric field. P_R – Remnant polarization. E_C – Coercive field.

Table 1.1. a) 68 ferroelectric space groups belonging to the 10 polar point group. b) 88 species of potential paraelectric-to-ferroelectric phase transitions. Used with permission of Royal Society of Chemistry, from *Symmetry breaking in molecular ferroelectrics*, Shi P. P. et al., *45*, **2016**; permission conveyed through Copyright Clearance Center Inc. [27]

Table 1.1a

Point group	Space group
C_1	*P*1
C_2	*P*2, $P2_1$, *C*2
C_{1h}	*Pm*, *Pc*, *Cm*, *Cc*
C_{2v}	*Pmm*2, $Pmc2_1$, *Pcc*2, *Pma*2, $Pca2_1$, *Pnc*2, $Pmn2_1$, *Pba*2, $Pna2_1$, *Pnn*2, *Cmm*2, $Cmc2_1$, *Ccc*2, *Amm*2, *Abm*2, *Ama*2, *Aba*2, *Fmm*2, *Fdd*2, *Imm*2, *Iba*2, *Ima*2
C_4	*P*4, $P4_1$, $P4_2$, $P4_3$, *I*4, $I4_1$
C_{4v}	*P*4*mm*, *P*4*bm*, $P4_2cm$, $P4_2nm$, *P*4*cc*, *P*4*nc*, $P4_2mc$, $P4_2bc$, *I*4*mm*, *I*4*cm*, $I4_1md$, $I4_1cd$
C_3	*P*3, $P3_1$, $P3_2$, *R*3
C_{3v}	*P*3*m*1, *P*31*m*, *P*3*c*1, *P*31*c*, *R*3*m*, *R*3*c*
C_6	*P*6, $P6_1$, $P6_5$, $P6_2$, $P6_4$, $P6_3$
C_{6v}	*P*6*mm*, *P*6*cc*, $P6_3cm$, $P6_3mc$

Table 1.1b

Triclinic	$\bar{1}F1$ (1)[a]
Monoclinic	*2F*1 (2/2); *mF*1 (2/2); 2/*mF*1 (2); 2/*mFm* (1); 2/*mF*2 (1)
Orthorhombic	222*F*1 (4/2); 222*F*2 (1); *mm*2*F*1 (4/2); *mm*2*Fm* (2/2); *mmmF*1 (4); *mmmFm* (2); *mmmFmm*2 (1)
Tetragonal	4*F*1 (4/2); $\bar{4}F1$ (4/2); $\bar{4}F2$ (1); 4/*mF*1 (4); 4/*mFm* (2); 4/*mF*4 (1); 422*F*1 (8/2); 422*F*2(*s*) (2); 422*F*4 (1); 4*mmF*1 (8/2); 4*mmFm* (4/2); $\bar{4}2mF1$ (8/2); $\bar{4}2mF2(s)$ (2); $\bar{4}2mFm$ (4/2); $\bar{4}2mFmm2$ (1); 4/*mmmF*1 (8); 4/*mmmFm*(*s*) (4); 4/*mmmFm*(*p*) (4); 4/*mmmFmm*2(*s*) (2); 4/*mmmF*4*mm* (1)
Trigonal	3*F*1 (3/2); $\bar{3}F1$ (3); $\bar{3}F3$ (1); 32*F*1 (6/2); 32*F*2 (3/2); 32*F*3 (1); 3*mF*1 (6/2); 3*mFm* (3/2); $\bar{3}mF1$ (6); $\bar{3}mF2$ (3); $\bar{3}mFm$ (3); $\bar{3}mF3m$ (1)
Hexagonal	6*F*1 (6/2); $\bar{6}F1$ (6/2); $\bar{6}Fm$ (3/2); $\bar{6}F3$ (1); 6/*mF*1 (6); 6/*mFm* (3); 6/*mF*6 (1); 622*F*1 (12/2); 622*F*2(*s*) (3); 622*F*6 (1); 6*mmF*1 (12/2); 6*mmFm* (6/2); $\bar{6}m2F1$ (12/2); $\bar{6}m2Fm(s)$ (6/2); $\bar{6}m2Fm(p)$ (6/2); $\bar{6}m2Fmm2$ (3/2); $\bar{6}m2F3m$ (1); 6/*mmmF*1 (12); 6/*mmmFm*(*s*) (6); 6/*mmmFm*(*p*) (6); 6/*mmmFmm*2(*s*) (3); 6/*mmmF*6*mm* (1)
Cubic	23*F*1 (12/2); 23*F*2 (3); 23*F*3 (4/2); $m\bar{3}F1$ (12); $m\bar{3}Fm$ (6); $m\bar{3}Fmm2$ (3); $m\bar{3}F3$ (4); 432*F*1 (24/2); 432*F*2(*s*) (6); 432*F*4 (3); 432*F*3 (4); $\bar{4}3mF1$ (24/2); $\bar{4}3mFm$ (12/2); $\bar{4}3mFmm2$ (3); $\bar{4}3mF3m$ (4/2); $m\bar{3}mF1$ (24); $m\bar{3}mFm(s)$ (12); $m\bar{3}mFm(p)$ (12); $m\bar{3}mFmm2$ (6); $m\bar{3}mF4mm$ (3); $m\bar{3}mF3m$ (4)

[a] *F* indicates the paraelectric-to-ferroelectric phase transition, while *p* and *s* indicate that the symmetry elements of the ferroelectric phase correspond to the principal and side symmetric axes in the paraelectric phase, respectively. State numbers are included in the round brackets, while the simple numbers represent reversible ferroelectrics. The number 1 belongs to 18 types of uniaxial ferroelectrics, and numbers greater than 1 are the sums of equivalent polar directions of multiaxial ferroelectrics. Besides, for complex state numbers such as "3/2", "4/2" and so on, the common number 2 on the right of the forward slash indicates reorientable ferroelectrics, whereas the numbers on the left of it denote the sums of equivalent polar directions.

The anomalous photovoltage effect refers to a phenomenon in which the photovoltage generated in a semiconductor exceeds its bandgap. [29-32] This anomalous photovoltage effect is recognized as a characteristic feature in ferroelectric materials and has prompted studies investigating this effect in various semiconductors. [33-37] In a ferroelectric material, individual ferroelectric domains can be considered as p-n junctions with their own ferroelectric dipoles. The separation of photogenerated charge carriers within each domain leads to the generation of a photovoltage. When the contributions from each domain are accumulated, a net open circuit potential (V_{OC}) can be achieved that exceeds the bandgap energy. Additionally, the direction of polarization in the material can be controlled by an external electric field, allowing for the modulation of photocurrent, either enhancing or suppressing it. [38-40] Enhancing photovoltage is a desirable goal for improving the efficiency of photocatalysts, as it leads to increased electric power output. We propose integrating ferroelectric polarization with photocatalysts as a strategy to improve overall efficiency.

1.3 Ferroelectric Polarization for Enhanced Photocatalytic Activity

To achieve higher photocatalyst efficiency, it is crucial to address the factors contributing to efficiency loss. The photocatalytic reaction involves several interconnected processes, including light absorption, charge separation, charge transport, charge transfer, surface reactions, and mass transport of reactants and products. Photocatalysts are typically nanoscale materials with distributed cathodic and anodic sites on their surfaces (**Figure 1.4**).

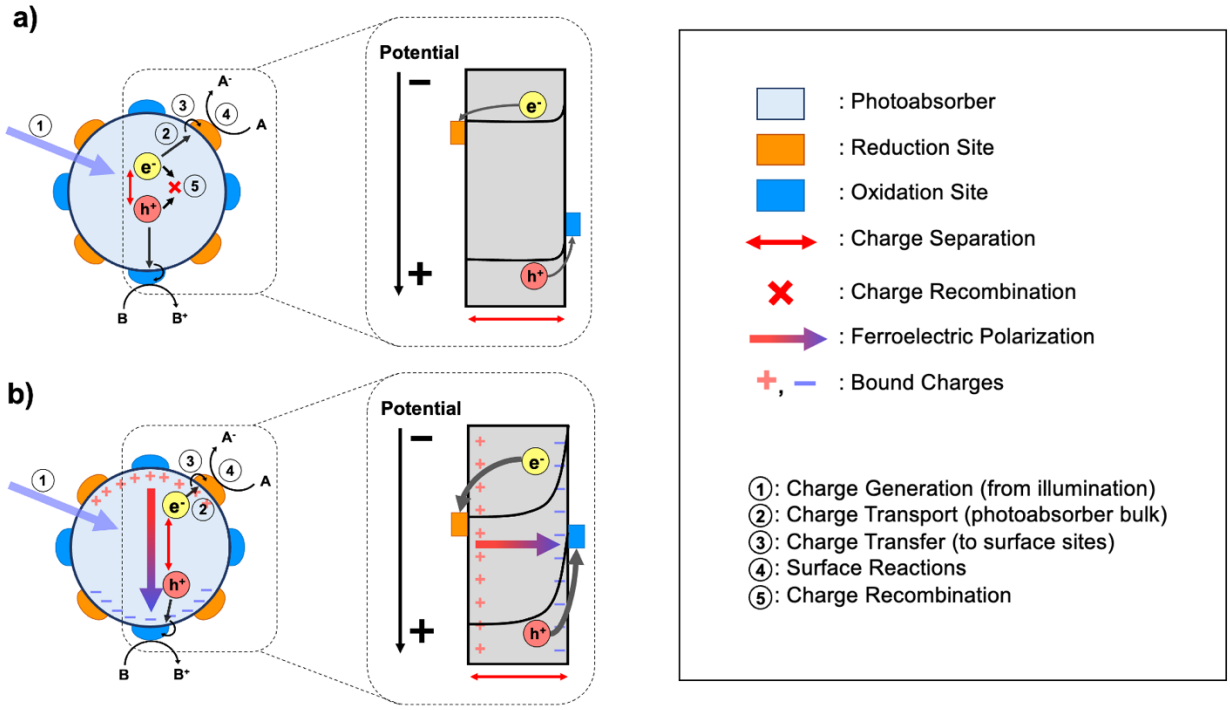

Figure 1.4. a) A photocatalyst with surface reductive and oxidative sites in an aqueous solution. The red arrow indicates the charge-separation direction between the two surface sites. The red "**X**" indicates carrier recombination in the bulk resulting in loss of efficiency. b) A ferroelectric photocatalyst with ferroelectric polarization resulting in an internal electric field (red to purple shaded arrow) and the bound charges (+, -) on the surfaces as a result of polarization. Band energetics for each system are shown in the dashed box region. Ferroelectric polarization increases the Schottky barrier and the internal electric field of the

photocatalyst resulting in enhanced carrier separation and reduced charge recombination. Adapted with permission from Yanagi et al.; *ACS Energy Letters*, **2022**, *7*, page 432−452. Copyright© 2022, American Chemical Society. [43]

In an ideal scenario, illumination initiates charge generation, followed by selective charge transfer to the respective reaction sites. However, the shortened distance across the photocatalyst can make charge separation and transfer processes problematic. [41, 42] As size decreases, the distance between electron-hole carriers diminishes, increasing the probability of recombination. In addition, reduced distance between surface redox sites relative to the carrier diffusion length contributes to increased surface trapped states and enhanced backward reactions. In the absence of an internal electric field, diffusion dominates charge carrier transport, resulting in more frequent recombination. [43, 44] Various approaches have been explored to enhance carrier separation and minimize charge recombination in photocatalytic systems. These include solid-solid junctions, [45, 46] crystal facets, [18, 47] and the use of co-catalysts. [48-50] In our research, we propose an alternative strategy to use the ferroelectric polarization to amplify the internal electric field within a photocatalyst to maximize carrier separation.

As discussed in Chapter 1.2, ferroelectric materials possess spontaneous electric polarization that can be controlled by an applied electric field. By inducing ferroelectric polarization in a photocatalyst, the internal electric field can enhance the separation of electrons and holes, thereby reducing charge recombination. This effect is illustrated in **Figure 1.4b**. Recent research has investigated the use of ferroelectric photocatalysts as an approach to improve overall catalytic reactions. [51,52] However, there is scarce research regarding the quantitative and direct correlations between ferroelectric polarization and photochemical energy conversion. Although studies on ferroelectric polarization in photocatalysts are available, further

research is needed to establish clear relationships between ferroelectric polarization and its effect on photocatalytic water splitting reactions.

1.4 Surface Photovoltage Spectroscopy

When a metal and a semiconductor are in contact, free electrons are transferred from the material with the lower work function to the higher work function. For contact between a metal (or surface states) and an n-type semiconductor (where electrons are majority carriers) where work function of the metal is higher than that of the semiconductor, electron flows from the semiconductor to the metal until the Fermi level of both materials are aligned (**Figure 1.5a**). [53, 54] This alignment results in an upward band bending at the surface of the semiconductor due to the low concentration of free charge carriers. The electric field at the interface cannot be effectively screened, leading to a depletion of free charge carriers near the semiconductor surface compared to the bulk. This depletion creates a Schottky barrier, accompanied by a potential drop across the region known as the space charge region (SCR). [54-56] Illumination causes the bands to flatten as the negative surface charge decreases due to the transport of holes to the surface (**Figure 1.5b**). Conversely, in a p-type semiconductor with downward band bending, illumination moves electrons toward the surface and reduces the downward band bending. The change in surface potential induced by illumination is referred to as Surface Photovoltage (SPV), and its magnitude is influenced by the intensity of the incident light. As the light intensity increases, the energy bands become completely flattened, and the saturated SPV value corresponds to the initial magnitude of band bending in the dark (**Figure 1.5c)**. [57]

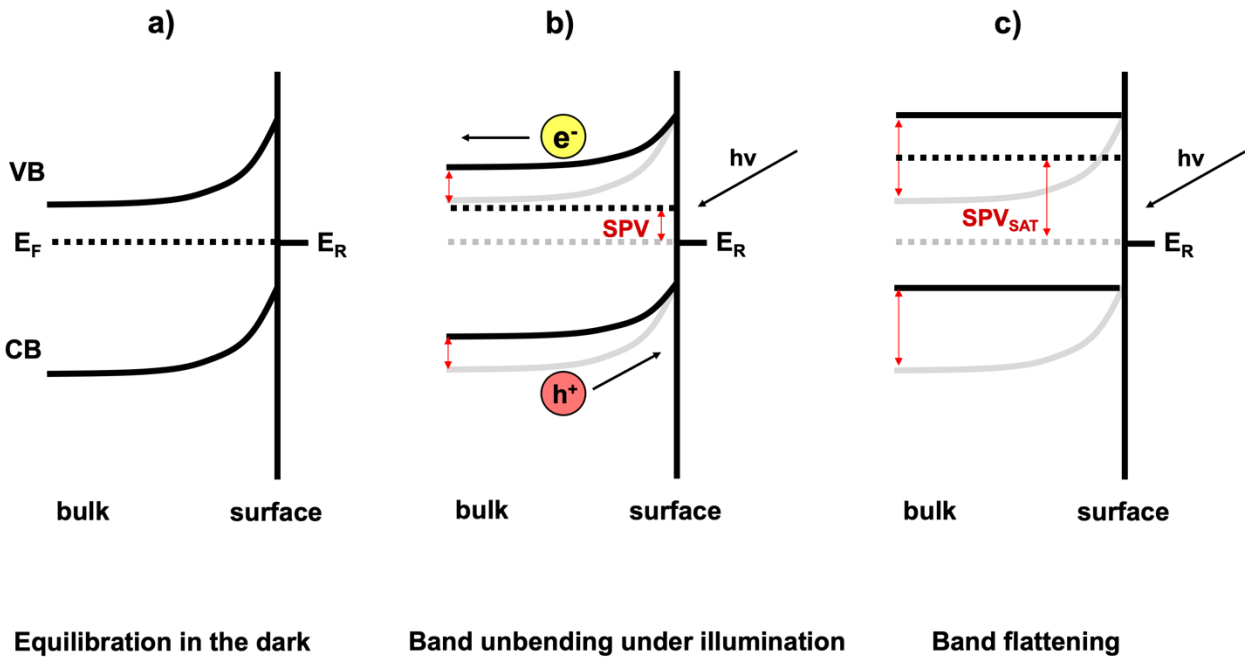

Figure 1.5. Schematic diagrams of the surface photovoltage effect. (a) Upward band bending in n-type semiconductor; (b) absorbed photons produce free charge carriers resulting in a partial band flattening; (c) largest possible SPV (saturation SPV) occurs with completely flatten bands. Grey line shows the upward band bending under equilibration in the dark. E_R is a surface state in equilibration with the Fermi level of the semiconductor, E_F. Adapted with permission from Zhang Z. and Yates Jr. J. T.; *Chemical Reviews*, **2012**, *112*, page 5520-5551. Copyright© 2012 American Chemical Society. [53]

Vibrating Kelvin probe surface photovoltage spectroscopy (SPS) is sensitive, contactless, and non-destructive technique used for semiconductor characterization. It relies on changes in contact potential induced by illumination. [58, 59] The Kelvin probe measures the work function difference between two materials after making an electrical contact. Before contact, both metals are electrically neutral, and share the same local vacuum level (**Figure 1.6a**). When contact is established, charge flows from the metal with a smaller work function to the one with a larger work function until the Fermi levels become equal. [53, 58, 59]

This charge transfer creates an electrical potential difference across the gap of the parallel capacitor (**Figure 1.6b**). The potential difference is called the contact potential difference (CPD) (Equation 1.2).

$$eV_{CPD} = W_1 - W_2 \tag{1.2}$$

Lord Kelvin suggested an accurate measurement of the CPD by directly applying an external DC bias, equal and opposite to the CPD, to the capacitor (**Figure 1.6c)**. [57] The applied bias will discharge the capacitor and restore the Fermi level of the two metals to their original positions. The applied bias required to completely discharge the capacitor can be used to accurately determine the CPD. This type of arrangement is known as the Kelvin probe method, after its inventor.

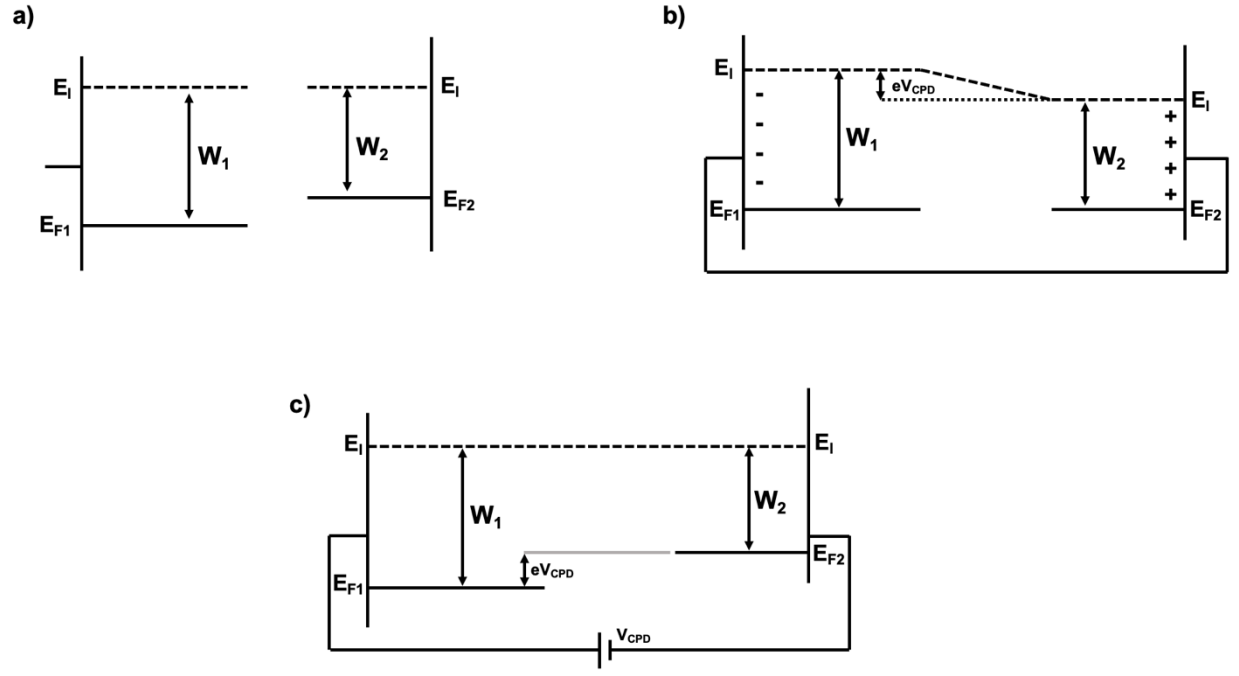

Figure 1.6. Schematic energy diagram for two different metals: a) isolated, b) short-circuited, c) connected through a DC bias equal and opposite to the contact potential difference. W_1, E_{F1} and W_2, E_{F2} are work

function and fermi level of material 1 and 2 respectively. eV_{CPD} is the CPD between the two materials in units of electron volts. E_l is the local vacuum energy level. The + and – are bound charges. Reprinted from *Surface Science Reports*, *37*, Kronik L. and Shapira Y., Surface photovoltage phenomena: theory, experiment, and applications, page 1-206, Copyright© 1999, with permission from Elsevier. [57]

The SPS technique measures the CPD between a sample and reference material in the dark and under illumination. Thus, surface photovoltage (SPV) can be calculated as the following (Equation 1.3):

$$SPV = CPD_{illumination} - CPD_{dark} \quad (1.3)$$

The vibrating Kelvin probe technique consists of a semitransparent gold mesh placed approximately 1 mm above a grounded sample film (**Figure 1.7)**. Surface photovoltage is measured by illuminating the sample with monochromatic light of varying wavelength through the Kelvin probe. The SPV corresponds to the light-induced change of the CPD of the semiconductor, assuming the work function of the reference electrode in the dark and under illumination are equal. This carrier separation can also be described as changes in surface dipoles. ΔCPD describes the separation of photogenerated electrons and holes toward the surface and back contact, respectively (ΔCPD >0), or towards the back contact and surface, respectively (ΔCPD <0).

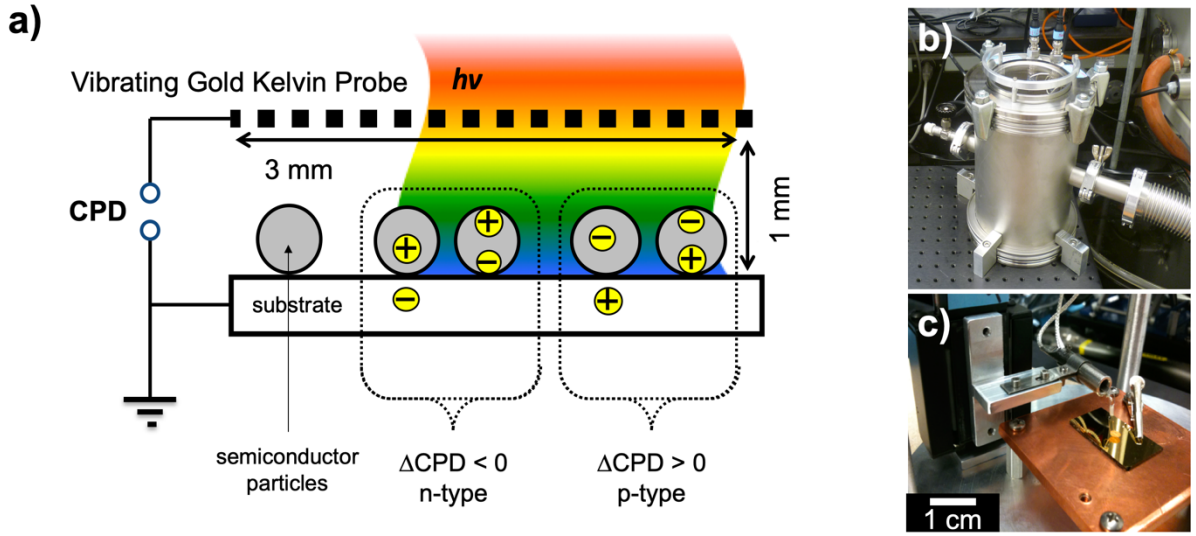

Figure 1.7. a) Surface photovoltage spectroscopy (SPS) schematics. b) SPS chamber for vacuum environment. c) Experimental set up with gold-coated glass substrate on a copper stage using a stainless-steel alligator clip contact. Vibrating Kelvin probe is located 1 mm above the gold substrate. Reprinted with permission from Osterloh F. E. et al.; *Journal of Physical Chemistry C*, **2014**, *118*, 14723−14731. Copyright© 2014 American Chemical Society. [60]

The application of SPS includes probing the bandgap, identifying semiconductor type, and identification of defects or dopant states. For example, in the case of bismuth vanadate ($BiVO_4$) with Co_3O_4 cocatalyst, the improved photocatalytic water oxidation (17-fold enhancement) was correlated with an observed increase in SPV signal caused by improved hole transfer into the cocatalyst. [61] The chemically deposited cocatalyst forms a $BiVO_4$-Co_3O_4 junction, facilitating electron-hole separation and hole accumulation at the film surface.

The SPV technique has also been applied to investigate the effects of transition metal dopants (Fe, Rh, Cu, Mn, Ni) in strontium titanate ($SrTiO_3$) on the bandgap. Distinct sub-bandgap onset signals were observed for each dopant. These SPV signals correspond with the optical bandgap determined through Kubelka-Munk absorption spectroscopy. [62] The SPS technique was also demonstrated for the calculation of the space charge region (SCR) width in different semiconducting materials such as $SrTiO_3$, $SrTiO_3$:Al, and GaAs. [63] By reducing the film thickness, the SPV signal proportionally decreases and inverts in direction. At the thinnest film, complete signal inversion occurs, indicating that the entire film becomes the inversion region, allowing for the extraction of SCR width information from the SPV data.

Overall, SPS is a highly sensitive and non-destructive technique with broad versatility in semiconductor characterization. It serves as a valuable tool for the study of semiconducting materials. However, the SPV signal can be influenced by impurities, surface states, defects, dopants, and other factors. To ensure accurate interpretation, it is highly recommended to analyze SPV data synergistically with other techniques to verify the obtained results.

1.5 Overview

Ferroelectric polarization has the potential to enhance photoelectrochemical (PEC) and photocatalytic overall solar water splitting processes. However, most reported ferroelectric systems have flaws such as relying on dye degradation reactions to demonstrate photocatalytic activity, using separate components for ferroelectricity and PEC, and employing polarization conditions that induce chemical changes in the samples. [35, 38, 39, 52, 65-67] The objective of this dissertation is to investigate well-defined systems and demonstrate the enhancement of solar water oxidation and hydrogen generation using ferroelectric semiconductors. In Chapter 2, the anomalous photovoltage effect of chromium-doped strontium titanate

($SrTiO_3$:Cr) and the influence of applied polarization on charge carrier dynamics are investigated using SPS. Doping strontium titanate can lead to visible light active properties and improvements in photocatalytic activity. [18, 19, 62, 64] In this study, we explore the potential ferroelectric response induced by chromium substitution with titanium ions. However, due to additional defects introduced by the chromium dopant (Cr^{6+} and oxygen vacancies), a simpler system is pursued in Chapter 3.

In chapter 3, we investigate a possible ferroelectric effect through symmetry distortion by formation of oxygen vacancies in $SrTiO_3$ single crystals. The impact of electric field-induced polarization on PEC water oxidation and changes in carrier dynamics is quantified using SPS. Mott Schottky measurements are also employed to understand the changes in the flat band potential of the material resulting from polarization effects. This has led to the investigation of crystal facet effects, which is further studied in chapter 4. Three exposed surface facets ([100], [110], [111]) of $SrTiO_3$ single crystals are studied to elucidate their effects on water oxidation activity. The goal is to isolate the facet effects from other factors such as co-catalysts, dopants, and defect states in order to investigate the origin of facet-dependent activity. Photoelectrochemical (PEC) measurements are employed to compare the activity differences in water and methanol oxidation, aiming to determine whether kinetics play a role. Mott Schottky and impedance measurements are conducted to assess the flat band potential and resistivity of each facet. Additionally, SPS is utilized to investigate the band bending characteristics of each facet, providing insights into the reasons behind the observed variations in water oxidation activity among different facets.

Finally in chapter 5, $BaTiO_3$ is selected as a model photocatalyst due to its ferroelectric properties at room temperature. [33, 51, 65, 66] To the best of our knowledge, no previous study has demonstrated the ferroelectric enhancement for water oxidation and H_2 evolution using $BaTiO_3$ nanocrystals as the photocatalyst. The goal is to provide a proof-of-concept for enhancement in solar water oxidation and H_2 generation using

$BaTiO_3$. Hydrothermal synthesis approach is improved to produce well-faceted uniform particles with tetragonal structure. Ferroelectric enhancement is explored in particle suspensions and particle films for PEC water oxidation and H_2 evolution respectively. Silver photoreduction is also used to elucidate the effects of polarization on modulating the internal electric field of the material to explain the ferroelectric effect. We hope this work will help contribute to the imperative transition from fossil fuel to a greener and more sustainable renewable energy source.

1.6 References

1. Exxon Mobil Outlook for Energy: A Perspective to 2050 (Exxon Mobil) **2022**.

2. NREL: Best Research-Cell Efficiency Chart (National Renewable Energy Laboratory, **2022**).

3. IEA, Lithium production, **2021**, and projected demand in climate-driven scenarios, 2030, IEA, Paris. *https://www.iea.org/data-and-statistics/charts/lithium-production-2021-and-projected-demand-in-climate-driven-scenarios-2030*

4. Lewis N. S., Nocera D. G.; Powering the Planet: Chemical Challenges in Solar Energy Utilization. *Proceedings of the National Academy of Sciences* **2006**, *103* (43), 15729-15735.

5. Lewis, N. S., Crabtree G., Nozik A. J., Wasielewski M. R., Alivisatos P., Kung H., Tsao J., Chandler E., Walukiewicz W., Spitler M., Ellingson R., Overend R., Mazer J., Gress M., Horwitz J., Ashton C., Herndon B., Shapard L., and Nault R. M.; Basic Research Needs for Solar Energy Utilization. Report of the Basic Energy Sciences Workshop on Solar Energy Utilization, April 18-21, **2005**.

6. Fujishima A., Honda K.; *Nature* **1972**, *238*, 37-38.

7. Lan R., Irvine J. T.S., Tao S.; *International Journal of Hydrogen Energy*, **2012**, *37 (2)*, 1482-1494.

8. Gretz J., Drolet B., Kluyskens D., Sandman F., Ullmann O.; *International Journal of Hydrogen Energy*, **1994**, *19 (2)*, 169-174.

9. Wang R.R., Zhao Y.Q., Babich A., Senk D., Fan X.Y.; *Journal of Cleaner Production,* **2021**, *329*, 129797.

10. Ghavam S., Vahdati M., Wilson G. I.A., Styring P.; *Frontiers in Energy Research,* **2021**, *9*, 580808.

11. Cook T.R., Dogutan D.K., Reece S.Y., Surendranath Y., Teets T.S., Nocera D.G.; *Chemical Reviews*, **2010**, *110*, 6474–6502.

12. DOE Technical Targets for Hydrogen Production from Photoelectrochemical Water Splitting. Office of Energy Efficiency & Renewable Energy. **2023**. *www.energy.gov/eere/fuelcells/doe-technical-targets-hydrogen-production-photoelectrochemical-water-splitting*

13. Pinaud B. A., Benck J. D., Seitz L. C., Forman A. J., Chen Z., Deutsch T. G., James B. D., Baum K. N., Baum G. N., Ardo S., Wang H., Miller E., Jaramillo T. F.; *Energy and Environmental Science*, **2013**, *6*, 1983–2002.

14. Y. Goto, T. Hisatomi, Q. Wang, T. Higashi, K. Ishikiriyama, T. Maeda, Y. Sakata, S. Okunaka, H. Tokudome, M. Katayama, S. Akiyama, H. Nishiyama, Y. Inoue, T. Takewaki, T. Setoyama, T. Minegishi, T. Takata, T. Yamada, K. Domen.; *Joule*, **2018**, *2*, 509-520.

15. Nishiyama H., Yamada T., Nakabayashi M., Maehara Y., Yamaguchi M., Kuromiya Y., Nagatsuma Y., Tokudome H., Akiyama S., Watanabe T., Narushima R., Okunaka S., Shibata N., Takata T., Hisatomi T., and Domen K.; *Nature,* **2021**, *598*, 304–307.

16. Liu J., Liu Y., Liu N., Han Y., Zhang X., Huang H., Lifshitz Y., Lee S., Zhong J., and Kang Z.; *Science*, **2015**, *347*, 970-974.

17. Varadhan P., Fu H.C., Kao Y.C., Horng R.H., He. J.H.; *Nature Communications*, **2019**, *10*, 5282.

18. Takata T., Jiang J., Sakata Y., Nakabayashi M., Shibata N., Nandal V., Seki K., Hisatomi T., Domen K.; *Nature,* **2020**, *581*, 411–414.

19. Hao L., Hisatomi T., Goto Y., Yoshida M., Higashi T., Katayama M., Takata T., Minegishi T., Nishiyama H., Yamada T., Sakata Y., Asakura K., Domen K.; *Chemical Science*, **2019**, *10*, 3196-3201.

20. Ekspong J., Larsen C., Stenberg J., Kwong W. L., Wang J., Zhang J., Johansson E. M. J., Messinger J., Edman L., Wågberg T.; *ACS Sustainable Chemistry and Engineering*, **2021**, *9*, 14070−14078.

21. Zhou P., Navid I. A., Ma Y., Xiao Y., Wang P., Ye Z., Zhou B., Sun K., Mi Z.; *Nature*, **2023**, *613*, 66-70.

22. J. Valasek.; The American Physical Society, **1920**, 6, 537-538.

23. C.A. Randall, R.E. Newnham, L.E. Cross.; The American Ceramic Society, **2009**.

24. Kim T. Y., Kim S. K., and Kim S. W.; *Nano Convergence,* **2018***, 5*, 30.

25. Schmid H.; *Journal of Physics: Condensed Matter*, **2008**, *20*, 434201.

26. Litvin D. B.; *Acta Crystallographica Section A*, **2008**, *A64*, 316–320.

27. Shi P. P., Tang Y. Y., Li P. F., Liao W. Q., Wang Z. X., Ye Q., and Xiong R. G.; *Chemical Society Reviews*, **2016**, *45*, 3811-3827.

28. Aizu K.; *Physical Review B*, **1970**, *2* (3), 754-772.

29. Starkiewicz J., Sosnowski L., and Simpson O.; *Nature*, **1946**, *158*, 28.

30. Goldstein B., and Pensak L.; *Journal of Applied Physics*, **1958**, *30*, 155-161.

31. Reuter H., and Schmitt H.; *Journal of Applied Physics*, **1995**, *77*, 3209-3218.

32. Pal U., Saha S., Chaudhuri A. K., and Banerjee H. D.; *Journal of Applied Physics*, **1991**, *69*, 6547-6555.

33. Koch W. T. H., Munser R., Ruppel W., Würfel P.; *Ferroelectrics*, **1976**, *13 (1)*, 305-307.

34. Tiwari D., Dunn S.; *Journal of Materials Science*, **2009**, *44*, 5063–5079.

35. Nuraje N., and Su K.; *Nanoscale*, **2013**, *5*, 8752-8780.

36. Yang S.Y., Seidel J., Byrnes S. J., Shafer P., Yang C. H., Rossell M. D., Yu P., Chu Y. H., Scott J. F., Ager J. W., Martin L. W., Ramesh R.; *Nature Nanotechnology*, **2010**, *5*, 143–147.

37. Fridkin V. M., and Popov B. N.; *Soviet Physics Uspekhi*, **1978**, *21*, 981-991.

38. Yuan Y., Xiao Z., Yang B., and Huang J.; *Journal of Materials Chemistry A*, **2014**, *2*, 6027-6041.

39. Choi T., Lee S., Choi Y. J., Kiryukhin V., and Cheong S. W.; *Science*, **2009**, *324*, 63-66.

40. Baltz R. von.; *Physica Status Solidi B*, **1978**, *89*, 419-429.

41. Wang Q., and Domen K.; *Chemical Reviews*, **2020**, *120*, 2, 919–985.

42. Takanabe K.; *ACS Catalysis*, **2017**, *7* (11), 8006−8022.

43. Yanagi R., Zhao T., Solanki D., Pan Z., and Hu S.; *ACS Energy Letters*, **2022**, *7*, 432−452.

44. Pan Z., Yanagi R., Wang Q., Shen X., Zhu Q., Xue Y., Rohr J. A., Hisatomi T., Domen K., and Hu S.; *Energy and Environmental Science*, **2020**, *13*, 162-173.

45. Wang X., and Li C.; *Journal of Physical Chemistry C*, **2018**, *122*, 37, 21083–21096.

46. Chowdhury F. A., Trudeau M. L., Guo H., Mi Z.; *Nature Communications*, **2018**, *9*, 1707.

47. Zhang A., Wang W. Y., Chen J. J., Liu C., Li Q. X., Zhang X., Li W. W., Si Y., and Yu H. Q.; *Energy and Environmental Science*, **2018**, *11*, 1444-1448.

48. Ye R., Hurlburt T. J., Sabyrov K., Alayoglu S., Somorjai G. A.; *Proceedings of the National Academy of Sciences of the United States of America*, **2016**, *113* (19), 5159−5166.

49. Wang X., and Li C.; *Journal of Photochemistry and Photobiology C: Photochemistry Reviews*, **2017**, *33*, 165−179.

50. Yang J., Wang D., Han H., Li C.; *Accounts of Chemical Research*, **2013**, *46* (8), 1900−1909.

51. Li L., Salvador P. A., Rohrer G. S.; *Nanoscale*, **2014**, *6* (1), 24−42.

52. Li Y., Li J., Yang W., Wang X.; *Nanoscale Horizons*, **2020**, *5* (8), 1174−1187.

53. Zhang Z., Yates Jr. J. T.; *Chemical Reviews*, **2012**, *112*, 5520−5551.

54. Kamloth K. P.; *Chemical Reviews*, **2008**, *108*, 367−399.

55. Fan F. R. F., Bard A. J.; *Journal of American Chemical Society*, **1980**, *102*, 11, 3677− 3683.

56. Bard A. J., Bocarsly A. B., Fan F. R. F., Walton E. G., and Wrighton M. S.; *Journal of the American Chemical Society*, **1980**, *102*, 11, 3671–3677.

57. Kronik L., Shapira Y.; *Surface Science Reports*, **1999**, *37*, 1–206.

58. Dittrich T., and Fengler S.; Surface Photovoltage Analysis of Photoactive Materials; World Scientific Publishing Europe Ltd: **2020**.

59. Sell K., Barke I., Polei S., Schumann C., Oeynhausen V. v., Broer K. H. M.; *Physica Status Solidi B*, **2010**, *247* (5), 1087–1094.

60. Osterloh F. E., Holmes M. A., Zhao J., Chang L., Kawula S., Roehling J. D., and Moule A. J.; *Journal of Physical Chemistry C*, **2014**, *118*, 14723−14731.

61. Wang J., and Osterloh F. E.; *Journal of Material Chemistry A*, **2014**, *2*, 9405-9411.

62. Ma X., Cui X., Zhao Z., Melo Jr. M. A., Roberts E. J., Osterloh F. E.; *Journal of Materials Chemistry A*, **2018**, *6*, 5774.

63. Doughty R. M., Hodges B., Dominguez J., Han R., Zhao Z., Assavachin S., Osterloh F. E.; *Journal of Physical Chemistry C*, **2020**, *124*, 18426−18435.

64. Ishii T., Kato H., Kudo A.; *Journal of Photochemistry and Photobiology A*: *Chemistry*; **2004**, *163* (1-2), 181-186.

65. Cui Y., Briscoe J., and Dunn S.; *Chemistry of Materials*, **2013**, *25* (21), 4215-4223.

66. Giocondi J. L., and Rohrer G. S.; *The Journal of Physical Chemistry B*, **2001**, *105* (35), 8275-8277.

67. Park S., Lee C. W., Kang M. G., Kim S., Kim H. J., Kwon J. E., Park S. Y., Kang C. Y., Hong K. S., and Nam K. T.; *Physical Chemistry Chemical Physics*, **2014**, *16*, 10408-10413.

Chapter 2 - Ferroelectric Surface Photovoltage Enhancement in Chromium-doped $SrTiO_3$ Nanocrystal Photocatalysts for Hydrogen Evolution

Reproduced from ref. 1 with permission from The Royal Society of Chemistry – Material Advances. [1]

2.1 Introduction

Visible light active photocatalysts capable of splitting water have been explored extensively in recent years because hydrogen is a clean and renewable fuel. [2-5] $SrTiO_3$ is appealing due to its high chemical stability and band edges that are appropriately positioned for proton reduction and water oxidation. [6-11] However, the wide band gap of $SrTiO_3$ (3.2 eV) restricts the absorption of photons to less than 5% of the solar spectrum (UV light only). Doping of $SrTiO_3$ with metal ions (M = Rh, Ru, Cr) adds new states inside the band gap, allowing photochemical H_2 evolution under visible light. [12–21] Among these dopants, Cr is attractive because it is an earth abundant element. [17-24] For example, Pt-decorated $SrTiO_3$:Cr,La nanocrystals promote hydrogen evolution from methanol under visible light (25.6% at 425 nm). [21] In this work, we use surface photovoltage spectroscopy to study carrier dynamics in thin films of $SrTiO_3$:Cr nanocrystals on gold substrates. Time-dependent photovoltage measurements reveal an anomalous photovoltage that increases with intermittent illumination and exceeds the maximum photovoltage predicted by the thermodynamics of the Au/$SrTiO_3$:Cr system. Electric polarization experiments confirm that the anomalous photovoltage is due to a ferroelectric effect in the material.

2.2 Results and Discussion

$SrTiO_3$:Cr nanocrystals were obtained as a brownish-yellow powder (**Figure. 2.1a)**, in nearly quantitative yield by hydrothermal synthesis from TiO_2, $Sr(OH)_2$, and $Cr(NO_3)_3$ in water, using a modification of a

published process. [8,25] Electron microscopy images of $SrTiO_3$:Cr are shown in **Figure 2.1a,b**. The particles form well defined cubic-shaped nanocrystals with a mean diameter of 45 nm (±15 nm), similar to other transition metal-doped $SrTiO_3$ nanoparticles, made by the same hydrothermal reaction. [16] The phase purity and crystallinity of $SrTiO_3$:Cr was confirmed by powder X-ray diffraction (**Figure 2.1c)**. All peaks can be indexed to the perovskite crystal structure. As expected, chromium doping did not shift the 2θ position of the diffraction peaks of $SrTiO_3$ because the ionic radius of hexacoordinate Cr^{3+} (62.0 pm) is very similar to that of Ti^{4+} (61.0 pm).

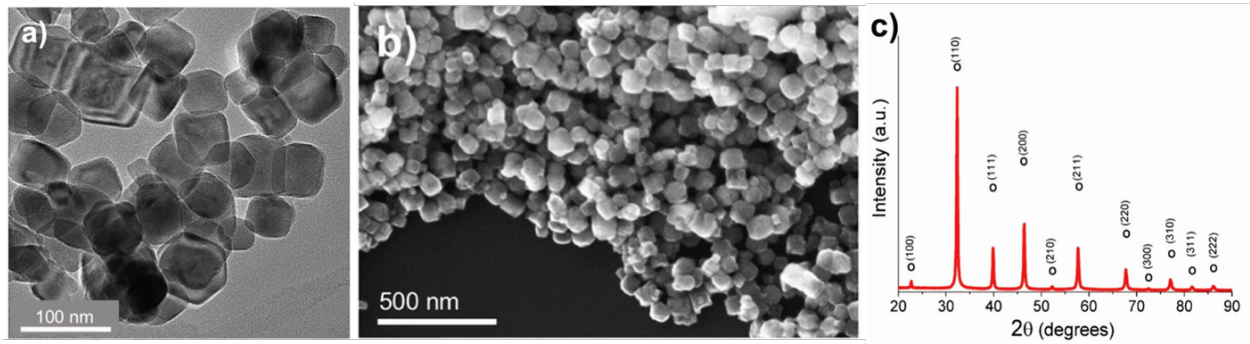

Figure 2.1. a) TEM and b) SEM images, c) powder X-ray diffraction pattern of $SrTiO_3$:Cr nanocrystals. All observed peaks can be assigned to the perovskite crystal structure (pdf card #01-080-4368).

The chemical surface composition of the $SrTiO_3$:Cr nanostructures was characterized by X-ray photoelectron spectroscopy (XPS). **Figure 2.2a** shows two Ti 2p peaks at 458.6 and 464.3 eV belonging to lattice Ti^{4+}, [26] and two peaks at 457.7 and 463.6 eV which are attributed to Ti^{3+} species. The relative atomic percentages of Ti^{4+} and Ti^{3+} are 78.8% and 21.2%. The latter is located predominantly at the $SrTiO_3$:Cr surface, based on earlier XPS studies for $SrTiO_3$. [27] The Cr 2p spectrum exhibit two doublet peaks which can be assigned to Cr^{3+} species (586 eV and 576 eV) and Cr^{6+} (590 eV and 580 eV), respectively. The relative amounts are 68.3% Cr^{3+} and 31.7% Cr^{6+}. Based on the XPS survey spectrum (**Appendix 2.7)**, the

Cr^{3+} ion concentration on the surface of the sample is estimated as 2.05 at% (based on B lattice sites) (**Figure 2.2c)** shows the valence band XPS spectrum for the $SrTiO_3$:Cr nanocrystals. The measured VB edge energy position was 1.73 eV relative to its Fermi level, which is close to the reported value (1.69 eV) for $SrTiO_3$. [11] This shows that the Cr^{3+} species does not significantly shift the VB edge, as further supported by the optical data below.

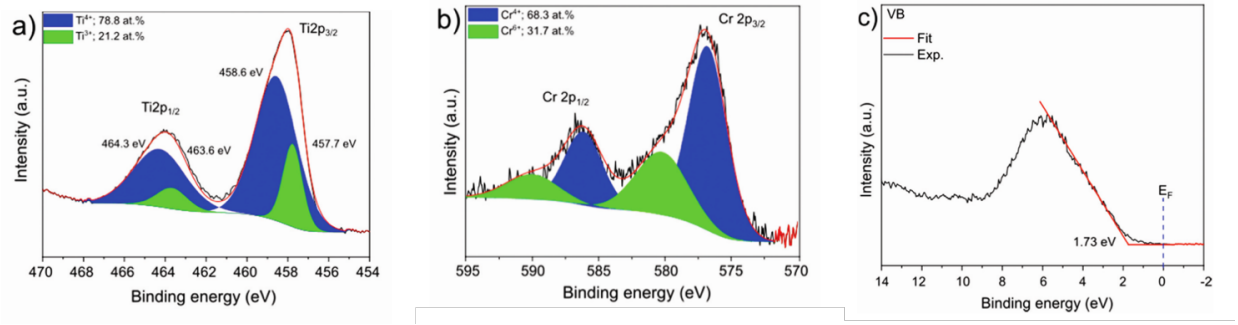

Figure 2.2. XPS spectra of the core level of the (a) Ti 2p region (b) Cr 2p region, and (c) valence band XPS spectrum.

To investigate the optical properties of the $SrTiO_3$:Cr samples, UV-vis diffuse reflectance spectra were collected for $SrTiO_3$:Cr and plotted as the Kubelka Munk function in **Figure 2.3a**. The spectrum for the Cr-doped nanocrystals shows two major absorptions with onsets at 2.3 eV (544 nm) and at 3.2 eV. While the latter belongs to the light absorption by the $SrTiO_3$ host, [28] the former can be assigned to electronic transition from occupied Cr^{3+} 3d orbitals to the unoccupied Ti 3d orbitals (**Figure 2.3b)**. [17,20,29–31] Spectra also show a weak absorption tail at 1.8–2.3 eV that can be assigned to Cr^{6+} species which can form as a result of air oxidation of Cr-doped $SrTiO_3$. [18] Indeed, prolonged storage in air increases the optical absorption below 2.5 eV (**Appendix 2.8)**. Based on the XPS data (**Figure 2.2)** the Cr^{6+} ions in fresh samples are concentrated at the nanocrystal surface.

To evaluate the photochemical activity for H_2 evolution, freshly prepared $SrTiO_3$:Cr nanocrystal powders were modified with 0.5 wt% platinum nanoparticles by photodeposition and dispersed in a 20 vol% aqueous methanol solution (**Figure 2.3c)**.

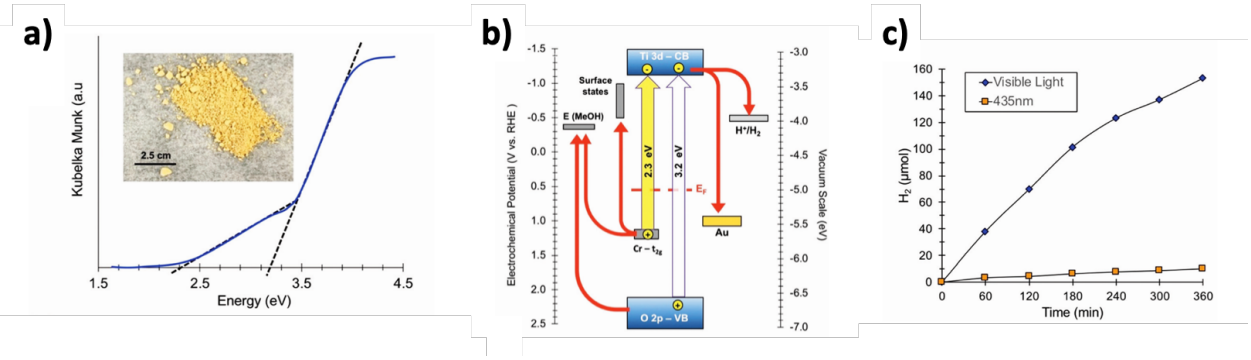

Figure 2.3. a) UV-vis diffuse reflectance optical spectra of $SrTiO_3$:Cr films (see also **Appendix 2.8**). Inset: Optical photograph of $SrTiO_3$:Cr powder. b) Energy diagram showing band edges and substrate work functions at the point of zero charge (near pH 7). E_F (0.55 eV) from UV-PS data in **Figure 2.2c**. Ti^{3+} states and $SrTiO_3$ band edges from Ma et al. [35] Gold work function from Lide et al. [36] c) H_2 evolution from suspension of Pt-$SrTiO_3$:Cr nanocrystals: 110 mg of photocatalyst in 20% (vol) aqueous methanol solution at pH 7 under visible light irradiation ($\lambda > 400$ nm, 270 mW cm^{-2}) or illumination at 435 nm from an LED (19.3 mW cm^{-2}).

Under broad band illumination, steady H_2 production is observed over the 5 h interval, with rates declining from 38.02 μmol h^{-1} during the first hour to 25.53 μmol h^{-1} during the last hour. In contrast, non-doped $SrTiO_3$ nanocrystals have only minimal activity for H_2 evolution under visible light (>400 nm). [16] This suggests that the visible light activity of $SrTiO_3$:Cr is due to excitation of Cr states (**Figure 2.3b)**. Under 435 nm illumination (LED, 19.3 mW cm^{-2}), H_2 was produced at up to 1.66 μmol h^{-1} corresponding to an

apparent quantum efficiency of 0.66%. The activity drops slightly (to 0.61%) after particles are isolated by centrifugation and re-suspended in aqueous methanol (**Appendix 2.9)**. These values are much lower than what has been reported for La,Cr co-doped $SrTiO_3$ (25.6% at 425 nm) from 5 M KOH/20 vol% MeOH solution. [21] The higher activity in that case is attributed equally to the high pH of ~14.5 and to the presence of the La dopant. Lanthanum ions have been shown to suppress the oxidation of Cr^{3+} to Cr^{6+}, which is an electron–hole recombination site in $SrTiO_3$. [15,32,33] Additionally, the lower pH promotes methanol oxidation. [34]

In order to gain more insight into photochemical charge separation in the $SrTiO_3$:Cr particles, surface photovoltage spectroscopy (SPS) experiments were conducted. In SPS, the contact potential difference (CPD) of a sample film on top of a conductive substrate is recorded with a contactless Kelvin probe as a function of the incident photon energy. [37–39] The change of the CPD under illumination (the photovoltage) provides information about the majority carrier type, the effective band gap, and defects in the sample. [25,40-44] Measurements were conducted under vacuum conditions on $SrTiO_3$:Cr particle films deposited onto gold-coated glass substrates. The SPS data for a fresh sample (A) (**Figure 2.4a)** together with an optical absorption spectrum of the material. The negative photovoltage is attributed to transfer of electrons from Cr^{3+} states into the $SrTiO_3$ conduction band and from there to the gold substrate (**Figure 2.3b)**. Electrons are the majority carriers suggesting that $SrTiO_3$:Cr is an n-type semiconductor despite its Fermi level near the mid gap position. The onset of the photovoltage lies near 1.75 eV, nearly 0.6 eV below the optical absorption from the Cr^{3+} states. The detailed reasons for this early photovoltage onset are not clear. Tentatively, we attribute it to acceptor states 1.75 eV above the $SrTiO_3$ valence band that are caused by oxygen vacancy complexes $\{Ti^{4+}, V_O\}$ in the material. [11] As can be seen from **Figure 2.4a**, the photovoltage reaches approximately ~3.7 V at 2.7 eV and increases only mildly upon excitation of the $SrTiO_3$ host at 3.2 eV. At photon energies above 3.5 eV, the photovoltage decays due to decreasing light intensity of the Xe lamp (for Xe emission spectrum see ref. 44) and due to the finite light penetration depth of the sample.

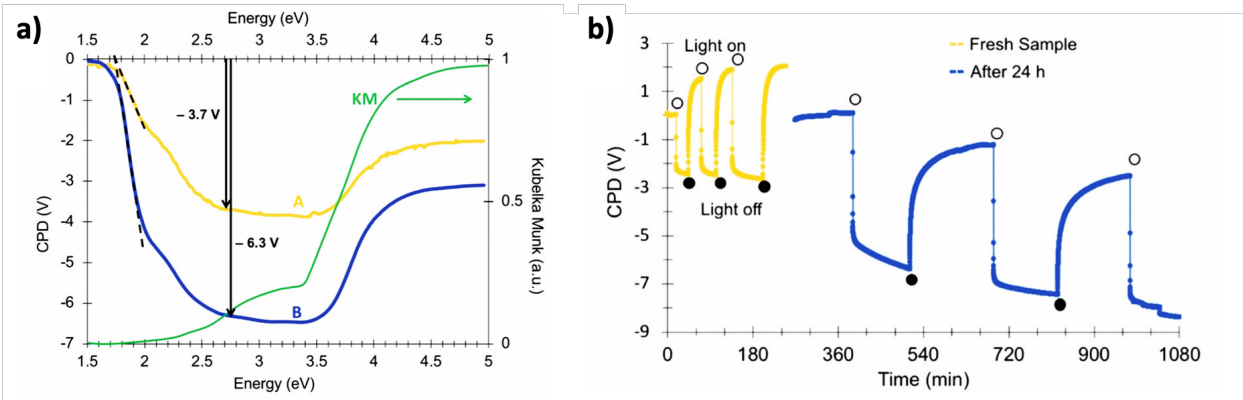

Figure 2.4. a) Surface photovoltage spectra of $SrTiO_3$:Cr particle films on gold substrate, before (A) and after (B) intermittent illumination at 2.50 eV and storing in vacuum for 24 h. (b) Transient photovoltage of $SrTiO_3$:Cr on Au substrate during intermittent 2.50 eV illumination (0.1 mW cm^{-2}) and after keeping $SrTiO_3$:Cr film for 24 h in the dark and under vacuum.

Interestingly, when the spectrum is recorded again for a sample that was illuminated with 2.5 eV light and then kept in the dark under vacuum for 24 h, the photovoltage increases over almost the entire spectral range (spectrum B in **Figure 2.4a**). At 2.7 eV, the photovoltage reaches ~6.3 V, a 70% increase over the fresh sample. This increased photovoltage cannot be explained on the basis of the energy diagram (**Figure 2.3b)**. According to that diagram, the Au/$SrTiO_3$:Cr configuration can produce a maximum photovoltage of –4.2 V (–2.1 V from electron transfer from the $SrTiO_3$ conduction band into the gold substrate and –2.1 V from hole trapping at Ti^{3+} surface sites). [35] In order to investigate the reason for the abnormally large photovoltage, SPS scans were repeated for a fresh sample under transient monochromatic illumination at 2.50 eV. As can be seen from **Figure 2.4b**, the initial cycle only produces a photovoltage of –2.4 V, but sequential illumination cycles gradually increase the value to –4.2 V. When the sample film is kept under vacuum and in the dark for 24 h and is again exposed to monochromatic light at 2.50 eV, it produces a –5.5 V photovoltage. However, the anomalous photovoltage is quenched entirely when the sample is stored in air for 12 h (**Appendix 2.10)**. Furthermore, the scans in **Figure 2.4b** show that photovoltage generation

and decay occur on different timescales. Photovoltage formation is observed on the 10 s timescale, which indicates that electron transfer from $SrTiO_3$:Cr to the gold substrate occurs by an electric field assisted process (drift). Similar drift processes were observed before in samples of CdSe quantum dots [45] films of P3HT, [46,47] and at the surface of silicon wafers. [41] The photovoltage decay, on the other hand is much slower, requiring ~100 s in the first set of scans (yellow curve), and over 500 s in the second set (blue curve). This slower timescale is typically associated with the diffusion of charge carriers, as previously seen for other nanostructured light absorbers, incl. $HCa_2Nb_3O_{10}$ nanosheets, [42] Fe_2O_3 nanowires, [48] and $BiVO_4$ particles. [41] The data in **Figure 2.4b** suggests that charge transport in the dark becomes slower after each illumination cycle.

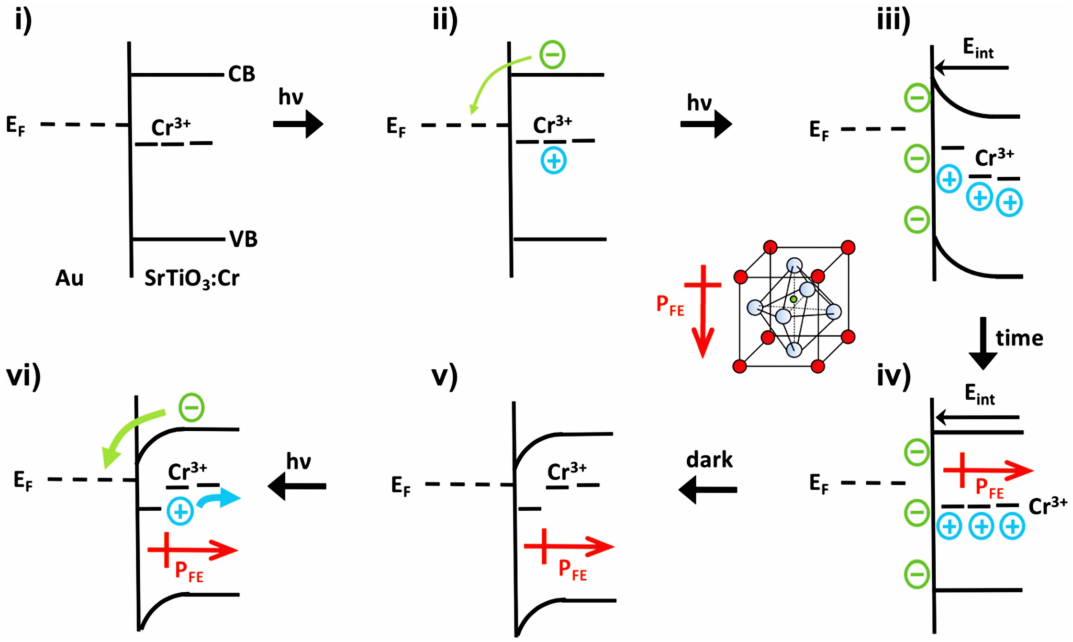

Figure 2.5. Energy diagram of the Au/$SrTiO_3$:Cr system: sample (i) in the dark, (ii) under illumination with 2.50 eV photons, (iii) under illumination at electrochemical equilibrium, (iv) under illumination after ferroelectric polarization, (v) in the dark, after return of majority carriers, (vi) repeat illumination with 2.50 eV photons showing enhanced electron transfer. E_F = Fermi level, E_{int} = electric field across depletion layer, P_{FE} = ferroelectric dipole. Inset: Unit cell of $SrTiO_3$:Cr with central Cr^{3+} ion displaced upwards.

The unusual photovoltage behaviour of the Au/$SrTiO_3$:Cr nanocrystal films can be explained with the ferroelectric (FE) polarization mechanism (**Figure 2.5)**. In the dark, there is no electric field across the nanocrystal film and the bands stay flat (i). Under illumination, electrons are injected into the gold substrate leaving the nanocrystal film positively charged (ii/iii). The electric field associated with the depletion layer (iii) polarizes the nanocrystals to produce a semi-permanent ferroelectric dipole (iv) that grows over time. When the light is turned off, electrons flow back into the nanocrystal film, but the electric dipole persists and causes the contact potential to increase above the initial value (v). Photoelectrons generated in subsequent illumination cycles now move with or against the electric field of the ferroelectric dipoles (vi), causing the fast abnormal photovoltage signal in **Figure 2.4** and the increasingly slow baseline recovery in later scans. On the basis of the –5.5 V ΔCPD value, the ferroelectric polarization is estimated as 0.9 x 10^6 V m^{-1} across the 6.0 μm thick film. This corresponds to a 41 mV potential difference across a single 45 nm thick $SrTiO_3$:Cr nanocrystal. The presence of the FE dipole also explains why baseline recovery (177 min) takes 16 times longer than photovoltage formation (11 min). This is because electrons under illumination move along the dipole, but have to move against it when the light is turned off.

To confirm the ferroelectric polarization in **Figure 2.5**, surface photovoltage spectra and transient photovoltage signals were recorded for Au/$SrTiO_3$:Cr films after polarization in a static electric field in air. Electric polarization was performed (**Figure 2.6a)**, in forward or reverse bias, with the polarity of the applied potential (154 V) defined in the figure. Immediately after electric polarization, samples were placed under vacuum and their photovoltage was measured.

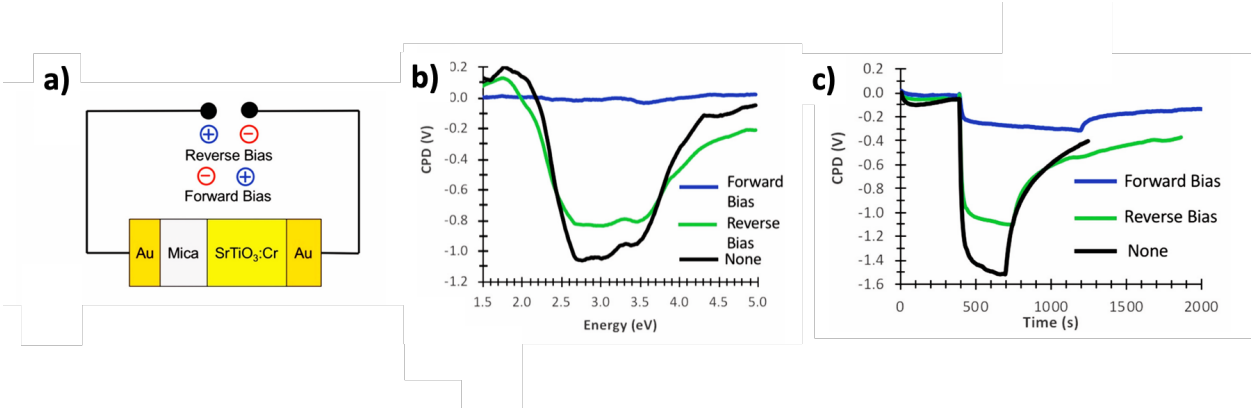

Figure 2.6. a) Schematic setup for electric polarization of the Au/$SrTiO_3$:Cr film. b) Surface photovoltage spectra and c) transient photovoltage scans (2.5 eV excitation) of films before and after electric polarization under forward and reverse bias. Reverse bias depletes the $SrTiO_3$:Cr sample of majority carriers while forward bias increases the majority carrier concentration.

As the data **Figure 2.6b,c** shows, forward bias nearly completely quenches the negative surface photovoltage in both the spectral and also in the time resolved domains. This agrees with the model in above. A forward electric bias polarizes the material in the opposite way as during the step iii (**Figure 2.5)**. Because the generated ferroelectric dipole opposes the movement of photoelectrons into the gold substrate, it reduces the negative photovoltage. On the other hand, the reverse bias polarizes the films as in step iii (**Figure 2.5)**, thereby promoting electron injection into the gold substrate. The lack of a photovoltage enhancement (**Figure 2.6)** compared to a non-polarized film is attributed to the limited stability of the ferroelectric polarization nanocrystals in air, as mentioned above (**Appendix 2.10)**. Details of the deactivation mechanism and of the atomic level origin of the effect are subject to ongoing studies. Tentatively, we believe that the FE polarization involves the movement of either Cr^{3+} or photogenerated Cr^{4+} cations in the perovskite unit cell (inset **Figure 2.5)**.

2.3 Conclusion

In summary, cubic $SrTiO_3$:Cr nanocrystals in the perovskite structure type with 2.05% atomic Cr^{3+} content and an optical band gap of 2.3 eV were synthesized by hydrothermal reaction and observed to catalyse hydrogen evolution from aqueous methanol solution with quantum efficiencies of up to 0.66% at 435 nm. According to surface photovoltage spectroscopy, the $SrTiO_3$:Cr nanocrystals are n-type and have an effective band gap of 1.75 eV. Under transient illumination, $SrTiO_3$:Cr nanocrystal films on gold show an anomalous –6.3 V surface photovoltage that can be explained on the basis of ferroelectric polarization of $SrTiO_3$:Cr in the depletion layer near the Au interface. The polarization is stable for 24 h in vacuum, but degrades within 12 h in air, due to an unknown mechanism. Electric polarization experiments confirm the effect of electric fields (1.20 MV m^{-1}) on the surface photovoltage behaviour of $SrTiO_3$:Cr films. The finding of a ferroelectric effect in $SrTiO_3$:Cr is not unexpected. Ferroelectric effects are commonly observed in $SrTiO_3$ after doping with Sn, [49] Ca, [29,50] Pr, [51] and Fe, [52] and are also well documented for $BaTiO_3$ where the electric dipole moment results from the displacement of Ti^{4+} ions from their equilibrium position. [53] Because electric dipoles aid photocarrier separation, [53–56] ferroelectric light absorbers are of interest for the construction of photocatalysts [57,58] and photovoltaics [54,59] with increased open-circuit voltage and potentially higher power conversion efficiency.

2.4 Experimental Section

Strontium hydroxide octahydrate (99%, Alfa Aesar), titanium(IV) oxide P25 (99.5%, Acros Organics), potassium hydroxide, (≥85%, Sigma-Aldrich), and chromium nitrate nonahydrate (99.99%, Acros Organics) were used as received. Water was purified by a nanopure system (18 MΩ cm). $SrTiO_3$:Cr nanocrystals were synthesized by modification of the published procedure. [8,25] First, 0.175 g (2.18 mmol) of P25 TiO_2 powder was added to a 45 mL PTFE lined autoclave containing an aqueous solution of 0.598

g (2.25 mmol) of $Sr(OH)_2$ in 35 mL of water. The solution was stirred during the addition of 0.0270 g (0.0675 mmol) $Cr(NO_3)_3 \cdot 9H_2O$ and then heated at 423 K for 72 h in a sealed stainless-steel autoclave. After natural cooling to room temperature, the resulting solid yellow product was washed several times by centrifugation in ultrapure water until the pH of the supernatant measured below 8.5. The solid was dried under vacuum to produce the yellow powder in approximately 96% yield.

Particle Film Fabrication

Film samples were prepared by drop-casting suspensions of $SrTiO_3$:Cr particles in water on gold substrates followed by air overnight (for UV/vis), or annealing at 100ºC in air for 20 min (for SPS), or at 300ºC for 2 hours in air (for the electric polarization experiments). Film thicknesses were measured using a stylus-type Veeco DekTak profilometer.

Co-Catalyst Deposition

Loading of 0.5 (% wt) Pt co-catalysts onto $SrTiO_3$:Cr nanocrystals was completed by suspending 150 mg of $SrTiO_3$:Cr nanocrystals in 100 mL 20% (vol) MeOH (aq.) solution together with 0.75 mL of a 1.0 mg mL^{-1} solution of $H_2PtCl_6 \cdot H_2O$. The mixture was illuminated with a 300 W Xe arc lamp for 4 h while stirring after the system was purged with argon gas for 5 cycles. After that, the solid was isolated by centrifugation, washed several times with water and dried overnight under vacuum to yield 120 mg of Pt–$SrTiO_3$:Cr nanocrystals.

Photochemical Hydrogen Evolution

Photochemical H_2 evolution was measured by irradiating 110 mg of Pt-$SrTiO_3$:Cr photocatalyst dispersed in 100 mL of a 20% aqueous methanol solution at neutral pH. Irradiations were performed in a round

bottom quartz flask. The light from a 300 W Xe arc lamp was filtered through an aqueous $NaNO_2$ solution as long-pass filter ($\lambda > 400$ nm) and some of the infrared portion of the spectrum. The intensity at the flask was 60 mW cm^{-2} measured by GaAsP photodetector for the 250–680 nm interval. The quartz flask was connected to vacuum and to a gas chromatograph (Varian 3800) by an air-tight circulation system that allowed the sample flask to be evacuated and purged with argon before taking measurements. Apparent Quantum Yield (AQE) measurements were completed by using a monochromatic 435 nm LED (light intensity = 19.3 mW cm^{-2}).

Material Characterization

Powder X-ray diffraction scans were performed using a Bruker D8 Advance Eco with a Cu Ka X-ray radiation and a monochromatic wavelength of 1.5418 Å. Transmission electron microscopy (TEM) micrographs were collected using a Philips CM-120 TEM instrument at 120 kV accelerating voltage. Samples were prepared by immersing copper TEM grids with carbon film into dilute suspensions of $SrTiO_3$:Cr, followed by drying at room temperature. Scanning electron microscopy (SEM) images were recorded using Philips XL-30 Scanning Electron Microscope. Samples for SEM were prepared by drop-coating aqueous solutions containing the particles onto pieces of an n-silicon wafer and allowed to dry in air while covered. X-ray photoelectron spectroscopy (XPS) were performed using a Scienta Omicron (ESCA+) XPS spectrometer with a high- performance hemispheric analyzer (EAC2000 sphere) with monochromatic Al Ka (hv = 1486.6 eV) radiation source. The operating pressure in the ultra-high vacuum chamber (UHV) during the analysis was 10^{-9} Pa. The XPS high resolution spectra were recorded at constant pass energy of 20 eV with a 0.05 eV per step, while the survey scan was taken at 50 eV pass energy with a 0.5 eV per step. XPS measurements were carried out using 50 mg of sample placed on a double-sided adhesive tape (5.0 x 5.0 mm), covering completely the surface area, in order to ensure that no XPS signal are due to the tape. The adventitious carbon C1s peak at 284.8 eV was used as reference for calibration. A Shirley background subtraction was performed before the curve fitting for all data. The atomic percentage

is calculated on the basis of the relative peak intensities and using appropriate relative sensitivity factors (RSF). Valence band XPS data were calibrated by linear extrapolation of the signal to zero intensity and by equating the zero-intensity point to 0 eV binding energy, which is by definition the Fermi level of the sample. The adventitious carbon C1s peak at 284.8 eV forming on the sample surface during calcination in air was used as reference for calibration. UV-Vis diffuse reflectance spectra were recorded using a Thermo Scientific Evolution 220 Spectrometer equipped with an integrating sphere. The absorption data was converted to diffuse reflectance spectra using the Kubelka–Munk function [$f(R) = (1 - R)^2/(2R)$] to correct for light scattering. Surface Photovoltage Spectroscopy (SPS) measurements were completed using a vibrating gold mesh Kelvin probe (Delta PHI Besocke) controlled with a Kelvin control 07 unit (Delta PHI Besocke, Germany). Samples were mounted inside a home-built vacuum chamber and equipped with quartz window and placed under vacuum (2×10^{-4} mbar). Illumination was done with monochromatic light from a 150 W Xe lamp filtered through an Oriel Cornerstone 130 monochromator (1–10 mW cm^{-2}). Contact potential difference (CPD) values are quoted relative to the values in the dark. Illumination for the transient photovoltage experiments was performed at 2.50 eV (0.1 mW cm^{-2}). Electric Polarization experiments were conducted (**Figure 2.6a)** in air for one hour. For this, $SrTiO_3$/Cr films on gold were prepared as described above and then covered with a 122.94 mm thick mica sheet (Electron Microscopy Sciences) and placed opposite of a gold coated glass slide as counter electrode. The gold substrate and counter electrode were connected to D.C. power source (154 V measured voltage) constructed by connecting sixteen 9 V alkaline batteries in series.

2.5 Appendix

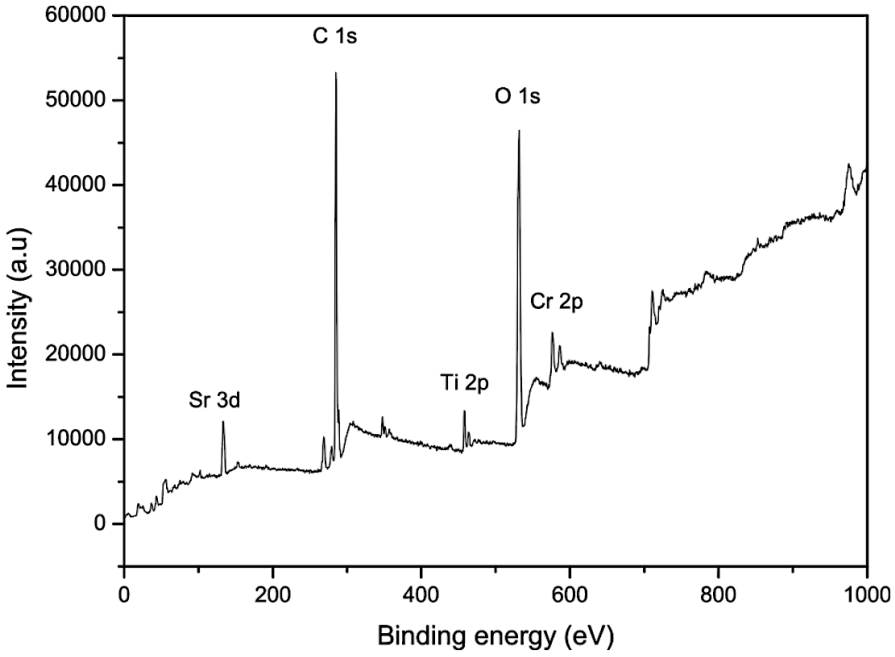

Figure 2.7. X-ray photoelectron survey spectrum.

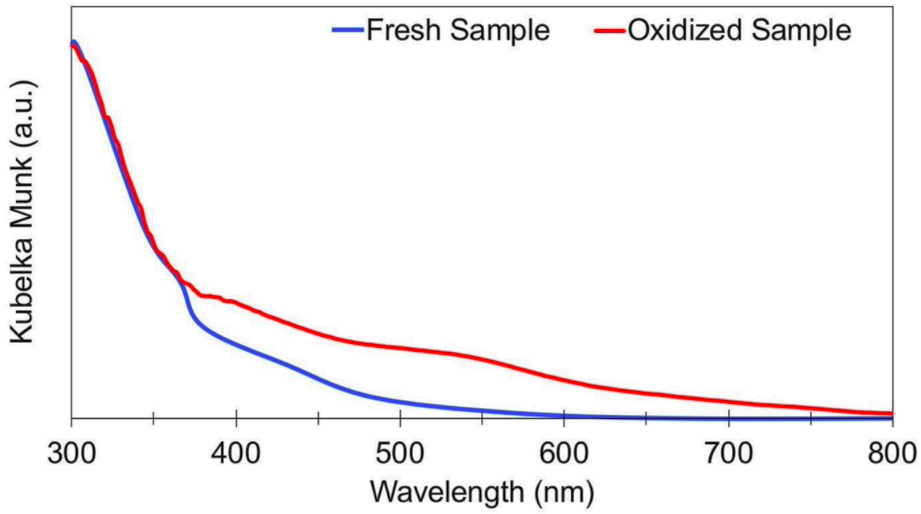

Figure 2.8. KM plot for a fresh and an oxidized $SrTiO_3$:Cr film (after storing in air for 3 months).

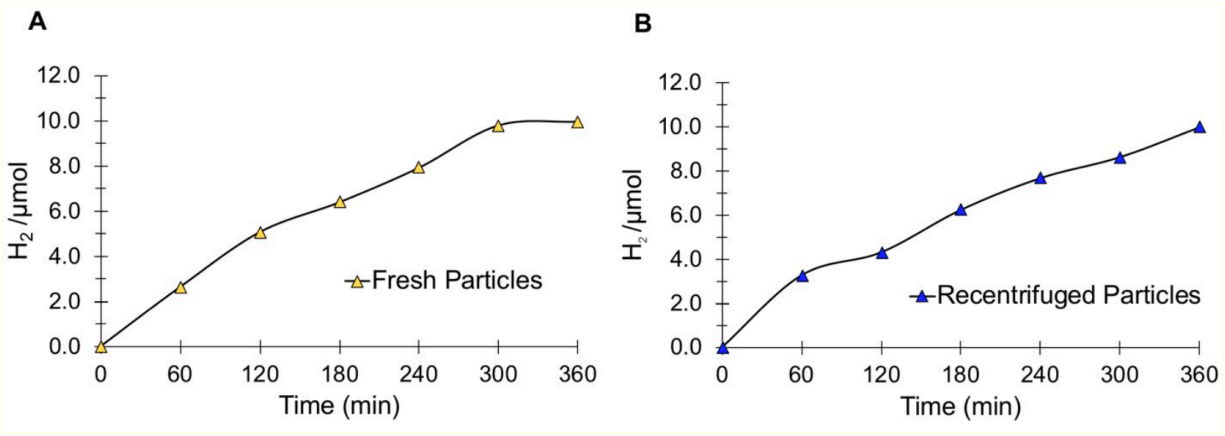

Figure 2.9. AQE Measurement on 0.5% wt. Pt: $SrTiO_3$:Cr under 435nm illumination in 20% aqueous methanol solution (irradiation area of 2.01 cm^2). A) Lamp intensity = 19.3 mW/cm^2 on freshly made sample with AQE = 0.66%. B) 20.91 mW/cm^2 lamp intensity on recentrifuged sample after 6 hours irradiation with AQE = 0.61% (7.6% decrease from original value).

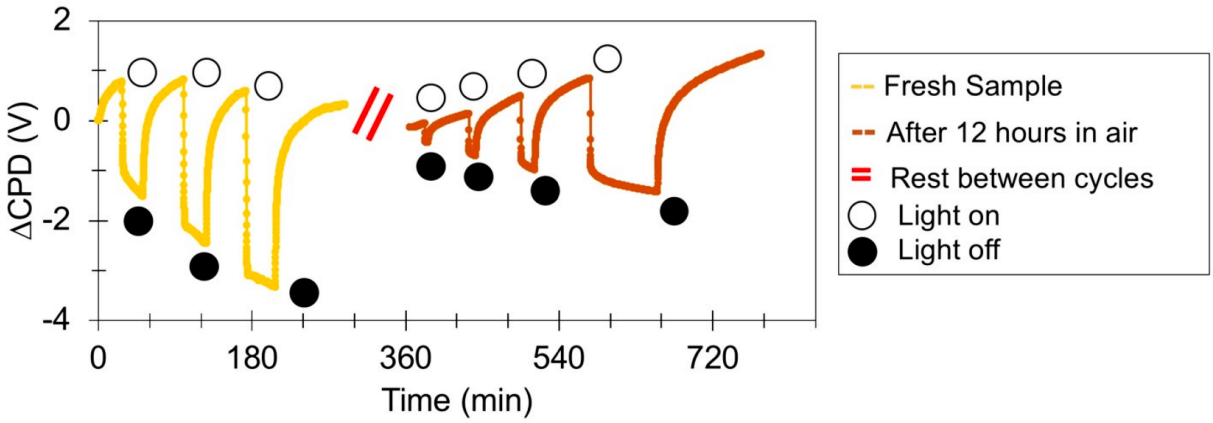

Figure 2.10. Transient photovoltage of Au/$SrTiO_3$:Cr under 2.5eV illumination before and after sample exposure to air (dark) for 12 h.

2.6 References

1. Assavachin S., Nail B. A., Goncalves R. V., Mulcahy J. R., Lloyd S. E., and Osterloh F. E.; *Materials Advances*, **2020**, *1*, 1382-1389.

2. Bard A. J., and Fox M. A.; *Accounts of Chemical Research*, **1995**, *28*, 141–145.

3. Fabian D. M., Hu S., Singh N., Houle F. A., Hisatomi T., Domen K., Osterloh F. E., and Ardo S.; *Energy and Environmental Science*, **2015**, *8*, 2825–2850.

4. Chen S., Takata T., and Domen K.; *Nature Reviews Materials*, **2017**, *2*, 17050.

5. Osterloh F. E.; *ACS Energy Letters*, **2016**, *1*, 1060–1061.

6. Mavroides J. G., Kafalas J. A., and Kolesar D. F.; *Applied Physics Letters*, **1976**, *28*, 241–243.

7. Domen K., Kudo A., and Onishi T.; *Journal of Catalysis*, **1986**, *102*, 92–98.

8. Townsend T. K., Browning N. D., and Osterloh F. E.; *ACS Nano*, **2012**, *6*, 7420–7426.

9. Osterloh F. E.; *Chemistry of Materials*, **2008**, *20*, 35–54.

10. Goto Y., Hisatomi T., Wang Q., Higashi T., Ishikiriyama K., Maeda T., Sakata Y., Okunaka S., Tokudome H., Katayama M., Akiyama S., Nishiyama H., Inoue Y., Takewaki T., Setoyama T., Minegishi T., Takata T., Yamada T., and Domen K.; *Joule*, **2018**, *2*, 509–520.

11. Zhao Z., Goncalves R. V., Barman S. K., Willard E. J., Byle E., Perry R., Wu Z., Huda M. N., Moule A. J., and Osterloh F. E.; *Energy and Environmental Science*, **2019**, *12*, 1385–1395.

12. Konta R., Ishii T., Kato H., and Kudo A.; *Journal of Physical Chemistry B*, **2004**, *108*, 8992–8995.

13. Niishiro R., Kato H., and Kudo A.; *Physical Chemistry Chemical Physics*., **2005**, *7*, 2241–2245.

14. Ohno T., Tsubota T., Nakamura Y., and Sayama K.; *Applied Catalysis A: General*, **2005**, *288*, 74–79.

15. Wang Q., Hisatomi T., Jia Q., Tokudome H., Zhong M., Wang C., Pan Z., Takata T., Nakabayashi M., Shibata N., Li Y., Sharp I. D., Kudo A., Yamada T., and Domen K.; *Nature Materials*, **2016**, *15*, 611–615.

16. Ma X., Cui X., Zhao Z., Melo M. A., Roberts E. J., and Osterloh F. E.; *Journal of Materials Chemistry A*, **2018**, *6*, 5774–5781.

17. Kato H., and Kudo A.; *Journal of Physical Chemistry B*, **2002**, *106*, 5029–5034.

18. Ishii T., Kato H., and Kudo A.; *Journal of Photochemistry and Photobiology A: Chemistry*, **2004**, *163*, 181–186.

19. Abe R., Sayama K., and Sugihara H.; *Journal of Physical Chemistry B*, **2005**, *109*, 16052–16061.

20. Liu J. W., Chen G., Li Z. H., and Zhang Z. G.; *Journal of Solid State Chemistry*, **2006**, *179*, 3704–3708.

21. Ouyang S. X., Tong H., Umezawa N., Cao J. Y., Li P., Bi Y. P., Zhang Y. J., and Ye J. H.; *Journal of the American Chemical Society*, **2012**, *134*, 1974–1977.

22. Sayama K., Mukasa K., Abe R., Abe Y., and Arakawa H.; *Journal of Photochemistry and Photobiology A: Chemistry*, **2002**, *148*, 71–77.

23. Lehuta K. A., and Kittilstved K. R.; *Dalton Transactions*, **2016**, *45*, 10034–10041.

24. Jiao Z. B., Zhang Y., Chen T., Dong Q. S., Lu G. X., and Bi Y. P.; *Chemistry: A European Journal*, **2014**, *20*, 2654–2662.

25. Wang J., Zhao J., and Osterloh F. E.; *Energy and Environmental Science*, **2015**, *8*, 2970–2976.

26. Vasquez R. P.; *Surface Science Spectra*, **1992**, *1*, 129–135.

27. Ferrer S., and Somorjai G. A.; *Surface Science*, **1980**, *94*, 41–56.

28. Benthem K. v., Elsasser C., and French R. H.; *Journal of Applied Physics*; **2001**, *90*, 6156–6164.

29. Basun S. A., Bianchi U., Bursian V. E., Kaplyanskii A. A., Kleemann W., Markovin P. A., Sochava L. S., and Vikhnin V. S.; *Ferroelectrics*, **1996**, *183*, 255–264.

30. Wang J., Fang T., Yan S., Li Z., Yu T., and Zou Z.; *Computational Materials Science*, **2013**, *79*, 87–94.

31. Comes R. B., Sushko P. V., Heald S. M., Colby R. J., Bowden M. E., and Chambers S. A.; *Chemistry of Materials*, **2014**, *26*, 7073–7082.

32. Wang Q., Hisatomi T., Ma S. S. K., Li Y., and Domen K.; *Chemistry of Materials*, **2014**, *26*, 4144–4150.

33. Takata T., and Domen K., *Journal of Physical Chemistry C*, **2009**, *113*, 19386–19388.

34. Wu P., Wang J., Zhao J., Guo L., and Osterloh F. E.; *Chemical Communications*; **2014**, *50*, 15521–15524.

35. Ma X., Wu Z., Roberts E. J., Han R., Rao G., Zhao Z., Lamoth M., Cui X., Britt R. D., and Osterloh F. E.; *Journal of Physical Chemistry C*, **2019**, *123*, 25081–25090.

36. Lide D. R., in CRC Handbook of Chemistry and Physics, CRC Press/Taylor and Francis, Boca Raton, FL, 88 (Internet Version 2008) edn, **2008**.

37. Kronik L., and Shapira Y.; *Surface Science Reports*, **1999**, *37*, 1–206.

38. Dittrich T., Fiechter S., and Thomas A.; *Applied Physics Letters*, **2011**, *99*, 084105-084101–084105-084103.

39. Gross D., Mora-Sero I., Dittrich T., Belaidi A., Mauser C., Houtepen A. J., Da Como E., Rogach A. L., and Feldmann J.; *Journal of the American Chemical Society*, **2010**, *132*, 5981–5983.

40. Nail B. A., Fields J. M., Zhao J., Wang J., Greaney M. J., Brutchey R. L., and Osterloh F. E.; *ACS Nano*, **2015**, *9*, 5135–5142.

41. Yang Y., Wang J., Zhao J., Nail B. A., Yuan X., Guo Y., and Osterloh F. E.; *ACS Applied Materials & Interfaces*, **2015**, *10*, 5959–5964.

42. Zhao J., and Osterloh F. E.; *The Journal of Physical Chemistry Letters*, **2014**, *5*, 782–786.

43. Zhao J., Nail B. A., Holmes M. A., and Osterloh F. E.; *The Journal of Physical Chemistry Letters*, **2016**, 3335–3340.

44. Melo M. A., Wu Z., Nail B. A., De Denko A. T., Nogueira A. F., and Osterloh F. E.; *Nano Letters*, **2018**, *18*, 805–810.

45. Zhao J., Nail B. A., Holmes M. A., and Osterloh F. E.; *The Journal of Physical Chemistry Letters*, **2016**, *7*, 3335–3340.

46. Osterloh F. E., Holmes M. A., Chang L., Moule A. J., and Zhao J.; *Journal of Physical Chemistry C*, **2013**, *117*, 26905–26913.

47. Osterloh F. E., Holmes M. A., Zhao J., Chang L., Kawula S., Roehling J. D., and Moule A. J.; *Journal of Physical Chemistry C*, **2014**, *118*, 14723–14731.

48. Shelton T. L., Harvey N., Wang J., and Osterloh F. E.; *Applied Catalysis A*, **2016**, *521*, 168–173.

49. Suzuki S., Honda A., Iwaji N., Higai S. I., Ando A., Takagi H., Kasatani H., and Deguchi K.; *Physical Review B: Condensed Matter and Materials Physics*, **2012**, *86*, 060102.

50. Bednorz J. G., and Muller K. A.; *Physical Review Letters*, **1984**, 52, 2289–2292.

51. Durán A., Martínez E., Díaz J. A.. and Siqueiros J. M.; *Journal of Applied Physics*, **2005**, *97*, 104109.

52. Kumar A. S., Suresh P., Kumar M. M., Srikanth H., Post M. L., Kathy S., Ralf M., and Srinath S.; *Journal of Physics: Conference Series*, **2010**, *200*, 092010.

53. Giocondi J. L., and Rohrer G. S.; *Chemistry of Materials*, **2001**, *13*, 241–242.

54. Yang S. Y., Seidel J., Byrnes S. J., Shafer P., Yang C. H., Rossell M. D., Yu P., Chu Y. H., Scott J. F., Ager J. W., Martin L. W., and Ramesh R.; *Nature Nanotechnology*, **2010**, *5*, 143–147.

55. Li L., Salvador P. A., and Rohrer G. S.; *Nanoscale*, **2014**, *6*, 24–42.

56. Burbure N. V., Salvador P. A., and Rohrer G. S.; *Chemistry of Materials*, **2010**, *22*, 5823–5830.

57. Khan M. A., Nadeem M. A., and Idriss H.; *Surface Science Reports*, **2016**, *71*, 1–31.

58. Park S., Lee C. W., Kang M.-G., Kim S., Kim H. J., Kwon J. E., Park S. Y., Kang C.-Y., Hong K. S., and Nam K. T.; *Physical Chemistry Chemical Physics*, **2014**, *16*, 10408–10413.

59. Yang S. Y., Martin L. W., Byrnes S. J., Conry T. E., Basu S. R., Paran D., Reichertz L., Ihlefeld J., Adamo C., Melville A., Chu Y. H., Yang C. H., Musfeldt J. L., Schlom D. G., Ager J. W., and Ramesh R.; *Applied Physics Letters*, **2009**, *95*, 062909.

Chapter 3 - Ferroelectric Effect Controls Water Oxidation Photoelectrochemistry in Oxygen Deficient Strontium Titanate Single Crystals

3.1 Introduction

Ferroelectric (FE) materials exhibit a spontaneous internal electric polarization that can be reversed by application of an external electric field. [1] This is of interest for applications in memory storage media, field effect transistors and ferroelectric random-access memory. [2,3] Ferroelectric materials with semiconducting properties, so called photoferroics, [2] have potential to enhance the performance of photovoltaic devices and photocatalysts. [4] This is shown in **Figure 3.1** for a $BaTiO_3$ crystal, a ferroelectric material. The electric polarization P enhances the spatial separation of electrons and the holes created under optical excitation. [4, 5] It has been shown that this promotes site specific Ag^+ reduction/Pb^{2+} oxidation activity of the material [6, 7] and enhances the photocatalytic dye degradation rate by a factor of 3. [8] Similarly, for Sr-doped $PbZrO_3$, photocatalytic hydrogen evolution was doubled after polarization along the z-axis and greatly suppressed when the applied electric field was reversed. [9] In $BiFeO_3$ one observes an anomalous photovoltaic effect (APE) with increased open-circuit voltages of up to 16 V. [10, 11] Generally, to be a ferroelectric, a crystalline phase must not crystallize in a centrosymmetric space group, which cannot possess a permanent dipole. For example, while the tetragonal form of $BaTiO_3$ in **Figure 3.1** is ferroelectric, the cubic phase is not.

For this reason, cubic $SrTiO_3$ in space group Pm3m is not a ferroelectric material, however, at low temperature (Curie temperature 105 K) the ferroelectric tetragonal form in space group I4/mcm can form. [14] Recent experimental evidence and theoretical calculations also suggests that room temperature ferroelectricity in cubic $SrTiO_3$ can become possible with the introduction of defects (**Figure 3.1d**), which breaks the centrosymmetry of the unit cell. For example, $SrTiO_3$ thin films grown on $GdScO_3$ (110)

substrates exhibit room temperature ferroelectric polarization as a result of the tensile distortion induced by the substrate. [15]

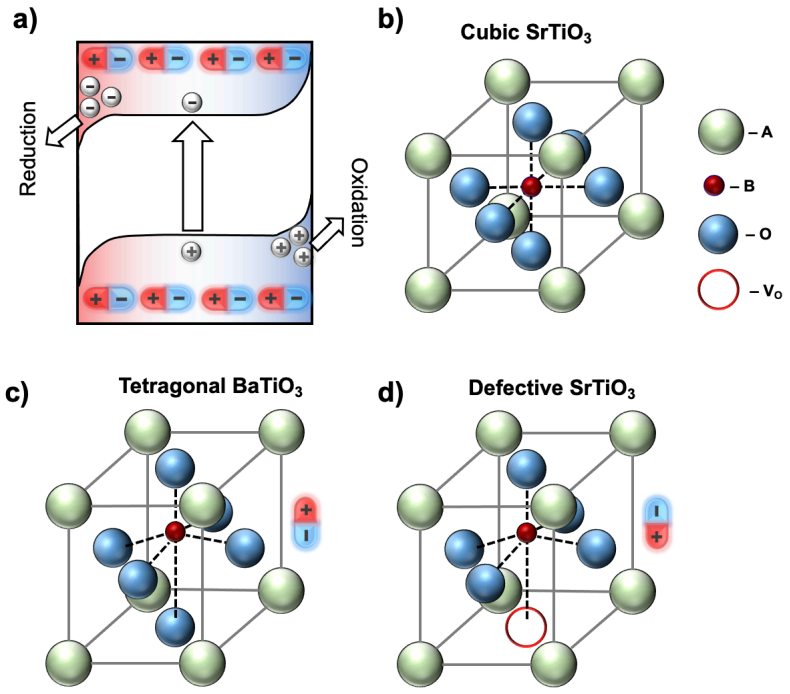

Figure 3.1. a) Ferroelectric polarization effect on band bending in a photovoltaic junction. The slope of the band edges is equivalent to a built-in field (E_{bi}). From ref. 12. b) Cubic strontium titanate unit cell in cubic ABO_3 perovskite structure (A = Sr^{2+} B = Ti^{4+} O = O^{2-}). c) Tetragonal barium titanate unit cell (A = Ba^{2+}, B = Ti^{4+}, O = O^{2-}). [13] d) Defective strontium titanate unit cell, containing one oxygen vacancy (VO).

Ferroelectric behavior in cubic $SrTiO_3$ has also been predicted theoretically as a result of the introduction of oxygen vacancies [16-18] or Frenkel defects. [19] Indeed, Chu et.al confirmed experimentally that polarization – electric field (PE) curves of chromium doped $SrTiO_3$ films exhibit hysteresis behavior. [20] Similarly, after doping chromium into strontium titanate nanocrystals, Assavachin observed an anomalous surface photovoltage signal of 6.4 V that was dependent on a prior applied electrical field. [21] While research into

these materials is ongoing, [22-28] it is unclear if this non-traditional defect-induced ferroelectric effect can be utilized to improve solar energy conversion.

To address this point, we studied the photoelectrochemical water oxidation properties of [111]-oriented $SrTiO_3$ single crystals after introduction of oxygen vacancies. We find that applied electric fields increase or reduce the photovoltage and photocurrent, depending on the orientation of the field. This is attributed to a defect-induced FE effect. In argon atmosphere, this FE enhancement is retained for 24 h, but in air it disappears in less than 24 h. Based on theoretical modeling, the FE enhancement can be attributed to the migration of oxygen vacancies near the surface. These results provide the first example of the use of a defect-induced ferroelectric effect for photoelectrochemical energy conversion with $SrTiO_{3-x}$.

3.2 Results and Discussion

The commercial $SrTiO_3$ single crystals for this study are 1.0 x 1.0 cm^2 x 0.50 mm in size (**Figure 3.2a**) and are terminated by [111] facets (SEM in **Figure 3.2b**). The [111] orientation is verified by x-ray diffraction in **Figure 3.2c**. The crystals are colorless and transparent in the visible and optical absorption spectra with an absorption edge at 390 nm (3.2 eV) corresponding to the known 3.2 eV optical bandgap of strontium titanate. [29] The crystals are electrically insulating but can be made semiconducting by annealing in a 10 % H_2 / 90 % Ar for 5 hours at 1,050°C according to the protocol used by Mavroides. [29] The resulting crystals are grey and have a broad optical absorption at > 400 nm (**Figure 3.2d**), that is due to free electron excitation in the $SrTiO_{3-x}$ conduction band. [30, 31] The free carriers are formed by thermal excitation of electrons from Ti^{3+} generated by reduction with H_2. Additionally, the weak absorption at 510 nm is attributed to $^2T_{2g} \rightarrow {}^2E_g$ transition of Ti^{3+} in octahedral environment. [32]

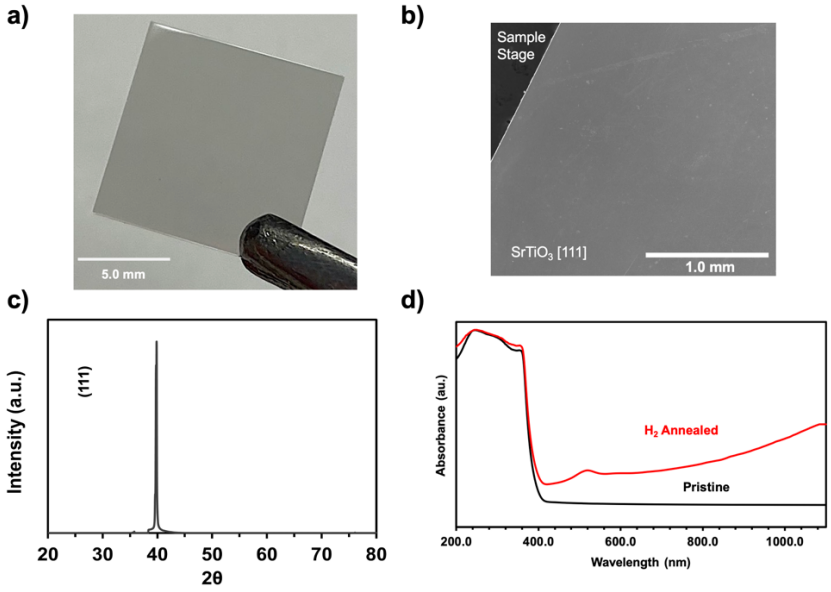

Figure 3.2. a) Images of (111) $SrTiO_3$ single crystal. b) SEM image of $SrTiO_3$ single crystal surface after H_2 annealing. c) XRD Pattern of H_2 annealed $SrTiO_3$ [111] single crystal. d) Optical absorbance spectra before and after H_2 annealing.

The photoelectrochemical (PEC) water oxidation properties of the $SrTiO_{3-x}$ crystal were assessed by placing the crystal into of a three-electrode cell (**Appendix 3.7a**), using a Pt counter electrode, a calomel reference electrode, and an aerated 0.50 M Na_2SO_4 aqueous solution (pH = 5.95). The crystal was contacted electrically with InGa alloy to promote an Ohmic contact, and its back side was covered with polyester masking tape to shield it from the electrolyte. A chopped light photoelectrochemical experiment was conducted using 60 mW cm^{-2} ultraviolet light from a Xe lamp. As can be seen in **Figure 3.3a**, at applied potentials positive of -0.20 V RHE, the $SrTiO_{3-x}$ sample produces an anodic photocurrent of 0.99 mA cm^{-2} at 1.23 V RHE. The current is stable for one hour (**Appendix 3.8**) and attributed to water oxidation as evidenced by formation of a gas at the working electrode (**Appendix 3.9**), movie in supporting information). The external quantum efficiency is 52.69 % at 1.23 V RHE under 375 nm LED illumination

(**Appendix 3.10** and **Table 3.1**). These values are comparable to a previous study. [33] The photocurrent of $SrTiO_3$ is known to be limited by carrier recombination at oxygen vacancy induced Ti^{3+} defects. [34] Higher quantum efficiencies can be achieved after removal of the Ti^{3+} defects by doping with aliovalent ions (Na^+, Ga^{3+}, Al^{3+}). [35, 36]

In order to observe the effect from an electric polarization on the photoelectrochemical behaviour of oxygen vacancy rich $SrTiO_{3-x}$, the crystal was exposed to an electric field, as shown in **Appendix 3.7b**. The crystal is sandwiched between two 2.0 x 4.0 cm^2 gold coated glass slides from which it was separated by two Muscovite mica sheets (~65 μm thick each) for electrical insulation. The sandwich was then placed inside a glass tube that was continuously purged with argon gas and the two gold contacts connected to a DC voltage of 545 V for one hour. Voltage was measured with a digital multimeter and using a voltage divider consisting of 0.499 MΩ and 49.3 kΩ resistors in series. Based on the thickness of the stack (0.050 cm + 2 x 0.0065 cm), the effective electric field acting on the $SrTiO_{3-x}$ crystal was 8.65 kV cm^{-1}. Within 30 minutes after polarization, the photoelectrochemical properties of the crystal were evaluated as described before. The PEC response for a forward polarized crystal (exposed surface was near positive electrode in **Appendix 3.7b**) is shown in **Figure 3.3a** (blue line). The anodic current begins at -0.20 V vs RHE and reaches 2.22 mA cm^{-2} at +1.23 V RHE. This corresponds to an IPCE of 71.35 % at 375 nm (at +1.23 V RHE). The photocurrent is 2.2 times larger than before, but the onset remained the same at -0.20 V vs RHE. PEC measurement for a reverse polarized crystal (exposed surface near negative electrode) is also shown in **Figure 3.3a** (green line). For the reverse polarized crystal, the current begins at -0.20 V vs RHE and reaches only 0.50 mA cm^{-2} at 1.23 V RHE (IPCE 48.82%), 1.99 times lower than what is found for the non-polarized crystal. This shows that forward and reverse polarization increases or decreases the anodic photocurrent of $SrTiO_{3-x}$ by a factor of ~2. These polarization effect on the photocurrent is reproducible with different $SrTiO_{3-x}$ crystals, as shown in **Appendix 3.11** and **Table 3.2**. On average, the photocurrent increases by a

factor of 1.83 ± 0.45 (24.6%) or decreases by a factor of 1.93 ± 0.49 (25.4%) for forward and reverse polarization respectively.

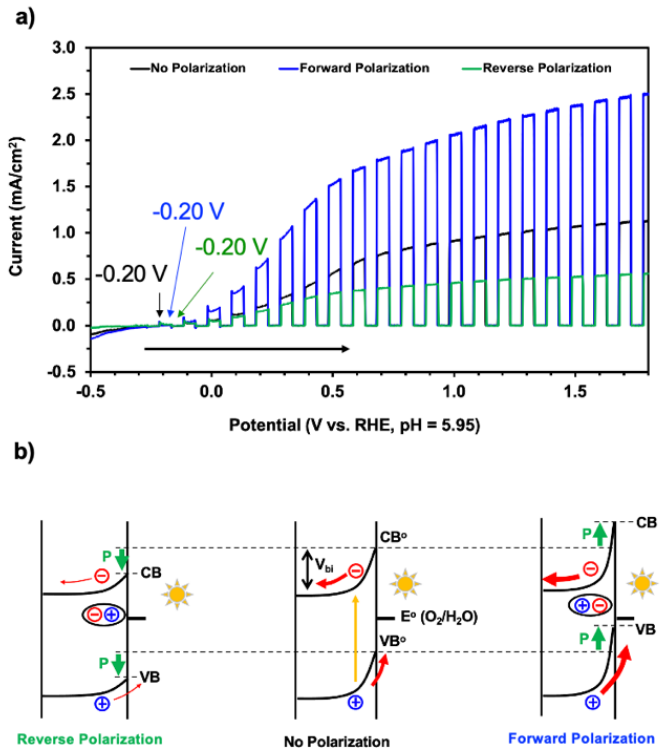

Figure 3.3. a) Chopped light linear sweep voltammetry of 10 % H_2 annealed $SrTiO_3$ under 300 W Xe lamp UV light illumination (60 mW cm^{-2}) with 5 s on/off interval; The single crystal back contact is coated with InGa eutectic to establish an Ohmic contact. b) Proposed band bending diagram for the $SrTiO_{3-x}$/liquid junctions during PEC water oxidation. CB^0 and VB^0 denote the conduction and valence band edges for the non-polarized film. V_{bi} is the built-in voltage. Voltametric scans were conducted from negative to positive applied potential.

The differences in the photoelectrochemical activity can be explained with the energy diagram in **Figure 3.3b**. The $SrTiO_{3-x}$/liquid interface forms a Schottky type junction that under illumination guides photogenerated holes into the liquid and electrons into the back contact. [33, 37] The electric polarization

creates a ferroelectric dipole near the $SrTiO_{3-x}$ surface, which increases or decreases the potential drop across the depletion region by an amount, P. This modifies the built-in potential of the depletion layer and, accordingly, the photocurrent of the samples.

To further assess the effect of the surface dipole on charge separation, surface photovoltage spectra were collected for the $SrTiO_{3-x}$ samples in contact with liquid water (**Figure 3.4a**). For this, the $SrTiO_{3-x}$ crystal surface was coated with 15 μL of deionized water and a microscopy glass cover slide. Samples were then placed 2 mm underneath a vibrating gold Kelvin probe to measure the contact potential difference change under illumination (**Appendix 3.7c**). All samples generate a negative SPV signal at energies above 3.15 eV, near the optical bandgap of $SrTiO_{3-x}$. The negative SPV signal is caused by photoholes reaching the $SrTiO_{3-x}$/liquid interface and electrons moving to the back contact, as shown in **Figure 3.3b**. The forward polarized sample produces the strongest SPV signal and the reverse polarized sample the weakest. This agrees with the band diagrams and the anodic photocurrent trends in **Figure 3.3**.

To probe the effect of the polarization on the flatband potential of $SrTiO_{3-x}$, Mott Schottky measurements were conducted in 0.50 M Na_2SO_4 aqueous solution with equimolar $K_{3/4}[Fe(CN)_6]$ electrolyte and under exclusion of air. As can be seen in **Figure 3.4b**, all MS plots produce a positive slope associated with an n-type depletion layer. The slopes for all samples are similar, as expected for this single crystal, and correspond to a free electron concentration between 1.8×10^{19} and 2.2×10^{19} cm^{-3} (calculation details in **Appendix 3.12**). Importantly, values for the flat band potentials are found to increase from the forward polarized (-0.321 V vs RHE) to the non-polarized (-0.288 V vs RHE) and the reverse polarized samples (-0.246 V vs RHE). This is an important confirmation of the model in **Figure 3.3b**, which predicts an impact of the ferroelectric polarization not just on the photocurrent, but also on the flatband potential. Surprisingly, this flatband potential variation does not appear to shift the water oxidation photoonset potentials in **Figure 3.3a**. This appears to be a consequence of the accumulation of positive charge at the $SrTiO_{3-x}$ interface

during the slow water oxidation reaction. Oxygen is also known to have a strong Fermi level pinning effect in $SrTiO_3$, which can mask the influence of the FE polarization on the photoonset potential. [38, 39]

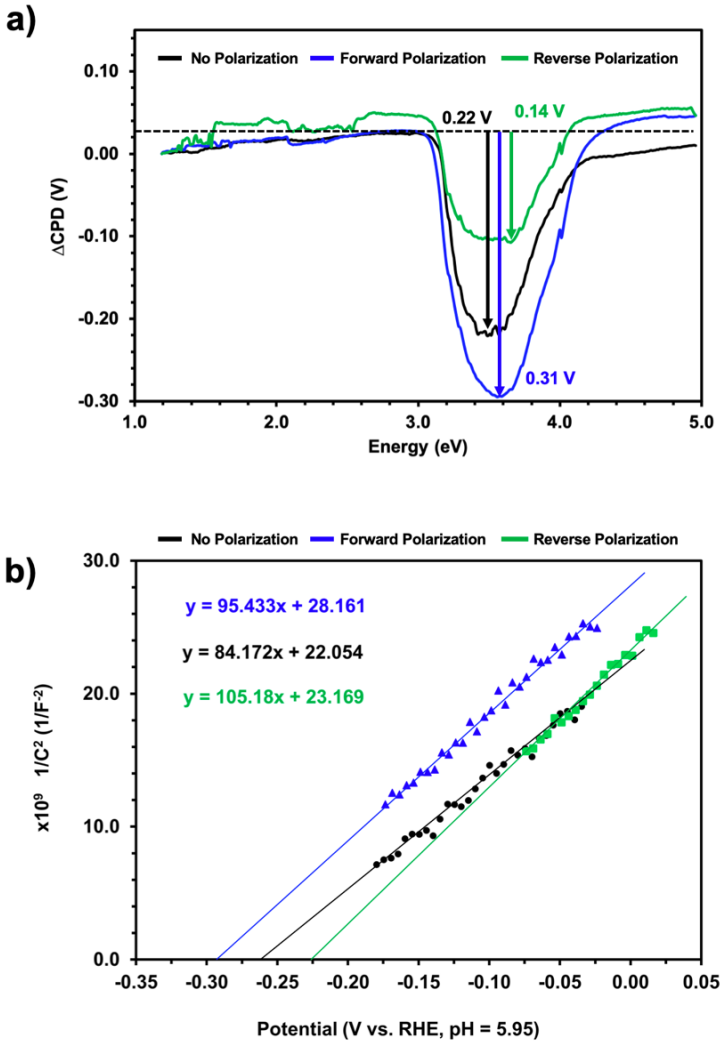

Figure 3.4. a) Surface photovoltage spectra of $SrTiO_{3-x}$ in contact with 15 µL deionized water and air saturated with water. The SPV signal reaches its maximum value at 3.4 – 3.6 eV and then decays to zero above 4.0 eV, as a result of the diminishing intensity of the light source (Xe Lamp). b) Mott Schottky measurement of $SrTiO_{3-x}$ crystals in 0.50 M Na_2SO_4 aqueous solution with 50 mM equimolar $K_{3/4}[Fe(CN)_6]$ (air free). The AC frequency was 100 Hz. $SrTiO_{3-x}$ crystals were contacted with InGa eutectic and the back side covered with polyester masking tape. The area exposed to the liquid was 0.50 cm^2.

To assess the lifetime of the FE polarization in $SrTiO_{3-x}$, chopped light LSV scans were repeated 24 h and 48 h after the initial electric field treatment (**Figure 3.5**). It can be seen that polarization effects disappear completely within a 24 h interval for samples stored in air, but is retained up to 48 h for samples stored in argon atmosphere. In the latter case, 100 % of the FE enhancement obtained from forward polarization is present after 24 h and 53 % after 48 h. Similarly, 83 % of the FE suppression from reverse polarization is retained after 24 h but disappears after 48 h. This shows that the polarization effect is air-sensitive and likely connected to the chemistry at the $SrTiO_{3-x}$ surfaces.

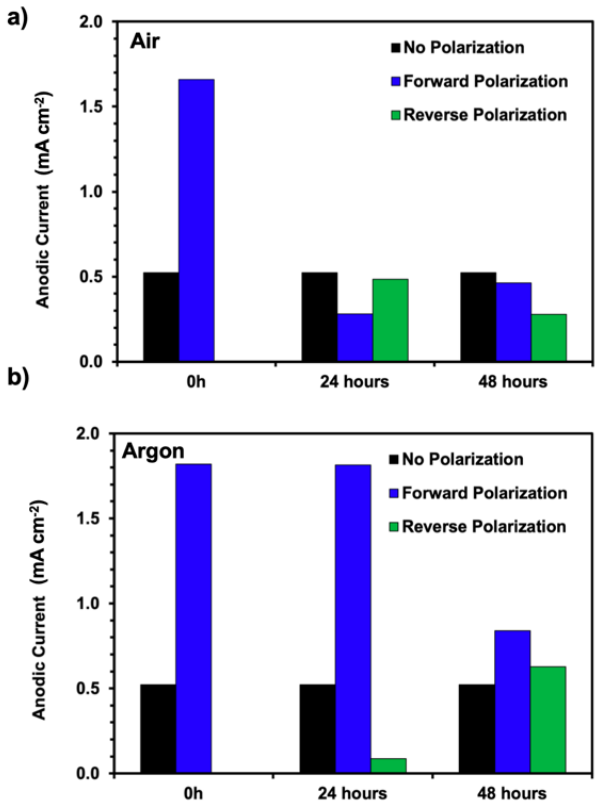

Figure 3.5. PEC water oxidation photocurrent at 1.23 V RHE at the indicated times after initial polarization. a) Sample storage in the dark in air, b) Sample storage in the dark under argon flow. PEC testing was performed by contacting samples with an iron clip to avoid chemical interference from the InGa alloy.

To better understand the effect of the H_2 treatment and of the electric polarization on the surface chemistry of $SrTiO_{3-x}$, X-ray photoelectron spectroscopy (XPS) was employed. High resolution data for the Ti and O regions is shown in **Figure 3.6**. Additional data and survey spectra are shown in **Appendix 3.13**, **3.14**, and **Table 3.3**.

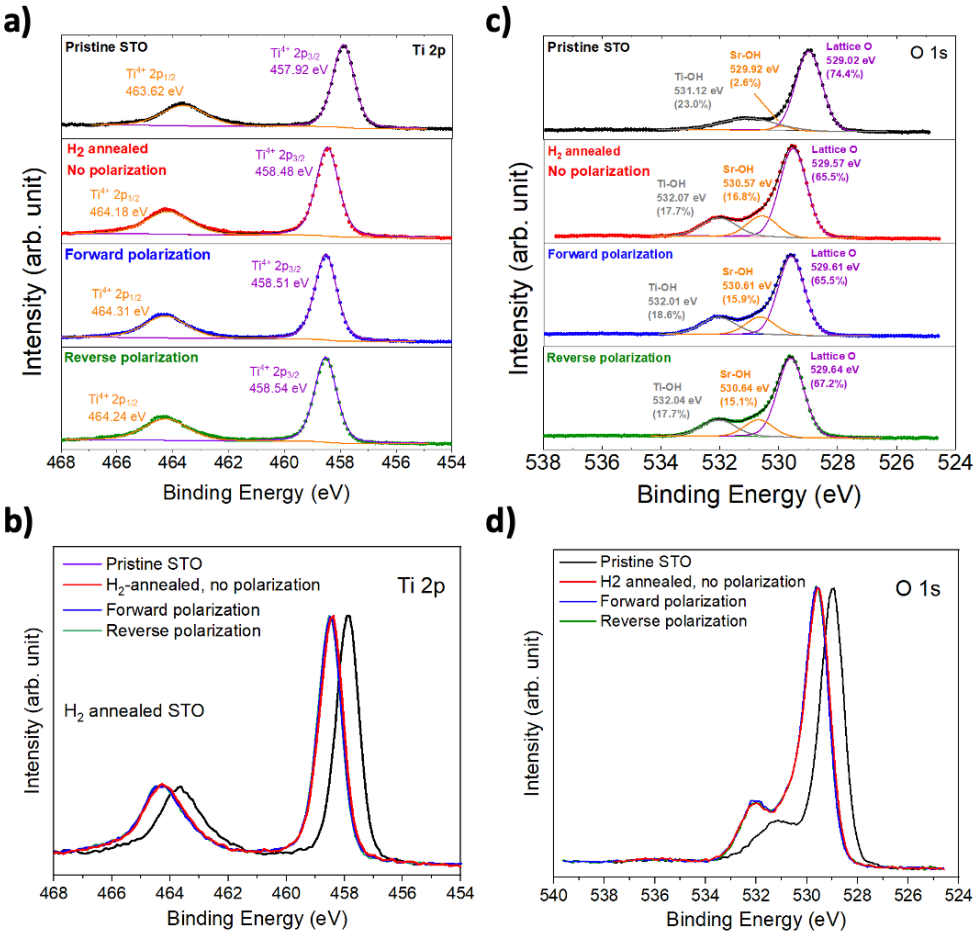

Figure 3.6. a) Peak fit and b) overlap of the Ti 2p spectra of pristine $SrTiO_3$ (purple), H_2-annealed $SrTiO_{3-x}$ without polarization (red), with forward polarization (blue) and reverse polarization (green), respectively. c) Peak fit and d) overlap of the O 1s spectra. Data from Chengcan Xiao, reproduced with permission.

For the as-purchased pristine $SrTiO_3$ single crystals, the Sr $3d_{5/2}$ peak at 132.42 eV, Ti 2p3/2 peak at 457.92 eV and O 1s peak at 529.02 eV match the results from other literatures. [40-44] All titanium is in the 4+ oxidation state. The two O 1s peaks are assigned to lattice O and surface OH groups, respectively. After H_2 annealing, a binding energy shift towards higher energy for all 3 elements was detected, suggesting a Fermi level shift toward more reducing potentials. This is evidence of an increase of free electrons in $SrTiO_{3-x}$ (see earlier discussion in Zhao et al.[34]) Based on the 0.55 eV shift for Ti $2p_{3/2}$ (457.92 to 458.48 eV) and O 1s (529.02 eV to 529.57 eV), and the slightly larger shift of 0.61 eV for Sr $3d_{5/2}$ (132.42 to 133.02 eV), the average Fermi level change in $SrTiO_{3-x}$ is 0.58 eV. Interestingly, no Ti^{3+} was detected, which is attributed to the small penetration depth of XPS (5 nm). Any formed surface Ti^{3+} undergoes air oxidation to Ti^{4+} with concomitant formation of peroxide and hydroxide. This additional hydroxide gives rise to a new O 1s peak at 530.57 eV in **Figure 3.6c**, which is assigned to surface Sr-OH hydroxide species according to the work by Hrabovsky et al. [42] Preferred –OH binding to Sr^{2+} is likely due a result of the stronger Broenstedt basicity of Sr-O compared to Ti-O. This also causes the larger binding energy shift of Sr peaks (see discussion above). The remaining two oxygen peaks at 529.57 eV and 532.07 eV are assigned to lattice O and surface Ti-OH, respectively.

Survey and high resolution XPS spectra for $SrTiO_{3-x}$ measured within the first hour after forward and reverse polarization are shown in **Appendix 3.13**, respectively. No significant changes in the relative intensity and peak positions were found after these treatments. However, when high resolution Ti spectra are overlayed in **Figure 3.6b**, a small shift of the Fermi level relative to non-polarized $SrTiO_{3-x}$ can be seen. The shift of 0.04-0.07 eV is much smaller than the Fermi level shift after H_2 annealing (0.58 eV), and occurs in the direction of higher energy, regardless of polarization direction. We attribute it to the removal of surface water from argon exposure during the one-hour polarization treatment of the $SrTiO_{3-x}$ crystals. Overall, the XPS data suggests that electric polarization is not associated with significant changes in the

chemical surface composition of the $SrTiO_{3-x}$ wafer and the observed polarization effect is possibly due to a ferroelectric polarization.

3.3 Conclusion

In conclusion, we have successfully introduced oxygen vacancies into strontium titanate single crystal with 111 exposed facets. The increased oxygen vacancy not only improves the PEC activity under UV light illumination, but also induces a ferroelectric effect that can be controlled with an applied electric field. Polarization in the forward direction increases the water oxidation photocurrent under UV light more than two-folds (1.83 ± 0.45 (24.6 %)) at 0.0 V vs RHE while reverse bias suppresses it by a factor of two (1.93 ± 0.49 (25.4 %)). SPS shows carrier movements consistent with the PEC results. These findings can be explained with junction model, which assumes that the band bending at the $SrTiO_{3-x}$/liquid interface is modified by a ferroelectric surface dipole. The dipole induced shift is verified experimentally with Mott Schottky measurements, which reveal a shift of the flatband potential -0.033 eV to more reducing or +0.042 eV to more oxidizing values, upon forward and reverse polarization, respectively. Although the polarization effect only lasts 24 h in air, argon storage extends its lifetime up to 48 hours. This suggests that the polarization is predominantly a surface effect. This work provides the first verification that oxygen vacancy-induced ferroelectricity in $SrTiO_{3-x}$ can be used to improve photoelectrochemical energy conversion with this material. Further work involving DFT calculations would be beneficial to elucidate the origins of the electric dipole observed and to verify the ferroelectric polarization of $SrTiO_{3-x}$.

3.4 Experimental Section

Water was purified to 18 MΩ cm resistivity using a nano-pure system. Double polished single crystals of strontium titanate with 111 exposed facets and 10 x 10 x 0.50 dimensions in millimeters were purchased from MSE Supplies. Sodium sulfate (99.5%, Sigma Aldrich), potassium hexacyanoferrate (II) trihydrate (98.5%-102.0%, Sigma-Aldrich), potassium ferricyanide (III) (99.9%, Fischer Chemical – Fischer Scientific), gallium indium eutectic (InGa, ≥99.99% trace metal basis, Aldrich Chemistry), and gold coated glass (Thermo Scientific) were used as purchased.

Preparation of $SrTiO_{3-x}$

$SrTiO_{3-x}$ crystals were annealed in a ceramic boat under 10 % H_2: 90 % flowing argon gas (0.1 L min^{-1} : 0.9 L min^{-1}). The initial flow rate was zero until the heating temperature reached 150^{o}C to eliminate water. The ramp rate was 50^{o}C/min and the single crystal was annealed at 1,050^{o}C for 5 hours before cooling to room temperature naturally. The obtained $SrTiO_{3-x}$ crystal was grey.

Electrical Polarization

The electrical polarization of the single crystal is depicted in (**Appendix 3.7b**), along with their respective nomenclature. To prevent direct contact with gold substrates, mica sheets (≤65 μm thick each) were used as a separation layer. The power supply input was set to 3.0 V and 340 mA, and a DC-HVDC Converter from the FS Series (XP Power) was employed to achieve an output voltage of approximately 545 V. Voltage was measured with a digital multimeter and using a voltage divider consisting of 0.499 MΩ and 49.3 kΩ resistors in series. The electrical bias was applied for 1 hour in either direction under a continuous argon flow of 1.0 L min^{-1} at room temperature. In the "Forward polarization" configuration, the “front side” of the single crystal, which is not covered by the polyester tape, was exposed to the positive electrode.

Conversely, in the "Reverse polarization" configuration, the front side was exposed to the negative electrode. It is important to note that the polyester tape was not present during the electrical polarization stage; it was only used in the electrochemistry measurements to isolate the effects of the front side from the back side.

Photoelectrochemistry Measurement

Electrochemistry measurements were conducted using a Gamry Reference 600 Potentiostat connected to a three-electrode system. The system consisted of a $SrTiO_{3-x}$ single crystal working electrode with the backside covered by polyester masking tape, platinum counter electrode, and a calomel reference electrode (3.5 M KCl). Linear sweep voltammetry (LSV) was conducted in a quartz three-neck flask containing a 0.50 M Na_2SO_4 aqueous electrolyte solution (pH = 5.95). The LSV measurements were carried out under UV-light illumination from a 300 W Xe lamp source at an intensity of 60 mW cm^{-2} in air. The experimental setup is depicted in **Appendix 3.7a**. Photoelectrochemistry (PEC) measurements were performed with 5-second interval chopped light illumination. The scans were conducted at a scan rate of 10 mV/s with a scan step of 1 mV, starting from negative to positive applied potential. The potential values were converted from V vs. SCE to V vs. NHE using the half-wave potential of the cyanohexaferrite/ferrate redox couple, and then further converted from NHE to RHE, where RHE = NHE + (pH x 0.059V). IPCE measurements were conducted using chronoamperometry with an applied bias of +1.23 V vs. RHE at pH = 5.95. The bias was applied throughout the measurement using a 375 nm LED light source (17.0 V / 240 mA). Mott-Schottky measurements were performed with a 10 mV rms AC voltage at a frequency of 100 Hz. These measurements were conducted in the dark using a sealed three-neck flask with constant nitrogen purging. The electrolyte used for Mott-Schottky measurements was $K_3[Fe(CN)_6]$/ $K_4[Fe(CN)_6]$ (50 mM each). Contact with the working electrode for Mott-Schottky measurements was made using an InGa eutectic. The backside of the crystal was covered with polyester masking tape to prevent contact with the solution.

Ambient / Argon Storage

$SrTiO_3$ single crystals were stored either at ambient conditions or under argon gas flow (1.0 L min^{-1}). In both storage methods, the samples were protected from direct light exposure. After each PEC measurement, the sample was rinsed twice with deionized water and gently wiped with a kimwipe. It was then allowed to air dry for 5 minutes. For ambient condition storage, the single crystal was placed in a closed lid plastic container at room temperature. In the case of argon storage, the single crystal was placed on a ceramic boat crucible and stored in a tube under continuous argon flow at 1.0 L min^{-1}. Polarization was performed only once at the beginning of the PEC measurement before all subsequent measurements and storage procedures were conducted.

Surface Photovoltage Spectroscopy

SPS measurements were accomplished using a vibrating gold mesh Kelvin probe (Delta PHI Besocke) mounted inside a vacuum chamber (**Appendix 3.7c**). Deionized water (15 μL) was added to the surface of $SrTiO_{3-x}$ crystal and covered with glass slide to prevent direct gold kelvin probe contact to the liquid solution. N_2 gas was flowed at a rate of 1.0 L min^{-1} through two deionized water baths before reaching the SPS chamber, the N_2 flow was allowed to fill and purge the chamber for 15 minutes. Sample is illuminated with monochromatic light range of 1.2 – 5.0 eV using a 300 W Xe lamp filtered by a monochromator (Oriel Cornerstone 130, 1-10 mW cm^{-2}). Samples were left to equilibrate under an open shutter at 9,600 cm^{-1} until stable baseline is obtained before spectrum scanning from 9,600 – 40,000 cm^{-1} with scans interval of 5 seconds and 100 cm^{-1} illumination increment.

X-ray Photoelectron Spectroscopy

XPS was conducted via Supra XPS spectrometer with Al Kα source that generate x-ray at 1,487 eV. All analysis was done in the ultra-high vacuum (UHV) analytical chamber with the pressure of 10^{-7} mbar. The spectra were electrostatically corrected based on the position of C 1s (284.8 eV). $SrTiO_3$ single crystal pristine as bought or after H_2 annealed were surveyed for O 1s, Ti 2p, Sr 3d, and survey spectrum scan. Polarized samples were analyzed within 60 minutes after polarization.

3.5 Appendix

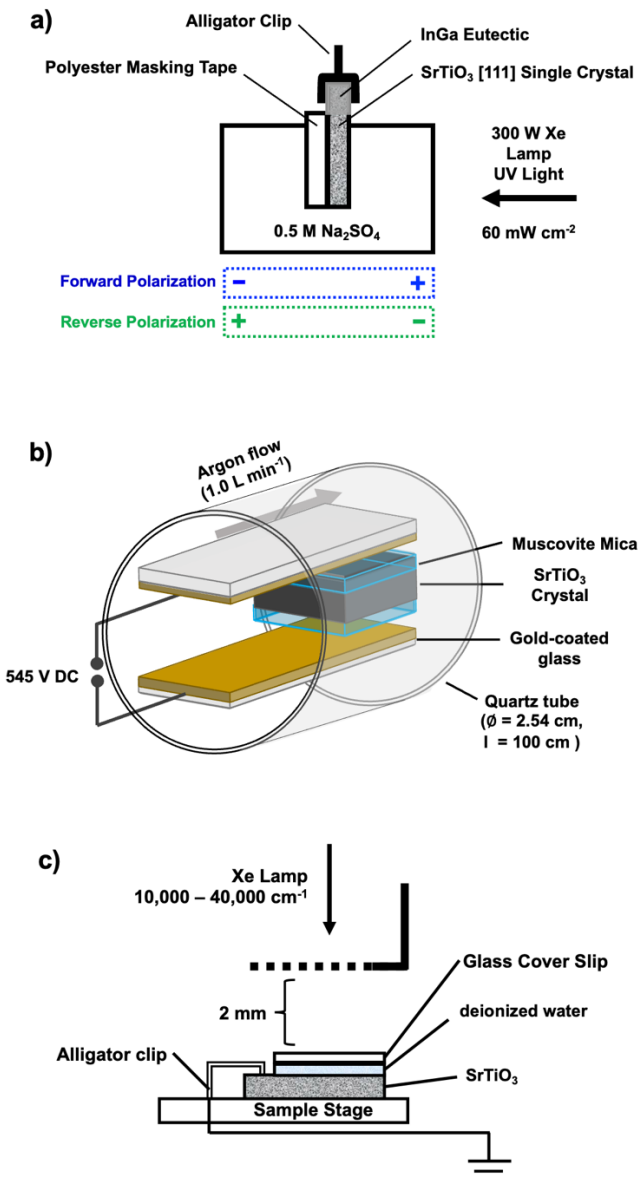

Figure 3.7. a) Photoelectrochemical measurement configuration. Ohmic contact is established using InGa eutectic, and the back of the $SrTiO_{3-x}$ crystal is covered with polyester masking tape. b) Sample configuration during electric polarization. Two gold-coated glass substrates serve as electrodes and two mica crystals (~65 µm thickness) serve as insulators. Conditions: argon atmosphere, room temperature, ± 8.65 kV cm^{-1} electric field. c) Surface Photovoltage Spectroscopy set up with liquid 0.50 M Na_2SO_4 contact under monochromatic illumination with Xe lamp source. Conditions: air saturated with water vapor.

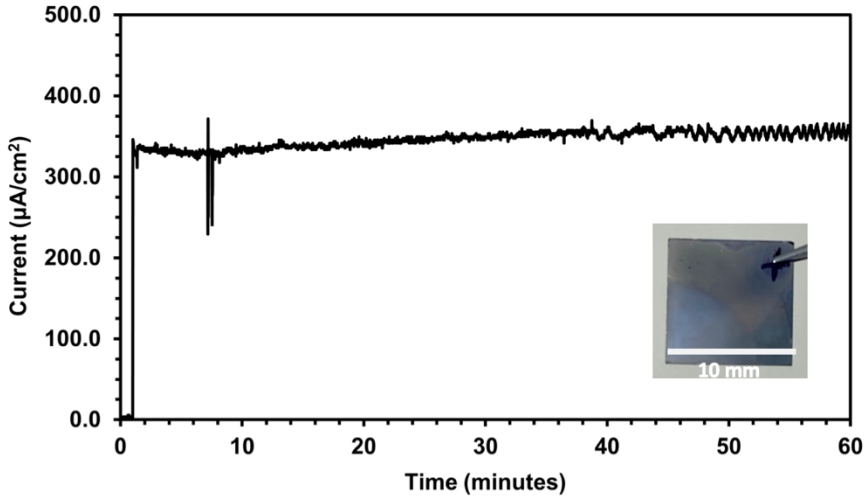

Figure 3.8. Chronoamperometry at +0.70 V vs RHE in 0.50 M Na_2SO_4 aqueous solution (pH = 5.95) under 300 W Xe Lamp UV light illumination, intensity = 60 mW/cm2 on a non-polarized H_2 annealed $SrTiO_{3-x}$ single crystal with 111 exposed facet. The film changed color (see Figure in inset) during this measurement.

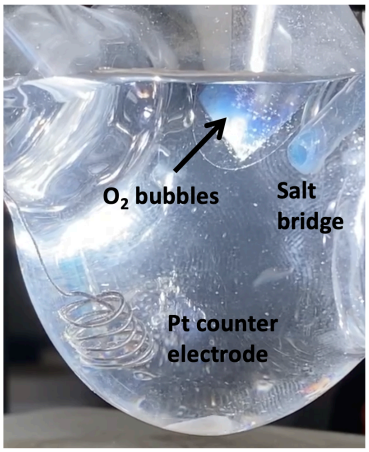

Figure 3.9. Gas bubbles form during PEC scan (H_2 annealed $SrTiO_{3-x}$ with UV illumination (60mW cm^{-2}) from Xe Lamp source in 0.50 M Na_2SO_4 (pH = 5.95) solution with +0.70 V vs RHE applied potential). See movie in supporting information.

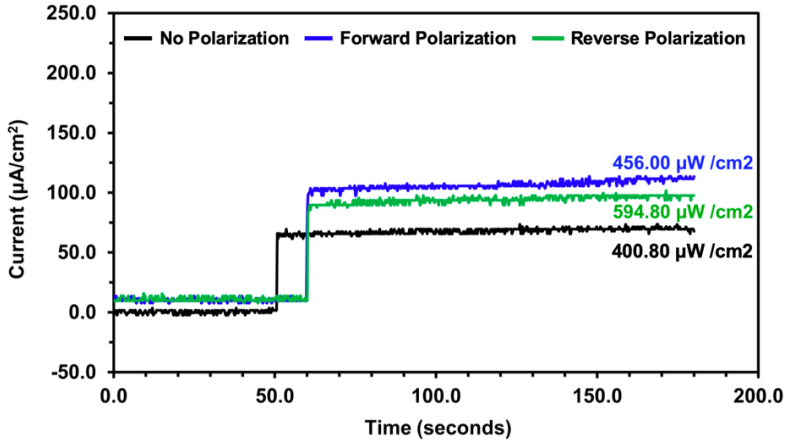

Figure 3.10. Chronoamperometry for $SrTiO_{3-x}$ with dark background and illumination using 375 nm (3.30 eV) LED light in 0.50 M Na_2SO_4 (pH = 5.95) solution with +1.23 V vs RHE applied potential. Dark background for neutral = 50 s, reverse/forward bias = 60 s. Lamp intensity was remeasured for each measurement.

Table 3.1. Photocurrent and IPCE values for $SrTiO_{3-x}$ electrodes under 375 nm LED illumination corresponding to the data in **Appendix 3.10**.

$SrTiO_3$ [111] Polarization Direction	Energy (eV)	Input Power ($\mu W/cm^2$)	Current ($\mu A/cm^2$)	IPCE (%) at 1.23 V vs RHE
No Polarization	3.3	400.80	63.99	52.69
Forward Polarization	3.3	456.00	98.59	71.35
Reverse Polarization	3.3	594.80	87.99	48.82

$$output\ power\ \left(\frac{mW}{cm^2}\right) = voltage\ (V)\ \times\ current\ \left(\frac{mA}{cm^2}\right)$$

$$power\ conversion\ efficiency\ (\%) = \frac{output\ power(mW/cm^2)}{input\ power(mW/cm^2)}$$

$$Incident\ Photon\ to\ Charge\ Efficiency\ (\%) = \frac{current\ (mA/cm^2)}{input\ power(mW/cm^2)} \times \frac{1240}{\lambda(nm)}\ \times\ 100\%$$

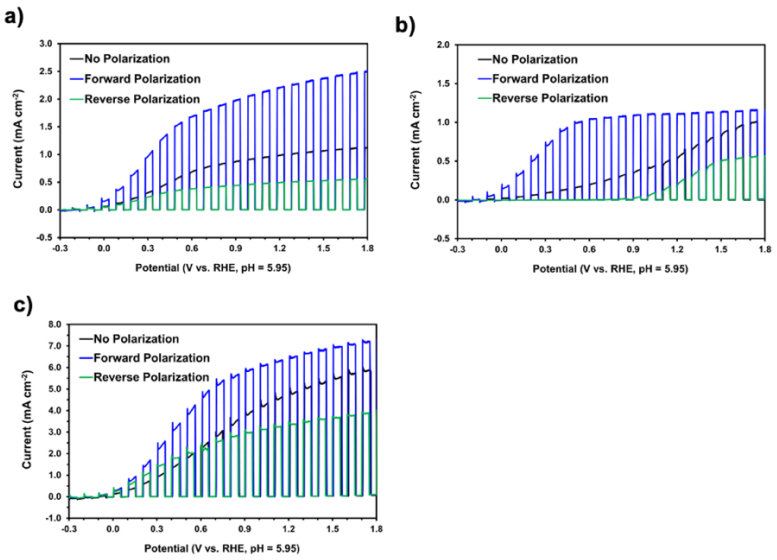

Figure 3.11. PEC activity of different batches of (111) H_2-annealed $SrTiO_{3-x}$ single crystals. a) Trial 1 (same as in **Figure 3.3**) with InGa eutectic contact. b, c) Trial 2 and 3, respectively, with stainless steel alligator clip as a contact. Variations in E_{on} and I_{SC} are a result of electron donor concentration variations caused by differences in H_2 annealing conditions.

Table 3.2. Statistical analysis corresponding to the data in **Appendix 3.11**.

Current Change Factor at 1.23V vs RHE	Trial 1	Trial 2	Trial 3	Mean	Standard Deviation (absolute, %)
Photocurrent Change Factor at 1.23 V RHE, from Non-to-Forward Polarization	2.24	1.90	1.35	1.83	0.45, 24.6
Photocurrent Change Factor at 1.23 V RHE, from Non-to-Reverse Polarization	1.99	2.39	1.42	1.93	0.49, 25.4

Mott-Schottky Equation

$$\frac{1}{C^2} = \left(\frac{2}{\varepsilon\varepsilon_0 A^2 e N_D}\right)\left(V - V_{FB} - \frac{k_B T}{e}\right)$$

Determination of Donor Concentration, N_D, by slope

$$slope = \frac{2}{\varepsilon\varepsilon_0 A^2 e N_D}$$

A = 0.0001 m^2
ε = 300
ε_0 = 8.854 x 10^{-12} C V^{-1} m^{-1}
e = 1.6022 x 10^{-19} C

Determination of Flat Band Potential, V_{FB}, by x-intercept

$$V_{FB} = V - \frac{k_B T}{e}$$

k_B = 1.380649 x 10^{-23} J K^{-1}
T = 298.15 K
e = 1.6022 x 10^{-19} C
V = x-intercept (V vs RHE)

Figure 3.12. Doping density (N_D) calculated from Mott-Schottky slope at 100 Hz, where area = 0.5 cm^2, and using dielectric constant of $SrTiO_3$ at 298 K. Flatband potential is determined from the intercept with the x-axis on the linear plot of C^{-2} versus V and converted from SCE to RHE.

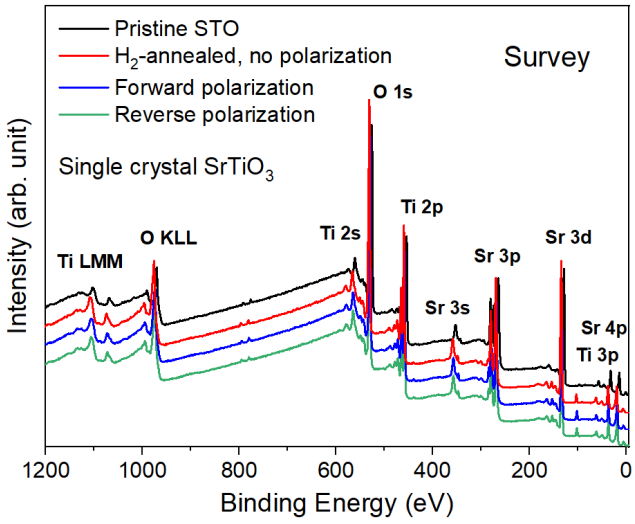

Figure 3.13. Survey scans of pristine single crystal $SrTiO_3$ (black) and H_2 annealed single crystal $SrTiO_{3-x}$ without polarization (red), with forward polarization (blue) and reverse polarization (green). A small Si 2p

peak at 102 eV in all $SrTiO_{3-x}$ samples is from the ceramic crucible used for the H_2 treatment. Data from Chengcan Xiao, reproduced with permission.

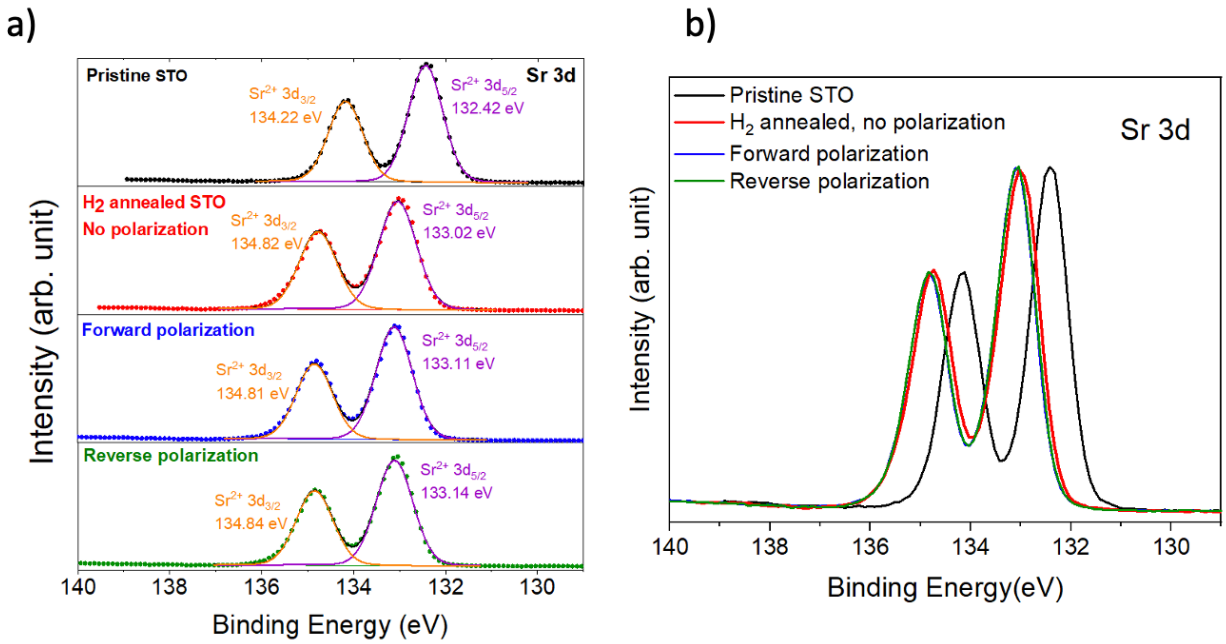

Figure 3.14. a) Peak fit and b) overlap of the Sr 3d spectra of pristine $SrTiO_3$ (black), H_2 annealed $SrTiO_{3-x}$ without polarization (red), with forward polarization (blue) and reverse polarization (green), respectively. Data from Chengcan Xiao, reproduced with permission.

Table 3.3. Peak position and area of fitted peaks. Data from Chengcan Xiao, reproduced with permission.

O 1s	Lattice O			Sr-OH			Ti-OH		
	Position	area	% area	position	area	% area	position	area	% area
pristine $SrTiO_3$	529.02	27970.42	74.4	529.92	976.658	2.6	531.12	8657.705	23.0
H_2-annealed $SrTiO_{3-x}$ no polarization	529.57	33513.96	65.5	530.57	8597.11	16.8	532.07	9081.723	17.7
$SrTiO_{3-x}$ after Forward polarization	529.61	32090.13	65.5	530.61	7781.211	15.9	532.01	9088.064	18.6
$SrTiO_{3-x}$ after Reverse polarization	529.64	33836.46	67.2	530.64	7579.349	15.1	532.04	8916.169	17.7

Ti 2p	Ti 2p3/2		Ti 2p1/2	
	position	area	position	area
pristine $SrTiO_3$	457.92	21239.11	463.62	10619.55
H_2-annealed $SrTiO_{3-x}$ no polarization	458.48	25635.24	464.18	12817.62
$SrTiO_{3-x}$ after Forward polarization	458.51	24075.46	464.31	12037.73
$SrTiO_{3-x}$ after Reverse polarization	458.54	24119.27	464.24	12059.64

Sr 3d	Sr 3d5/2		Sr 3d3/2	
	position	area	position	area
pristine $SrTiO_3$	132.42	20708.42	134.22	14281.81
H_2-annealed $SrTiO_{3-x}$ no polarization	133.02	23528.67	134.82	16773
$SrTiO_{3-x}$ after Forward polarization	133.11	23192.43	134.81	15460.07
$SrTiO_{3-x}$ after Reverse polarization	133.14	23058.39	134.84	16302.78

3.6 References

1. Valasek J.; *Physical Review*, **1921**, *17* (4), 475-481.

2. Butler K. T., Frost J. M., Walsh A.; *Energy and Environmental Science*, **2015**, *8*, 838-848.

3. Martin L. W., Rappe A. M.; *Nature Reviews Materials*, **2016**, *2*, 16087.

4. Lopez-Varo P., Bertoluzzi L., Bisquert J., Alexe M., Coll M. Huang J., Jimenez-Tejada J. A., Kirchartz T., Nechache R., Rosei F., Yuan Y.; *Physics Reports*, **2016**, *653*, 1-40.

5. Yuan G. L., Wang J.; *Applied Physics Letters*, **2009**, *95* (25), 252904.

6. Giocondi J. L., Rohrer G. S.; *The Journal of Physical Chemistry B*, **2001**, *105* (35), 8275-8277.

7. Burbure N. V., Salvador P. A., Rohrer G. S.; *Chemistry of Materials*, **2010**, *22* (21), 5823-5830.

8. Cui Y., Briscoe J., Dunn S.; *Chemistry of Materials*, **2013**, *25* (21), 4215-4223.

9. Inoue Y., Sato K., Sato K.; *Journal of the Chemical Society, Faraday Transactions 1: Physical Chemistry in Condensed Phases*, **1989**, *85*, 1765-1774.

10. Yang S. Y., Martin L. W., Byrnes S. J., Conry T. E., Basu S. R., Paran D., Reichertz L., Ihlefeld J., Adamo C., Melville A., Chu Y. H., Yang C. H., Musfeldt J. L., Schlom D. G., Ager J. W., Ramesh R.; *Applied Physics Letters*, **2009**, *95* (6), 062909.

11. Yang S. Y., Seidel J., Byrnes S. J., Shafer P., Yang C. H., Rossell M. D., Yu P., Chu Y. H., Scott J. F., Ager J. W., Martin L. W., Ramesh R.; *Nature Nanotechnology*, **2010**, *5* (2), 143-147.

12. Lee D., Baek S. H., Kim T. H., Yoon J. G., Folkman C. M., Eom C. B., Noh T. W.; *Physical Review B*, **2011**, *84* (12), 125305.

13. Ahn C. H., Rabe K. M., Triscone J. M.; *Science*, **2004**, *303* (5657), 488-491.

14. Tsuda K., Tanaka M.; *Acta Crystallographia Section A*, **1995**, *A51*, 7-19.

15. Kim Y., Choi J., Kim J., Moon S., Park B., Yu J., Kwon J., Kim M., Chung J., Noh T., Yoon J.G.; *Applied Physics Letters*, **2010**, *97*, 242907.

16. Choi M., Oba F., Kumagai Y., Tanaka I.; *Advanced Materials*, **2013**, *25* (1), 86-90.

17. Kim Y. S., Kim J., Moon S. J., Choi W. S., Chang Y. J., Yoon J. G., Yu J., Chung J. S., Noh T. W.; *Applied Physics Letters*, **2009**, *94*, 202906.

18. He R., Lin J. L., Liu Q., Liao Z., Shui L., Wang Z. J., Zhong Z., Li R. W.; *ACS Applied Materials & Interfaces*, **2020**, *12* (40), 45602-45610.

19. Klyukin K., Alexandrov V.; *Physical Review B*, **2017**, *95* (3), 035301.

20. Wan T., Qu B., Du H., Lin X., Guan P., Lin Q., Chen N., Tan T. T., Hang T., Chu D.; *Journal of Colloid and Interface Science Volume*, **2017**, *494*, 15, 178-184.

21. Assavachin S., Nail B. A., Goncalves R. V., Mulcahy J. R., Lloyd S. E., Osterloh F. E.; *Materials Advances*, **2020**, *1*, 1382-1389.

22. Das S., Wang B., Cao Y., et al.; *Nature Communication*, **2017**, *8*, 615.

23. Jiang W., Noman M., Lu Y. M., Bain J. A., Salvador P. A., Skowronski M.; *Journal of Applied Physics*, **2011**, *110*, 034509.

24. Martino G. D., Demetriadou A., Li W. et al.; *Nature Electronics*, **2020**, *3*, 687–693.

25. Li Y., Lei Y., Shen B.; *Scientific Reports*, **2015**, *5*, 14576.

26. Zhong W. M., Tang X. G., Liu Q. X., Jiang Y. P., Li W. H., Yue J. L.; *Physica B: Condensed Matter*, **2021**, *615*, 15, 413080.

27. Meyer R., Waser R.; *Journal of the European Ceramic Society*, **2001**, *21*, 10–11, 1743-1747.

28. Dragos N., Irvine J. T. S.; *Chemistry of Materials*, **2011**, *23*, 6, 1607–1617.

29. Mavroides J. G., Kafalas J. A., Kolesar D. F.; *Applied Physics Letter*, **1976**, *28* (5), 241-243.

30. Wild R. L., Rockar E. M., Smith J. C.; *Physical Review B*, **1973**, *8* (8), 3828-3835.

31. Yamada H., Miller G. R.; *Journal of Solid State Chemistry*, **1973**, *6*, 169-177.

32. Khomenko V. M., Langer K., Rager H., Fett A.; *Physics and Chemistry of Minerals*, **1998**, *25* (5), 338-346.

33. Wrighton M. S., Ellis A. B., Wolczanski P. T., Morse D. L., Abrahamson H. B., Ginley D. S.; *Journal of American Chemical Society*, **1976**, *98* (10), 2774-2779.

34. Zhao Z., Goncalves R. V., Barman S. K., Willard E. J., Byle E., Perry R., Wu Z., Huda M. N., Moulé A. J., Osterloh F. E.; *Energy and Environmental Science*, **2019**, *12*, 1385-1395.

35. Ham Y., Hisatomi T., Goto Y., Moriya Y., Sakata Y., Yamakata A., Kubota J., Domen K.; *Journal of Materials Chemistry A*, **2016**, *4*, 3027-3033.

36. Takata T., Jiang J., Sakata Y., Nakabayashi M., Shibata N., Nandal V., Seki K., Hisatomi T., Domen K.; *Nature*, **2020**, *581* (7809), 411-414.

37. Kumar A., Santangelo P. G., Lewis N. S.; *Journal of Physical Chemistry*, **1992**, *96* (2), 834-842.

38. Doughty R. M., Hodges B., Dominguez J., Han R., Zhao Z., Assavachin S., Osterloh F. E.; *The Journal of Physical Chemistry C*, **2020**, *124* (34), 18426-18435.

39. Ferrer S., Somorjai G. A.; *Surface Science*, **1980**, *94* (1), 41-56.

40. Xie K., Umezawa N., Zhang N., Reunchan P., Zhang Y., Ye J.; *Energy and Environmental Science*, **2011**, *4*, 4211-4219.

41. Wang C., Koirala P., Stair P., Marks L.; *Applied Surface Science*, **2017**, *422*, 661-665.

42. Hrabovsky D., Berini B., Fouchet A., Aureau D., Keller N., Etcheberry A., Dumont Y.; *Applied Surface Science*, **2016**, *367*, 307-311.

43. Vasquez R. P.; *Journal of Electron Spectroscopy and Related Phenomena*, **1991**, *56*, 217-240.

44. Chen H., Zhang F., Zhang W., Du Y.; *Applied Physics Letter*, **2018**, *112*, 013901.

Chapter 4 – Surface Dipoles at the 111, 110, and 100 Facets of Strontium Titanate ($SrTiO_3$) Single Crystals Control Charge Separation During Photoelectrochemical Water Oxidation

4.1 Introduction

Photoelectrochemical (PEC) overall water splitting is a thermodynamically uphill process involving a 4-electron redox reaction which allows for simultaneous H^+ reduction and H_2O oxidation. [1] In general, the process involves photon absorption, charge generation, separation, transport, and surface redox reactions. [2-5] Efficient carrier separation is the basis of high efficiency solar energy conversion. [6-9] For photocatalysts involved the importance of crystal facets for carrier separation has been recognized recently. [7] Because facets differ in terms of atomic and electronic structure, [10,11] they have different energetics for electron/hole accumulation. [6,7] This creates a built-in electric field which promotes carrier separation. [7, 12-14] Facet engineering, therefore, can improve the efficiency of a photocatalyst. For example, Wolfram Jaegermann et al. reported that [100] and [110] facets in titanium dioxide single crystals showed differences in their Fermi level due to the differences in their work function. [15] The Fermi level of the [100] facet is 150-450 meV lower in energy than the [110] facet. This is due to the higher concentration of oxygen vacancies on the [110] facet.

Strontium titanate ($SrTiO_3$) is the well-known overall water splitting photocatalyst, and the importance of facets on charge separation is a topic of great interest. [16] Faceted $SrTiO_3$ photocatalysts can be synthesized by a flux method. [17] $SrTiO_3$ crystals of cubic morphology and terminated by low index [100] facets are obtained in LiCl flux. This facet is promoted by the high solubility of $SrTiO_3$ in this flux. On the other hand, $SrCl_2$ or NaCl do not dissolve $SrTiO_3$ as well, resulting in truncated cubes with [110] edges, while KCl flux yields a triangular pyramid-like morphology with high energy [120] and [121] facets. In a study by Can Li

et al., [18] the overall water splitting activity of isotropic facet terminated (6-facet $SrTiO_3$) and anisotropic facet terminated (18-facet $SrTiO_3$) was compared. Selective deposition of Pt (for the hydrogen evolution reaction, HER) and Co_3O_4 (for the oxygen evolution reaction, OER) cocatalysts on the [100] and [110] facets respectively increased photocatalytic activity by a factor of ten over SrTiO3 with randomly arranged Pt and Co_3O_4 cocatalysts. This improvement was due to enhanced charge separation achieved by spatial separation of the reduction and oxidation sites on their appropriate facets. In 2020, the Domen group achieved near 100% quantum efficiency for overall water splitting in $SrTiO_3$:Al through facet engineering. [19] Rh/Cr_2O_3 cocatalysts preferentially deposited on the electron collecting [100] facet, while the CoOOH cocatalyst deposited preferentially on the [110] facets, although there were not well defined. The preferential photodeposition was attributed to the charge selectivity of the facets.

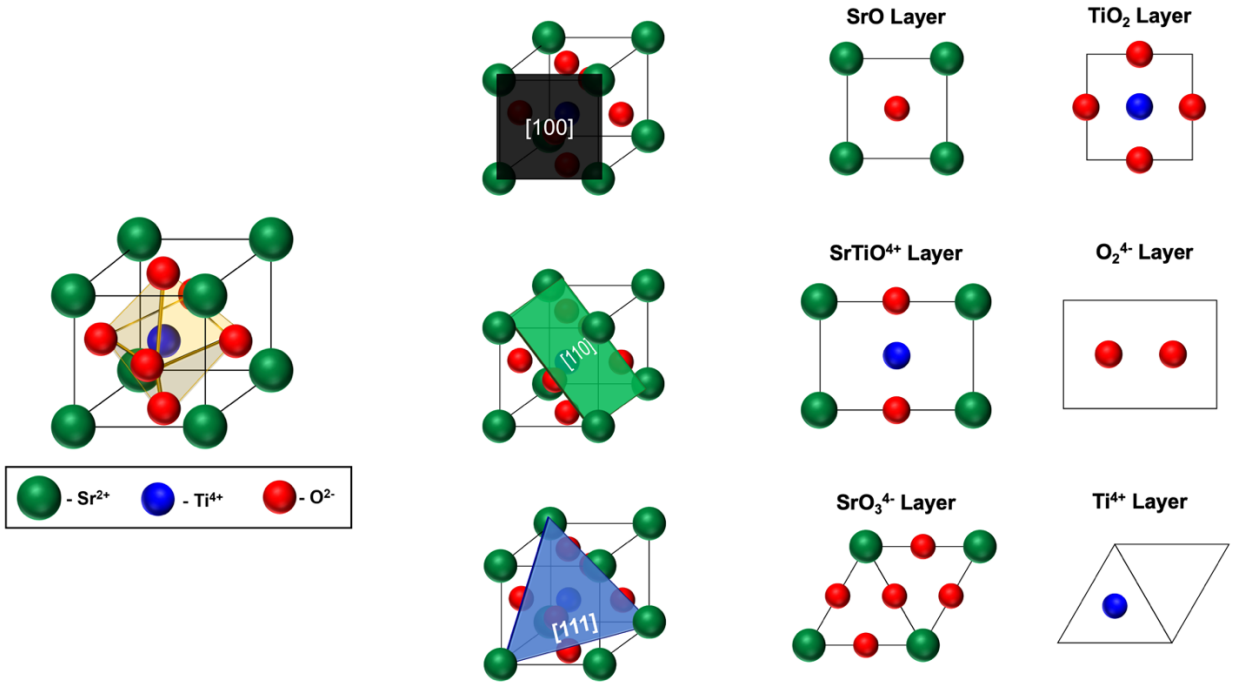

Figure 4.1. Exposed facet pictures of $SrTiO_3$ unit cell [100] – Top Row, [110] – Middle Row, [111] – Bottom Row with two possible termination layers. Reprinted from Biswas A., Rossen P. B., Yang C.-H.,

Siemons W., Jung M.-H., Yang I. K., Ramesh R., and Jeong Y. H.; *Applied Physics Letters*, **2011**, *98*, 051904 with the permission of AIP Publishing. [20]

Exposed facets of $SrTiO_3$ contain distinct atomic environments (**Figure 4.1**), which result in variations in and hydration and water dissociation. [21] Holmström et al. [22] performed density functional theory (DFT) calculations and observed differences in surface hydroxylation rate between planar Sr-O and TiO_2-terminated [001] surfaces of $SrTiO_3$. This was attributed to the varying basicity and differences in the ionicity between the Sr-O and TiO_2 terminations. This leads to different adsorption geometries for water molecules, degrees of water dissociation, and proton transfer rates.

The objective of this present study is to observe the influence of different exposed facets [100, 110, 111] of hydrogen annealed strontium titanate ($SrTiO_{3-x}$) single crystals on photoelectrochemical (PEC) water oxidation. This complements the photodeposition and theoretical studies mentioned above, [22, 23] and would provide more direct evidence for the role of the facets on charge separation. [17-19] In this study, we utilize commercially available $SrTiO_3$ single crystals with three exposed facets. [100, 110, 111] Hydrogen annealing is performed to improve the conductivity of the $SrTiO_3$ single crystals. [24-27] By working with single crystals, we control, isolate, and stabilize the high-energy facets [110 and 111] for comparison with the lower-energy facet [100]. Our findings on the facet-dependent photoelectrochemistry of the crystals are described below.

4.2 Results and Discussion

Strontium titanate ($SrTiO_3$) single crystals with [100, 110, 111] orientations (MSE Supplies ®, 10 x 10 x 0.50 mm) were annealed at 1,100°C in forming gas (10% H_2 / 90% Argon) for 6 hours. SEM images post H_2 annealing for the three facets of H_2 annealed $SrTiO_{3-x}$ single crystals are shown in **Figure 4.2a-c**. The images showed a smooth uniform surface with no observable particle formation or impurities observed. XRD pattern in **Figure 4.2d** confirm phase purity of the crystals and the correct crystal orientations after H_2 annealing. This suggests that the H_2 annealing process does not alter the surface morphology or the exposed facets of the single crystals.

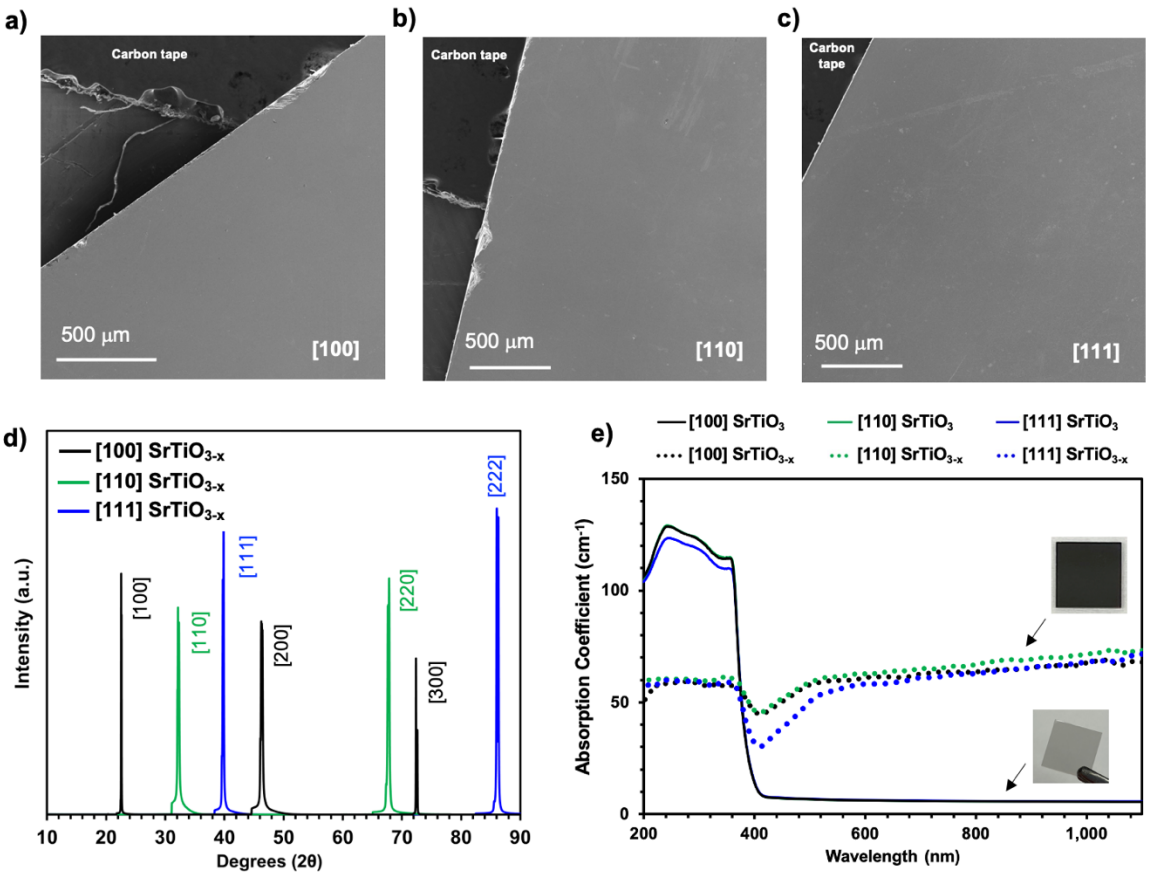

Figure 4.2. H_2-annealed $SrTiO_{3-x}$ with different crystal orientations. a-c) SEM images, d) XRD patterns, e) UV-Vis spectra of as-received and H_2-annealed samples. Inset shows photos of pristine and black films

after H_2 annealing. Additional images of $SrTiO_{3-x}$ single crystals post H_2 annealing is available in **Appendix 4.9**.

Optical absorption spectra of the pristine and H_2-annealed $SrTiO_{3-x}$ single crystals are shown in **Figure 4.2e**. Optical bandgaps were observed at 3.2 eV (390 nm) agreeing with the literature value of 3.2 eV. [28] After hydrogen annealing, $SrTiO_{3-x}$ crystals turn black (**Appendix 4.9**) and develop a secondary absorption feature in the visible light region that extends into the infrared (IR) region. This absorption results from Ti^{3+} and oxygen vacancies in the material and is associated with the excitation of free electrons in the conduction band. [29]

X-ray photoelectron spectroscopy (XPS) was conducted to study the surface composition of [100], [110], and [111] oriented $SrTiO_3$ crystals pre- and post-H_2 annealing. Binding energies for all elements are summarized in **Table 4.2**. Survey scans (**Appendix 4.10**) confirm the presence of Sr, Ti, and O peaks before and after H_2 annealing. For the pristine $SrTiO_3$ single crystals, the Sr $3d_{5/2}$ peak is at 132.4 - 132.7 eV, the Ti $2p_{3/2}$ peak at 457.8 - 458.0 eV, and the O 1s peak at 528.9 - 529.1 eV. This matches the results from previous reports. [30-34] For the [100], [110], and [111] facets of $SrTiO_{3-x}$ single crystals, Ti 2p peaks are shifted to higher binding energy by 0.41 eV, 0.38 eV, and 0.5 eV respectively (**Figure 4.3a-c**). This indicates that H_2 annealing shifts the Fermi level towards the conduction band of $SrTiO_3$ making it more n-type. Two additional shoulder peaks at lower energy relative to the major peaks of Ti $2p_{1/2}$ and Ti $2p_{3/2}$ were observed post H_2-annealing and were attributed to the formed Ti^{3+} species. [35-36] The presence of Ti^{3+} species indicate a significant reduction of the Ti^{4+} population, consistent with the black appearance of the single crystals. Sometimes, Ti^{3+} species are absent from the XPS for reduced $SrTiO_{3-x}$, as a result of air oxidation. [30,34]

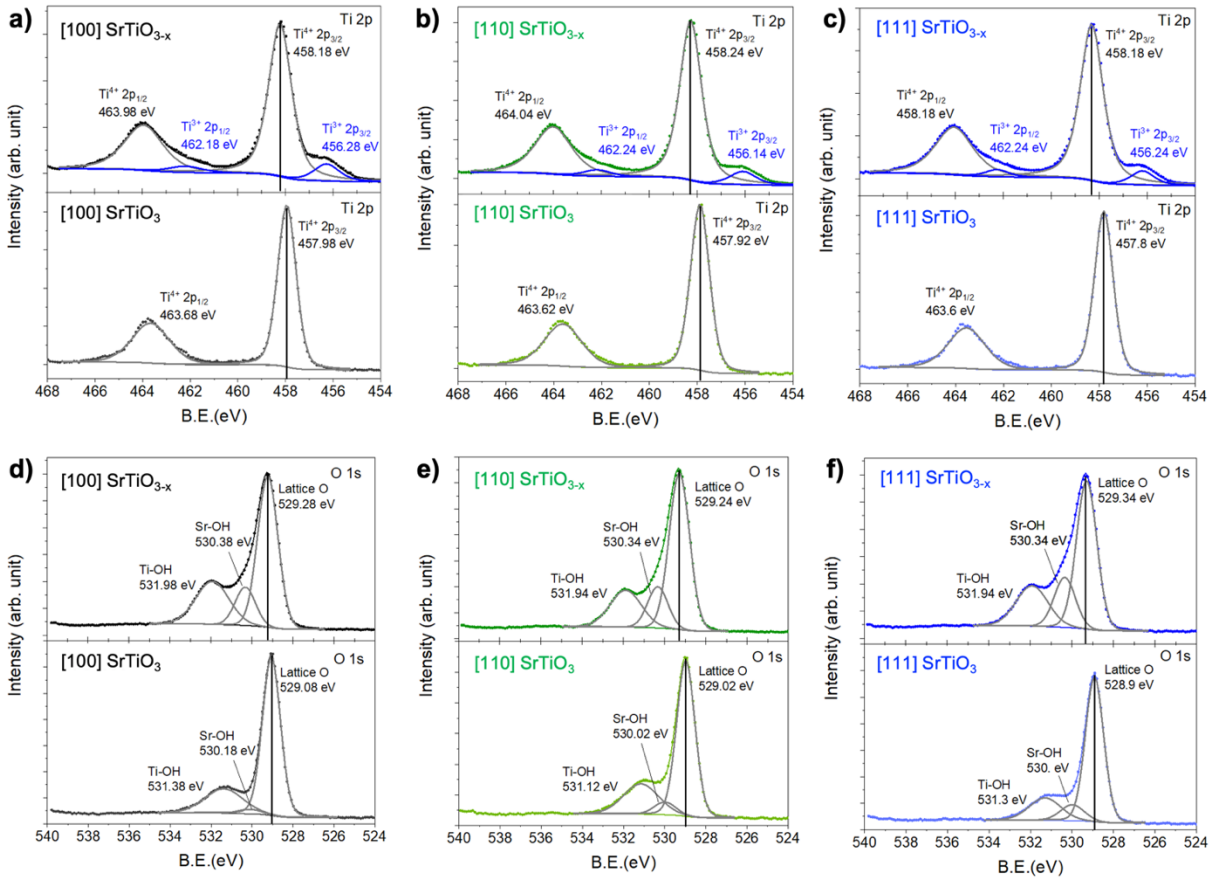

Figure 4.3. Ti 2p peak of a) [100], b) [110], and c) [111] facets of single crystal $SrTiO_3$ and O 1s peak of d) [100], e) [110], and f) [111] facets of single crystal $SrTiO_3$ before and after H_2 annealing. Top section is for H_2 annealed samples. Bottom section is for pristine samples. The position of each fitted peak is marked with a vertical black line to show the peak shift resulted from H_2 annealing. Data provided by Chengcan Xiao with permission.

High resolution O 1s spectra are shown in **Figure 4.3d-f**. After H_2 annealing, the O 1s lattice peaks are shifted by 0.2 eV, 0.22 eV, and 0.44 eV for the [100], [110] and [111] facets, respectively. Similar shifts are seen for Ti 2p peaks (**Figure 4.3a-c**). Additionally, a significant increase in the intensities of Ti-OH [32-

[34] and Sr-OH [32] peaks were observed post H_2 annealing. These hydroxyls are direct indications to the formation of oxygen vacancies. Overlapped plot of the O1s spectra for the pristine and H_2-annealed samples are shown in **Appendix 4.11**. Although minor variations are observed, the shape and intensity of the O shoulders from all three facets are similar, indicating no significant differences in the chemical environment of surface oxygen species among the different $SrTiO_{3-x}$ facets. The binding energies for the oxygen peaks are summarized in **Table 4.2**. Sr 3d peaks were shifted by 0.14 eV, 0.27 eV, and 0.30 eV respectively (**Appendix 4.12**) after H_2 annealing. The Sr shoulder peaks (0.7 eV higher than Sr 3d major peak) are assigned to surface Sr ions bonded to hydroxide or peroxide groups. [37-41] These results confirmed that H_2 annealing reduces Ti^{4+} to Ti^{3+} and promotes the formation of oxygen vacancies at all facets.

The photoelectrochemical (PEC) activity of the H_2 annealed single crystals was measured in aqueous 0.50 M Na_2SO_4 with or without added 20 % methanol under UV light illumination (60 mW cm^{-2}). The measurement configuration is shown in **Appendix 4.13a** and the data is shown in **Figure 4.4**. For the as-purchased single crystals, no photocurrent under UV light illumination can be obtained due to the insulating property of the material (**Appendix 4.15**). For the H_2 annealed crystals, an anodic photocurrent is observed that can be attributed to water oxidation to oxygen, as evidenced by visible gas evolution (**Appendix 4.16**). Also, the current is stable over the course of several minutes, ruling out photocorrosion as the course of the current. As **Figure 4.4** shows, among the three samples, [111] $SrTiO_{3-x}$ yields the highest anodic photocurrent of 1.30 mA cm^{-2} at 1.23 V RHE, [110] $SrTiO_{3-x}$ yields intermediate (0.81 mA cm^{-2}) and [100] $SrTiO_{3-x}$ yields the smallest photocurrent (0.34 mA cm^{-2}). The anodic photo-onset (E_{on}) was found to be the same for [111] and [110] $SrTiO_{3-x}$ at -0.287 V vs RHE while [100] $SrTiO_{3-x}$ exhibits the least reducing onset at -0.190 V vs RHE. This corresponds to a photovoltage of $V_{ph} = E^0 - E_{on}$ of 1.52 V for both [111] and [110] $SrTiO_{3-x}$ and 1.42 V for [100] $SrTiO_{3-x}$ electrodes (using E^0 of water oxidation at 1.23 V RHE).

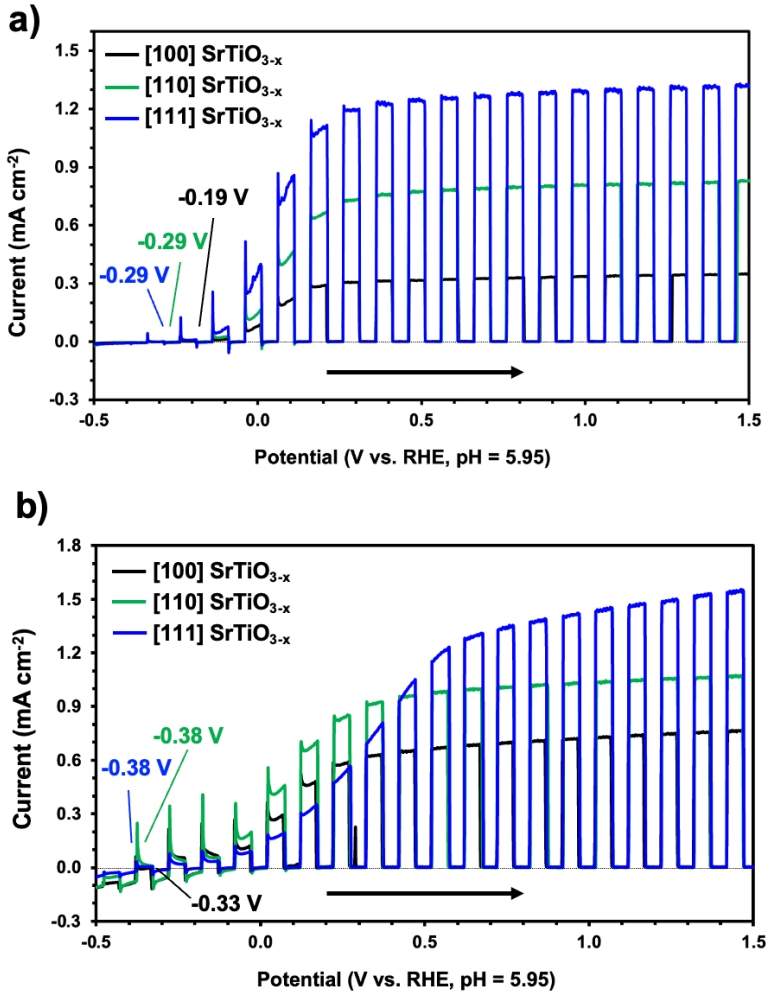

Figure 4.4. a) PEC scans of H_2 annealed strontium titanate single crystals under UV illumination (60 mW cm^{-2}) from Xe Lamp in a) 0.50 M Na_2SO_4 non-degassed aqueous solution, and b) 0.50 M Na_2SO_4 non-degassed aqueous solution with added 20% (volume) methanol (pH = 5.95). Single crystals were coated with InGa eutectic to establish an Ohmic contact. The scan direction is from negative to positive potential as indicated by the horizontal arrow. The active area of electrode in contact with solution is 0.50 cm^2. A zoomed-in photo onset is available in **Appendix 4.14**.

This shows that the water oxidation photocurrent depends on the exposed crystal facets. These results were

reproducible in three separate crystal samples, as shown in **Appendix 4.17** and **Table 4.3**. The mean photocurrents for [100] $SrTiO_{3-x}$, [110] $SrTiO_{3-x}$, and [111] $SrTiO_{3-x}$ are 0.34, 0.82, and 1.36 mA cm^{-2} (1.23 V RHE) respectively, with the highest standard deviation of 0.08 mA cm^{-2} (5.89 %) in the [111] $SrTiO_{3-x}$ sample. Mean photocurrent onsets for three separate crystal samples were -0.294 V RHE for [111] $SrTiO_{3-x}$, -0.286 V RHE [110] $SrTiO_{3-x}$, and -0.172 V RHE for [100] $SrTiO_{3-x}$, as shown in **Appendix 4.17** and **Table 4.3**.

To verify whether the water oxidation kinetics were the cause of facet-dependent activity, the fast hole acceptor 20 % (vol.) methanol was added to 0.50 M Na_2SO_4 and the PEC scans were repeated (**Figure 4.4b**). Anodic photocurrents were increased for all samples. [111] $SrTiO_{3-x}$ showed the highest activity of 1.48 mA cm^{-2} (1.23 V RHE), followed by [110] $SrTiO_{3-x}$ and [100] $SrTiO_{3-x}$ at 1.06 mA cm^{-2} and 0.74 mA cm^{-2} respectively. Anodic photocurrent onsets were also shifted to -0.38 V RHE for [111] and [110] $SrTiO_{3-x}$ crystals and to roughly -0.33 V RHE for the [100] $SrTiO_{3-x}$ crystal. A small reductive dark current was observed for all three crystals, which is possibly from the presence of residual oxygen. As the same trend in photocurrents and photoonsets is observed during methanol oxidation, oxidation kinetics can be ruled out as the cause of activity differences between facets. Also, as shown in **Appendix 4.18**, the $SrTiO_{3-x}$ backside has negligible influence on the PEC activity. Because the $SrTiO_{3-x}$ crystals are thicker than the light penetration depth (δ_P) = 1 / α of $SrTiO_{3-x}$ = 0.16 mm at 348 nm ($\alpha_{348\ nm}$ = 61.8 cm^{-1}), less than 0.1 % of the UV light intensity can excite the backside. This explains why the PEC contribution from the back side can be neglected.

To independently assess the photovoltage generating ability of the three crystals, Vibrating Kelvin Probe Surface Photovoltage Spectra (VK-SPS) were recorded for all samples. VKP-SPS measures the contact

potential difference (CPD) change of a thin film with a commercially available vibrating Kelvin probe (Besocke Delta Phi). [42, 43] Illumination through the semi-transparent probe disturbs the distribution of the charge carriers in the sample and produces a surface photovoltage signal SPV = CPD_{light} - CPD_{dark}. The sign and size of the SPV signal provides information about the majority carrier type and the photovoltage. [44-46] To mimic the conditions during PEC, $SrTiO_{3-x}$ crystals were coated with 8 µL of 0.50 M Na_2SO_4, covered with a microscopy cover slip glass, and placed underneath the Kelvin probe, as shown in **Appendix 4.19**.

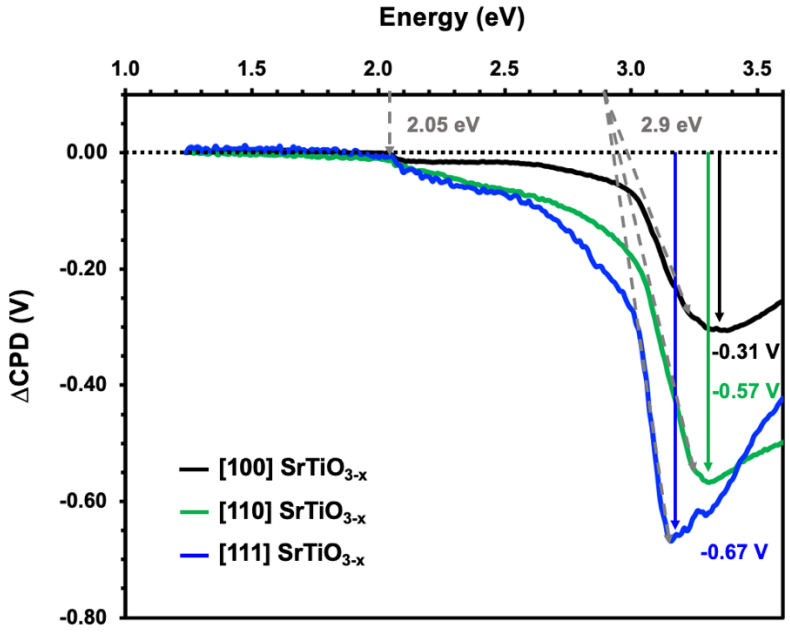

Figure 4.5. Surface photovoltage spectra of $SrTiO_{3-x}$ single crystals exposed to 8 µL 0.50 M Na_2SO_4 aqueous solution under H_2O-saturated oxygen gas flow. Illumination was provided from a 300 W Xe light source filtered through a monochromator. The light intensity at 3.3 eV is 1.91 mW cm^{-2}. The scan direction was from low to high energy. Data provided by Kathleen Becker with permission.

The resulting SPS spectra are shown in **Figure 4.5**. The major photovoltage signal onset occurs at 2.9 eV,

slightly below the optical band gap of the material (3.2 eV). Additionally, a sub band gap signal is observed at 2.05 eV, which is attributed to the excitation of Ti^{3+} defect states, as described before. [47] At 3.2 - 3.4 eV the maximum ΔCPD varies from -0.67 V for [111] $SrTiO_{3-x}$ to -0.57 V for [110] $SrTiO_{3-x}$ and -0.31 V for [100] $SrTiO_{3-x}$. These surface photovoltage signals are smaller than the photovoltage values from PEC due to the lower light intensity used. Nevertheless, the trend correlates well with the photocurrent and photovoltage data from the PEC measurements in **Figure 4.4**. This confirms that the facets differ in their ability to generate a photovoltage, and that this is the reason for the observed photocurrent trends seen in **Figure 4.4**.

To better characterize the band bending at the three $SrTiO_{3-x}$ liquid interfaces, Mott-Schottky measurements (MS) were conducted. Three frequencies at 100, 125, and 150 Hz were selected to measure the flatband potential. The flatband potential is defined as the potential required to remove the depletion layer at the semiconductor-electrolyte junction. To ensure formation of a depletion layer, the fast $K_{3/4}[Fe(CN)_6]$ redox couple (50 mM each) is added into 0.50 M Na_2SO_4 aqueous solution. The system was purged with nitrogen gas for 30 minutes and throughout the experiment to remove the presence of oxygen. Electric contact to the single crystals was established with InGa eutectic to ensure an Ohmic contact. As can be seen in **Figure 4.6**, MS plots are linear for all the frequencies tests. The plots have a positive slope consistent with the formation of an electron depletion region. From the MS slope, the free electron density, N_D, can be calculated using the junction area of 1.0 cm^2 (combined from the front and back side) and a dielectric constant ε of 300. [48] Calculation details are given in **Table 4.4** and the caption.

At 100 Hz, calculated N_D values were 1.23 x 10^{20}, 4.88 x 10^{18}, and 1.78 x 10^{19} cm^{-3} for [111], [110], and [100] $SrTiO_{3-x}$ respectively, i.e. N_D [111] > N_D [100] > N_D [110]. All MS calculations presented in this text

are based on the data obtained at a frequency of 100 Hz, as it yields intermediate values between the three measurement frequencies. However, the relative trend remains consistent across all frequencies (**Table 4.4**). The observed difference in free electron density is difficult to explain considering that annealing conditions were identical. It may be attributed to differences in ion migration for the three crystal directions.

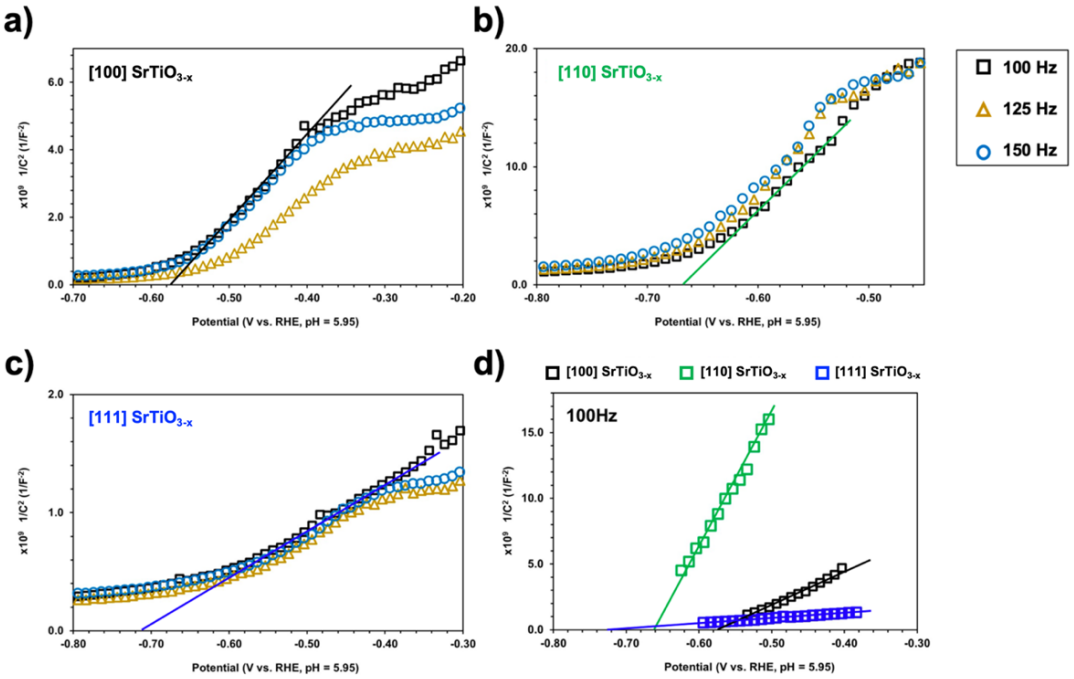

Figure 4.6. Mott Schottky plots at 100, 125, and 150 Hz in 0.50 M Na_2SO_4 aqueous solution (pH = 5.95) with 50 mM equimolar $K_{3/4}[Fe(CN)_6]$ under constant nitrogen purging without illumination is shown for a) [100] $SrTiO_{3-x}$, b) [110] $SrTiO_{3-x}$, c) [111] $SrTiO_{3-x}$ -111$SrTiO_{3-x}$ crystals. The crystal back contact is coated with InGa eutectic, as shown in **Appendix 4.13b**. d) The three facets at 100Hz are plotted for comparison to highlight the differences in slope and x-intercept. Detailed values and calculations are available in **Table 4.4.**

The x-intercept of the Mott Schottky (MS) plot reveals the flat band potential (E_{FB}) where [100] $SrTiO_{3-x}$ has the least reducing potential (-0.60 V vs RHE) followed by [110] $SrTiO_{3-x}$ (-0.69 V) and [111] $SrTiO_{3-x}$

(-0.75 V). This trend aligns with the relative photovoltage values $V_{Ph} = E^0 - E_{on}$ from the PEC data in **Figure 4.4**. A summary of all PEC, MS, and SPS values is shown in **Table 4.1**.

Table 4.1. Summary of mean values and standard deviations for photocurrent, flatband potentials, built-in potentials, surface photovoltage, and conduction band edges for three facets of $SrTiO_{3-x}$. All values based on MS calculations are based on data obtained at 100 Hz.

	[100] $SrTiO_{3-x}$	[110] $SrTiO_{3-x}$	[111] $SrTiO_{3-x}$
Photocurrent at 1.23 V RHE / mA cm^{-2}	0.34 ± 0.01	0.82 ± 0.00	1.36 ± 0.08
Photovoltage V_{Ph} (from PEC) / V	1.40 ± 0.03	1.52 ± 0.05	1.52 ± 0.01
Flatband potential E_{FB} (from MS) /V RHE	-0.596	-0.692	-0.751
Built-in potential V_{bi} (from MS) /V	1.83	1.92	1.98
Surface photovoltage SPV / V	0.31	0.57	0.67
Conduction Band Edge E_{CB}/ V vs RHE at pH = 5.95	-0.69	-0.82	-0.80

The connection between the junction properties and the PEC behavior of the crystals can be explained with the energy diagram in **Figure 4.7**. In contact with O_2/H_2O, the Fermi level of the $SrTiO_{3-x}$ electrodes equalizes with the standard reduction potential of the O_2/H_2O couple (E^0 = 1.23 V RHE), as shown in **Figure 4.7a**. Under these conditions, the potential drop in the space charge region is defined by the built-in potential $V_{bi} = E_{FB} - E^0 (O_2/H_2O)$. Using the E_{FB} values from the MS analysis, it can be seen that V_{bi}=

1.83 V for [100] $SrTiO_{3-x}$, 1.92 V for [110] $SrTiO_{3-x}$, and 1.98 V for [111] $SrTiO_{3-x}$ i.e., the band bending decreases in the series [111] > [110] > [100]. This agrees with the relative photovoltage and photocurrent trends summarized in **Table 4.1**. This proves that the built-in potential (band bending) controls the efficiency of charge separation and photoelectrochemical water oxidation properties with $SrTiO_{3-x}$. The energy diagrams in **Figure 4.7** also give the depletion layer thickness for the series [111] $SrTiO_{3-x}$ (23.14 nm) < [100] $SrTiO_{3-x}$ (58.39 nm) < [110] $SrTiO_{3-x}$ (114.29 nm). This order is very different from the PEC performance trend in **Figure 4.4**. This shows that the depletion layer thickness does not control the photovoltage or the photocurrent in these samples.

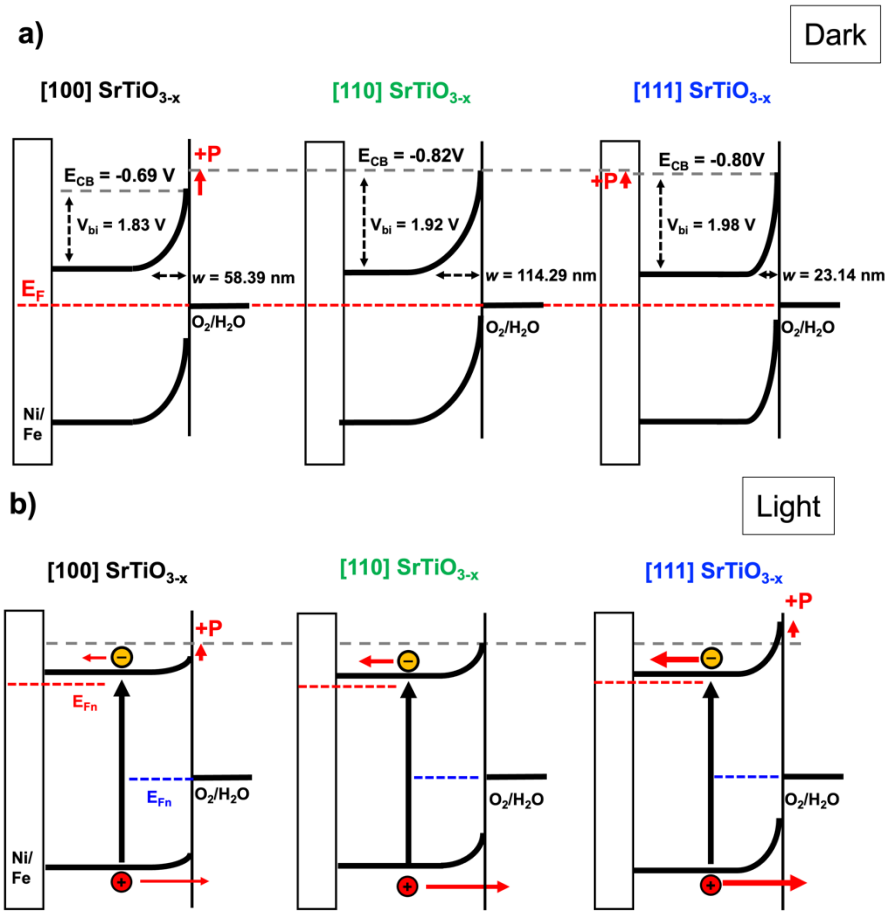

Figure 4.7. Energy diagram for [100] $SrTiO_{3-x}$ (left), [110] $SrTiO_{3-x}$ (middle), [111] $SrTiO_{3-x}$ (right) with flatband potentials E_{FB} obtained from Mott Schottky plot at 100 Hz. a) Upward band bending in the dark due to E_{FB} equilibrating to the O_2/H_2O potential E^0 = 1.23 V RHE. b) Charge separation under illumination.

E_{CB} positions were obtained from the data in **Appendix 4.20**, using $E_{CB} = E_{FB} \times \ln (N_D / N_{CB})$ where the density of states in the conduction band, $N_{CB} = 8.00 \times 10^{20}$ cm^{-3} (Wang et al). [49] The detailed calculation is shown in **Table 4.4**.

Interestingly, when the experimental N_D concentrations are taken into consideration for calculating the conduction band edges E_{CB} for the three crystals, it becomes apparent that [110] $SrTiO_{3-x}$ (-0.82 V) has the most reducing conduction band edge, followed by [111] $SrTiO_{3-x}$ (-0.80 V) and [100] $SrTiO_{3-x}$ (-0.69 V). This means that if donor densities were equal, the built-in potential would decrease in that order. This agrees well with the findings by Domen et al. for [110] and [100] terminated $SrTiO_{3-x}$ cubes, where holes were found to preferentially accumulate at the [110] facet and electrons at the [100] facet. [18,19] The trends of electron density, conduction band edge position and photocurrent are also graphically represented in **Figure 4.8**.

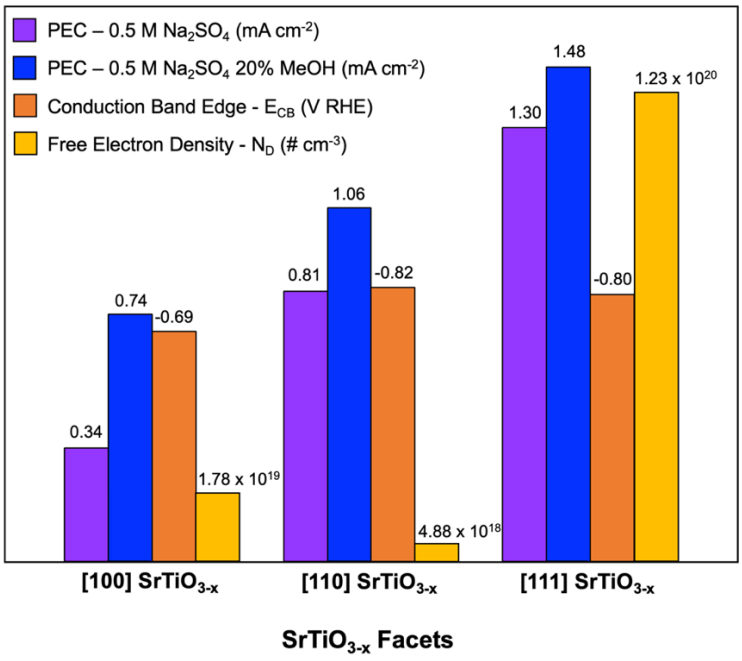

Figure 4.8. Summary of PEC performance in 0.50 M Na_2SO_4 with or without 20 % methanol under UV light illumination (60 mW cm^{-2}) at 1.23 V RHE, of free electron density, N_D, and conduction band edge,

E_{CB}, for [100, 110, 111] $SrTiO_{3-x}$ single crystals. N_D and E_{CB} were calculated from the Mott Schottky slope at 100 Hz (for values see **Table 4.4**).

High water oxidation photocurrents require a *combination* of a reducing E_{CB} value *and* a high electron density to ensure a large built-in potential and fast electron transport. This is the case for the [111] $SrTiO_{3-x}$ crystal, but not for the [110] $SrTiO_{3-x}$ crystal. The [100] $SrTiO_{3-x}$ crystal has the lowest water oxidation performance because it has *both* and oxidizing E_{CB} value *and* the relatively low electron density.

The impact of a high free electron concentration on charge transport can also be observed in the electrochemical impedance (EIS) measurements in **Appendix 4.21**. In the dark, the [111] $SrTiO_{3-x}$ phase has the highest conductivity, followed by the [100] $SrTiO_{3-x}$ phase and the [110] $SrTiO_{3-x}$ phase. This mimics the order of relative N_D values in the series. The corresponding Nyquist plot is shown in **Appendix 4.22**. Based on the diameter of the real versus imaginary impedance curve, the [110] $SrTiO_{3-x}$ crystal has the highest resistivity, followed by [100] $SrTiO_{3-x}$ and [111] $SrTiO_{3-x}$. Overall, the band bending model derived from the Mott-Schottky data confirms that the different flatband potentials (surface Fermi levels) of the facets are the reason for the observed difference in water oxidation properties of $SrTiO_{3-x}$, as manifested in the PEC and SPV data. This provides a rationale for the charge separation mechanism in $SrTiO_3$ photocatalysts. Planned DFT calculations will be aimed at a better understanding of the junction properties in terms of the surface structure.

4.3 Conclusion

In conclusion, hydrogen annealing of strontium titanate single crystals with [100, 110, 111] orientations at 1,100°C yields increases the free electron density of $SrTiO_{3-x}$ and yields crystals suitable for photoelectrochemical measurements. The PEC activity under UV light illumination exhibits significant variations among the different facets, with [111] $SrTiO_{3-x}$ demonstrating the highest water oxidation photocurrent and photovoltage followed by [110] $SrTiO_{3-x}$ and with [100] $SrTiO_{3-x}$ showing the lowest values. Photovoltage values increase from 1.42 V for [100] $SrTiO_{3-x}$ to 1.52 V for [111] and [110] $SrTiO_{3-x}$, in good agreement with the trend in surface photovoltage values (0.31 V, 0.57 V, and 0.67 V for [100], [110], and [111] $SrTiO_{3-x}$ respectively). The reactivity trend can be attributed to differences in the band bending at the different facets, with V_{bi} of 1.83 V for [100] $SrTiO_{3-x}$, 1.92 V for [110] $SrTiO_{3-x}$, and 1.98 V for [111] $SrTiO_{3-x}$. The variable degrees of band bending are a result of the changing surface Fermi levels (flatband potentials) among the three facets, with [100] $SrTiO_{3-x}$ exhibiting the smallest E_{FB} (-0.60 V RHE), followed by [110] $SrTiO_{3-x}$, and [111] $SrTiO_{3-x}$ (-0.69 and -0.75 V RHE). Considering the free electron densities, conduction band edge, E_{CB}, can be calculated for the three crystals. Here [100] $SrTiO_{3-x}$ has the most oxidizing band position (-0.69 V) while [110] $SrTiO_{3-x}$ and [111] $SrTiO_{3-x}$ have similar values (-0.82 V and -0.80 V respectively). That means that at equal donor density, the [110] $SrTiO_{3-x}$ surface would be expected to form the best junction with the O_2/H_2O redox couple, followed by [111] $SrTiO_{3-x}$, and [100] $SrTiO_{3-x}$. This confirms earlier photolabeling results by the Domen group in Japan, which speculated the [110] facets of $SrTiO_3$ to be most suitable for hole accumulation and the [100] facets of $SrTiO_3$ most suitable for electron accumulation. Additionally, we find that the free electron density plays a strong role in controlling the built-in potential and electron transfer. Accordingly, the [111] $SrTiO_{3-x}$ crystal (N_D = 1.23 x 10^{20} cm^{-3}) is the most active for photoelectrochemical water oxidation, followed by [110] $SrTiO_{3-x}$ (4.88 x 10^{18} cm^{-3}) and [100] $SrTiO_{3-x}$ (1.78 x 10^{19}). Overall, these experimental results highlight the importance of crystal facets for photochemical charge separation in photocatalysts. Planned DFT calculations will reveal how the surface structure affects the $SrTiO_3$/liquid junction properties.

4.4 Experimental Section

Water was purified to 18 MΩcm resistivity using a nano-pure system. Double polished single crystals (10 x 10 x 0.50 mm) of strontium titanate with 100, 110, 111-exposed facets were purchased from *MSE Supplies*. Sodium sulfate (99.5%, Sigma Aldrich), potassium hexacyanoferrate (II) trihydrate (98.5%-102.0%, Sigma-Aldrich), potassium ferricyanide (III) (99.9%, Fischer Chemical – Fischer Scientific), gallium-indium eutectic, InGa (≥99.99% trace metal basis, Aldrich Chemistry), and anhydrous methanol (99.9%, Alfa Aesar) were used as received.

Hydrogen Reduced Strontium Titanate Annealing – $SrTiO_{3-x}$

As-purchased $SrTiO_3$ crystals were annealed in a tube furnace by placing them into a ceramic boat inside of a quartz tube, and by exposing them to 10% H_2: 90% argon (0.1 L min^{-1} : 0.9 L min^{-1}) gas flow. Then temperature was increased to 1,100ºC at a rate of 50ºC min^{-1} temperature was kept at 1,100ºC for 6 hours. After that the crystals were cooled to room temperature rapidly by opening the furnace while 10% H_2: 90% Argon continued to flow through the quartz tube. Small holes were drilled into the ceramic crucible promote gas flow. The obtained $SrTiO_{3-x}$ crystal had a shiny black appearance (**Appendix 4.9**).

Optical Absorption

A Thermo Scientific Evolution 220 Spectrometer equipped with an integrating sphere was used to measure transmittance from 200 – 1,100 nm with 2 nm increment. Transmittance was converted to absorbance where: Absorbance = 2 – log (%Transmittance). Optical absorption coefficients, α (cm^{-1}), were calculated as follows equation: $\alpha = 2.303 \times A/d$ where A is the absorbance and d is the thickness in cm. In this case, the thickness is 0.05 cm.

X-ray Photoelectron Spectroscopy

XPS measurements were conducted by Chengcan Xiao with a Supra XPS spectrometer using an Al Kα source that generate x-ray at 1,487 eV and using an ultra-high vacuum (UHV) analytical chamber with a pressure of 10^{-7} mbar. The spectra were electrostatically corrected based on the position of C 1s (284.6 eV). $SrTiO_3$ single crystal pristine as bought or after H_2-annealed were surveyed for O 1s, Ti 2p, Sr 3d, and survey spectrum scan. Baseline simulation of the core-level spectrum was done using the Shirley method. The area ratio between the subpeaks in each doublet was set as ratio between 2j + 1, where j is the total angular momentum quantum number. The FWHM of the subpeaks in each doublet was set equal (except for Ti 2p).

Photoelectrochemical Measurements

Electrochemical measurements were conducted using a Gamry Reference 600 Potentiostat connected to a three-electrode system consisting of a platinum counter electrode and a calomel reference electrode (3.5 M KCl). The working electrode consists of a $SrTiO_{3-x}$ single crystal mounted on a stainless steel alligator clip via InGa eutectic to establish an ohmic contact (**Appendix 4.13a**). Chopped light linear sweep voltammetry was accomplished in 0.50 M Na_2SO_4 aqueous electrolyte solution (pH = 5.95) in a quartz three-neck flask. UV-light illumination was from a 300 W Xe lamp source at an intensity of 60 mW cm^{-2}, as measured with GaAsP photodetector, in the 250-680 nm window. The system was not degassed and contains ambient amounts of air. The electrode area in contact with solution is 1.0 cm^2 (0.50 cm^2 from the front side and 0.50 cm^2 from the back side). Illumination occurs on the front side and the active area of the electrode for photocurrent calculation is 0.50 cm^2. The chopped light scan alternates between light on and light off at a 5-second interval with scan rate of 10 mV/s and scan step of 1 mV. The applied potential was adjusted from

V vs. SCE to V vs. NHE by adding the difference between the half wave potential for the $K_{3/4}[Fe(CN)_6]$ redox couple versus SCE to the redox potential at NHE (0.36 V vs. NHE). Electrical Impedance Spectroscopy (EIS) and Mott-Schottky data were measured in a sealed three-neck flask using a 50 mM equimolar $K_{3/4}[Fe(CN)_6]$ in 0.50 M Na_2SO_4 aqueous solution (as shown in **Appendix 4.13b**). The solution was purged with N_2 for 30 min and bubbled with N_2 throughout the measurement. InGa eutectic was applied at the working electrode between the alligator clip contact to the $SrTiO_{3-x}$ single crystal to establish an Ohmic contact. The single crystal contact area to the electrolyte is 1.0 cm^2, which includes 0.50 cm^2 from the front side and 0.50 cm^2 on the back side. The EIS experiment was conducted at 100 mV rms AC voltage using 10 points/decade, with an initial frequency of 100,000 Hz and final frequency of 0.1 Hz.

Surface Photovoltage Spectroscopy

SPS measurements were accomplished by Kathleen Becker using a vibrating gold mesh Kelvin probe (Delta PHI Besocke) mounted inside a steel chamber, as shown in **Appendix 4.19**. Deionized water (8 µL) was added to the surface of $SrTiO_{3-x}$ single crystal and covered with a glass slide to prevent direct contact between the gold kelvin probe and the liquid solution. O_2 gas was flowed at a rate of 1.0 L min^{-1} through two water baths before reaching the SPS chamber. The O_2 gas was allowed to fill and purge the chamber for 15 minutes prior to the measurement. The $SrTiO_{3-x}$ crystals are illuminated with monochromatic light in the 1.2 – 4.1 eV range using a 300 W Xe lamp filtered by a monochromator (Oriel Cornerstone 130, 1-10 $mW \cdot cm^{-2}$). The lamp intensity was measured using a silicon thermopile detector at 3.3 eV and was found to be 1.91 mW cm^{-2}. Samples were left to equilibrate under 10,000 cm^{-1} illumination from the monochromator until a stable baseline was obtained. Spectrum were acquired from 10,000 – 40,000 cm^{-1} with a measurement interval of 5 seconds and a 100 cm^{-1} illumination increment.

4.5 Appendix

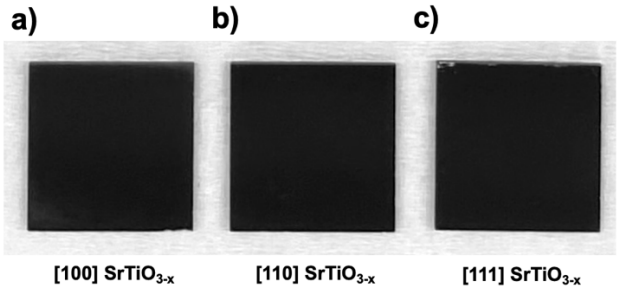

Figure 4.9. Hydrogen-annealed $SrTiO_{3-x}$ single crystals with a) [100], b) [110], and c) [111] facets.

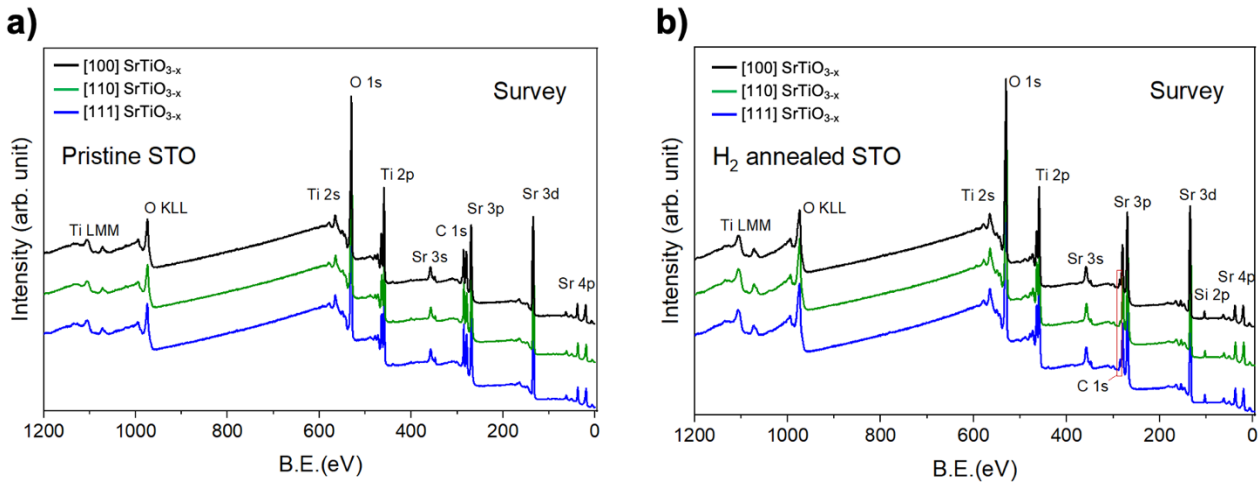

Figure 4.10. Survey scans of [100], [110], and [111] facets of the $SrTiO_3$ single crystals before (a) and after (b) H_2 annealing. A small Si 2p impurity peak at 102 eV is attributed to migration of Si species from the ceramic crucible used for the H_2 annealing at 1100°C. Data provided by Chengcan Xiao with permission.

Table 4.2. XPS summary table for binding energy position and area for pristine and H_2 annealed $SrTiO_3$ single crystals. Data provided by Chengcan Xiao with permission.

O 1s	Lattice O			Sr-OH			Ti-OH			
	Position	Area	% area	Position	Area	% area	Position	Area	% area	
[100] $SrTiO_3$	529.08	28455.580	73.4	530.18	1069.289	2.8	531.38	9233.749	23.8	
[100] $SrTiO_{3-x}$	529.28	35511.050	58.4	530.38	8926.351	14.7	531.98	16413.640	27.0	
[110] $SrTiO_3$	529.02	23034.040	66.3	530.02	742.980	2.1	531.12	10969.540	31.6	
[110] $SrTiO_{3-x}$	529.24	37989.690	61.6	530.34	9944.254	16.1	531.94	13737.490	22.3	
[111] $SrTiO_3$	528.90	25127.190	70.9	530.00	3591.105	10.1	531.3	6719.895	19.0	
[111] $SrTiO_{3-x}$	529.34	34271.930	56.3	530.34	9944.254	19.8	531.94	14569.490	23.9	
Ti 2p	Ti^{4+} $2p_{3/2}$			Ti^{4+} $2p_{1/2}$		Ti^{3+} $2p_{3/2}$			Ti^{3+} $2p_{1/2}$	
	Position	Area	% area	Position	Area	Position	Area	% area	Position	Area
[100] $SrTiO_3$	457.98	18701.270	-	463.68	9350.637	-	-	-	-	-
[100] $SrTiO_{3-}$	458.18	25095.470	89.2	463.98	12547.730	456.28	3053.007	10.8	462.18	1526.504

x										
[110] $SrTiO_3$	457.92	18364.61	-	463.62	9182.303	-	-	-	-	-
[110] $SrTiO_{3-x}$	458.24	29828.030	91.0	464.04	14914.020	456.14	2958.796	9.0	462.24	1479.398
[111] $SrTiO_3$	457.80	18670.750	-	463.60	9335.377	-	-	-	-	-
[111] $SrTiO_{3-x}$	458.34	28265.560	91.7	464.04	14132.780	456.24	2565.564	8.3	462.24	1282.782
Sr 3d	Sr $3d_{5/2}$			Sr $3d_{3/2}$		Surface Sr $3d_{5/2}$			Surface Sr $3d_{3/2}$	
	Position	Area	% area	Position	Area	Position	Area	% area	Position	Area
[100] $SrTiO_3$	132.48	20854.110	-	134.28	13902.81	-	-	-	-	-
[100] $SrTiO_{3-x}$	132.58	21262.600	71.7	134.38	14175.140	133.28	8371.931	28.3	134.98	5581.315
[110] $SrTiO_3$	132.48	19748.21	-	134.12	13165.48	-	-	-	-	-
[110] $SrTiO_{3-x}$	132.74	26611.890	80.9	134.44	17741.350	133.44	6275.025	19.1	135.14	4183.37
[111] $SrTiO_3$	132.40	18647.890	-	134.10	12431.990	-	-	-	-	-
[111]	132.74	22134.040	78.2	134.54	14756.100	133.54	6187.937	21.8	135.24	4125.312

$SrTiO_{3-x}$										

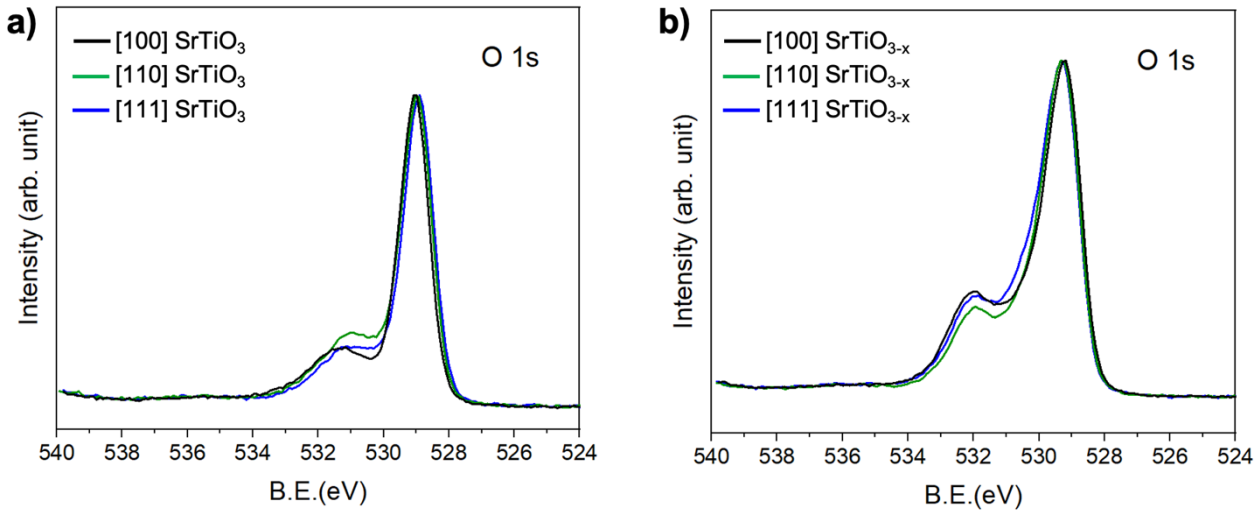

Figure 4.11. Overlapped O1s peak of [100], [110], and [111] facets of $SrTiO_3$ single crystal a) before and b) after H2 annealing. Data provided by Chengcan Xiao with permission.

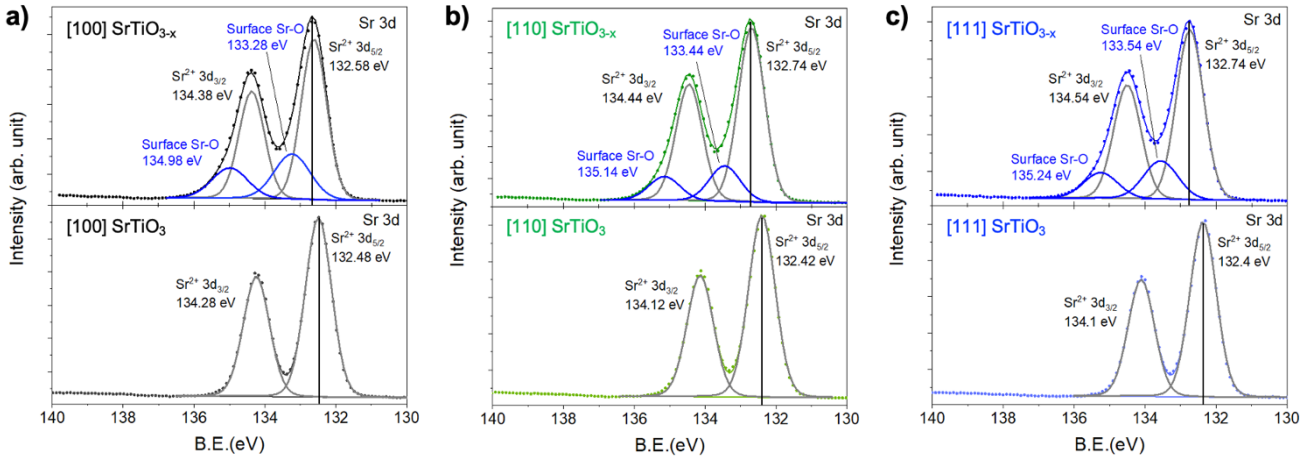

Figure 4.12. Sr 3d peak of a) [100], b) [110], and c) [111] facets of single crystal $SrTiO_3$ before (top) and after H_2 annealing (bottom). Data provided by Chengcan Xiao with permission.

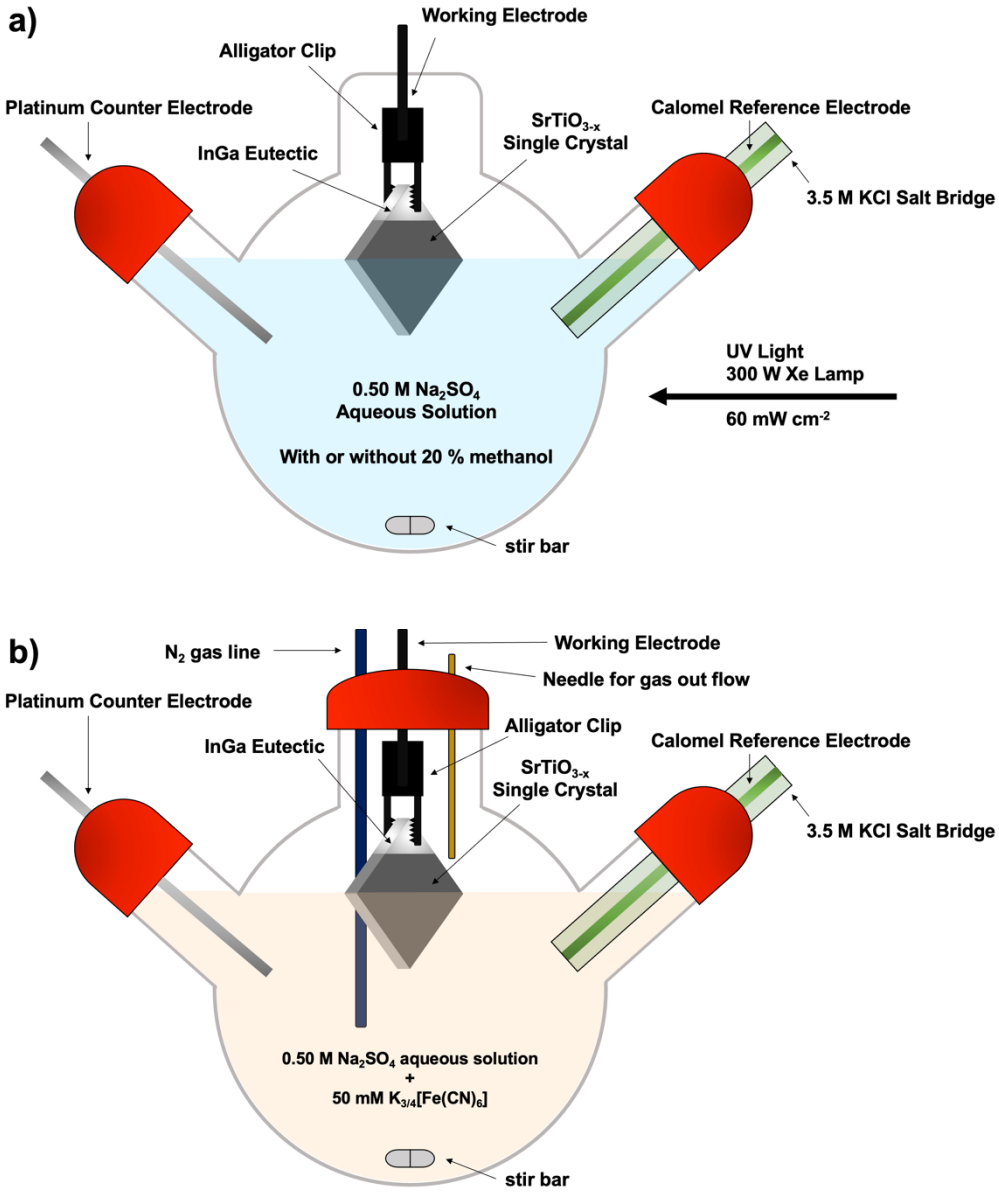

Figure 4.13. Electrochemistry apparatus scheme for a three-electrode system consisting of the working electrode, a calomel reference electrode (3.5 M KCl), and a Pt counter electrode. The working electrode is a $SrTiO_{3-x}$ single crystal with InGa eutectic coating at the back contact to the stainless steel alligator clip. a) Photoelectrochemical (PEC) measurements setup is shown using a 0.50 M Na_2SO_4 aqueous electrolyte solution (pH = 5.95) under constant stirring. UV-light illumination is from a 300W Xe lamp with an

intensity of 60 mW/cm^2 as measured with GaAsP photodetector for 250-680 nm. The system is not degassed and contains ambient amounts of air. Area in contact with solution is 1.0 cm^2, illumination occurs on the front side and the active area of the electrode for photocurrent calculation is 0.50 cm^2. b) Mott-Schottky (MS) and electrochemical impedance spectroscopy (EIS) measurement set up is shown using 50 mL 0.50 M Na_2SO_4 aqueous electrolyte solution (pH = 5.95) with 50 mM equimolar $K_{3/4}[Fe(CN)_6]$ redox couple under constant stirring at 200 rpm. The system is initially purged with N_2 gas for 30 minutes and constantly purged with N_2 gas throughout all measurements. Gas out flow is made possible with the needle where the gas in flow from the nitrogen needle creates a positive pressure inside the flask purging oxygen from the system constantly. No illumination was made throughout the experiment. Active area of the system is 1.0 cm^2 where both sides of the single crystal is in contact with the solution.

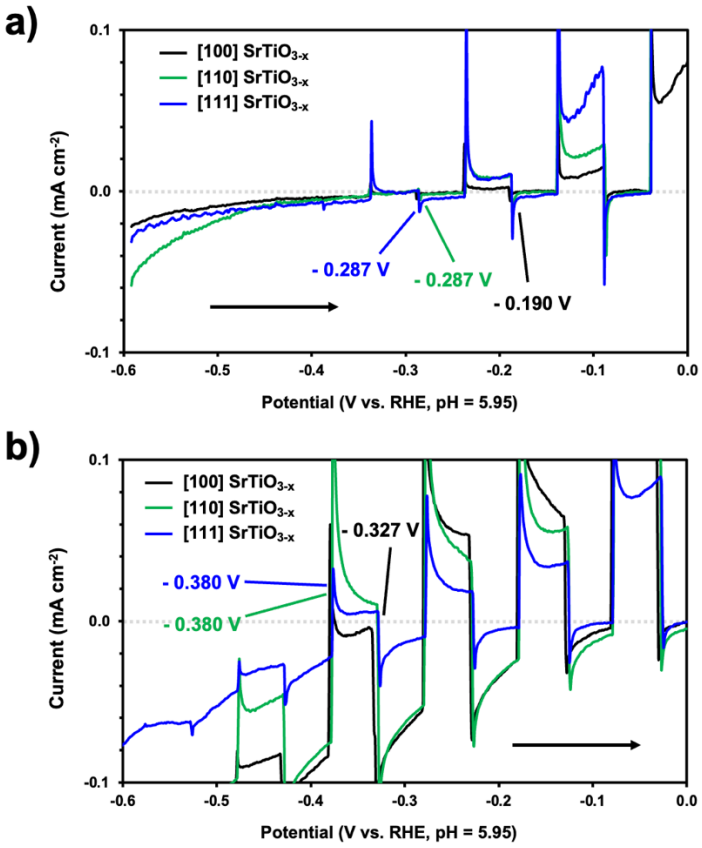

Figure 4.14. Zoomed-in PEC onset for H_2 annealed strontium titanate single crystals under UV illumination (60 mW cm^{-2}) from Xe Lamp in a) 0.50 M Na_2SO_4 aqueous solution, and b) 0.50 M Na_2SO_4 aqueous solution with 20% methanol (pH = 5.95). The scan direction is from negative to positive potential as indicated by the horizontal arrow. Active area of electrode in contact with solution is 0.50 cm^2.

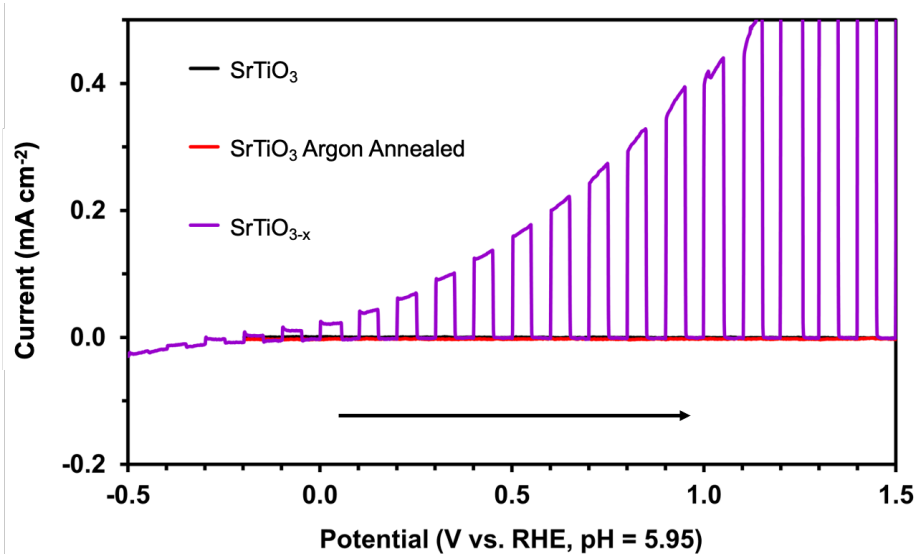

Figure 4.15. PEC scan in 0.50 M Na_2SO_4 aqueous solution under 60 mW cm^{-2} UV light illumination for as-received, Ar-annealed, and H_2-annealed $SrTiO_3$ single crystal with [111] exposed facet. The dataset was obtained from the same [111] $SrTiO_3$ single crystal sample. The sequence of measurements was as follows: PEC measurement was conducted on the as-received $SrTiO_3$ sample, followed by argon annealing at 500°C, and then another PEC measurement. Subsequently, H_2 annealing at 1,110°C was performed, followed by a final PEC measurement. The argon annealing was an attempt to induce the formation of oxygen vacancies, but it was not successful, which is why H_2 annealing was utilized. The scan direction is from negative to positive potential as indicated by the horizontal arrow. The active area of electrode in contact with solution is 0.50 cm^2.

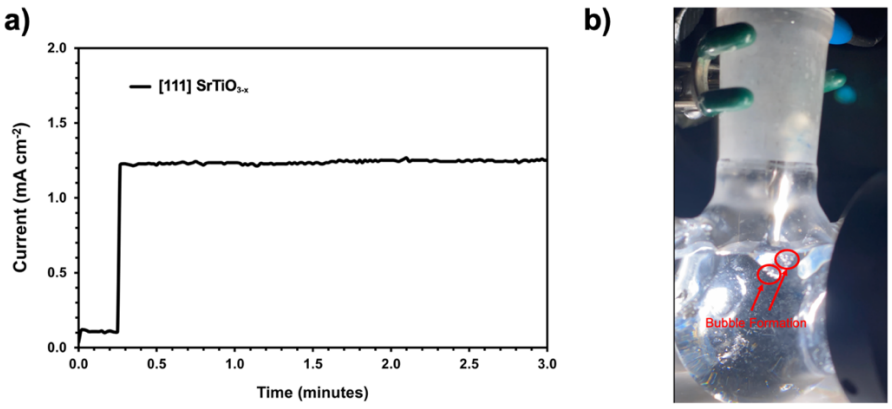

Figure 4.16. a) Chronoamperometry for H_2 annealed [111] $SrTiO_{3-x}$ single crystal at 1.23 V vs RHE in 0.50 M Na_2SO_4 aqueous solution under UV illumination 60 mW cm^{-2} Xe Lamp corresponding to the video of bubbles. The active area of electrode in contact with solution is 0.50 cm^2. b) Corresponding image of the video, the red circles highlight the bubble formation on the single crystal.

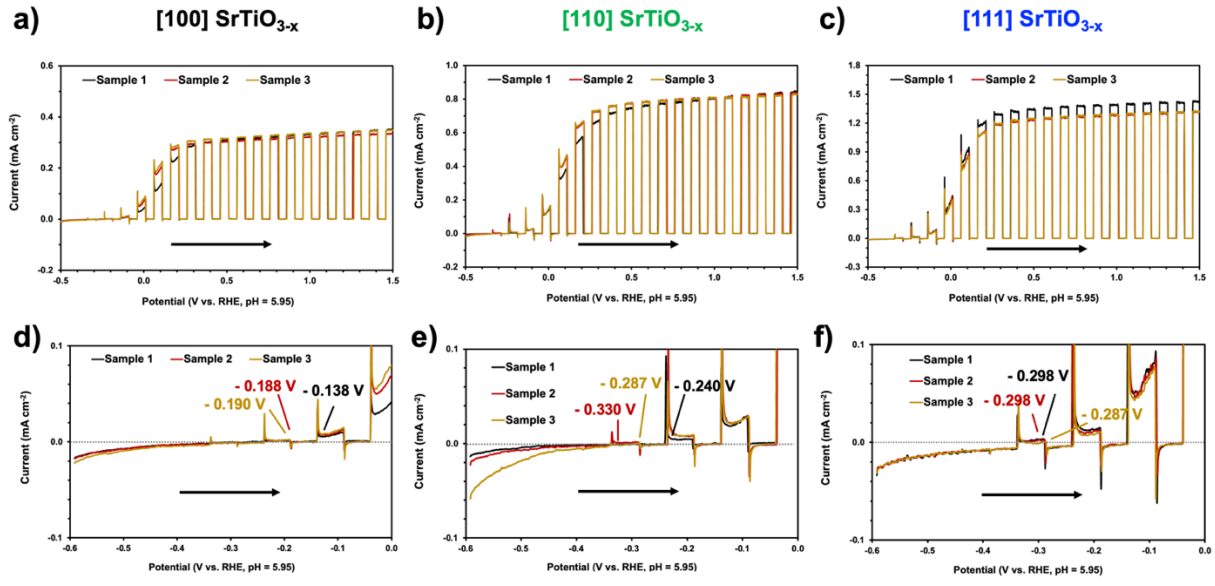

Figure 4.17. PEC for three samples of a) [100], b) [110], and c) [111] $SrTiO_{3-x}$ single crystals were each measured in 0.50 M Na_2SO_4 under UV light illumination (60 mW cm_{-2}) to determine the experimental error.

The zoomed in area to reveal the photo onset potential, E_{ON}, for d) [100], e) [110], and f) [111] $SrTiO_{3-x}$ single crystal is also shown. Sample 3 is also featured in **Figure 4.4**. The scan direction is from negative to positive potential as indicated by the horizontal arrow. The active area of electrode in contact with solution is 0.50 cm^2.

Table 4.3. Values and errors of photocurrent, photoonset, and photovoltage of three samples of [100, 110, 111] $SrTiO_{3-x}$ single crystals with different exposed facets corresponding to the data in **Appendix 4.17**.

	[100] $SrTiO_{3-x}$			**[110] $SrTiO_{3-x}$**			**[111] $SrTiO_{3-x}$**		
	Sample 1	**Sample 2**	**Sample 3**	**Sample 1**	**Sample 2**	**Sample 3**	**Sample 1**	**Sample 2**	**Sample 3**
Current (mA cm^{-2})	0.342	0.328	0.341	0.821	0.823	0.814	1.413	1.300	1.304
Photoonset (V RHE)	-0.138	-0.188	-0.190	-0.240	-0.330	-0.287	-0.298	-0.298	-0.287
Photovoltage (V)	1.37	1.42	1.42	1.47	1.56	1.52	1.53	1.53	1.52
Average Current (mA cm^{-2})	0.337			0.819			1.357		

Current Standard Deviation (absolute, %)	0.01, 2.97	0.00, 0.00	0.08, 5.89
Average Photoonset (V RHE)	-0.172	-0.286	-0.294
Photoonset Standard Deviation (absolute, %)	0.03, 17.4	0.05, 17.5	0.01, 3.40
Average Photovoltage (V)	1.40	1.52	1.52
Photovoltage Standard Deviation (absolute, %)	0.03, 2.14	0.05, 3.29	0.01, 0.65

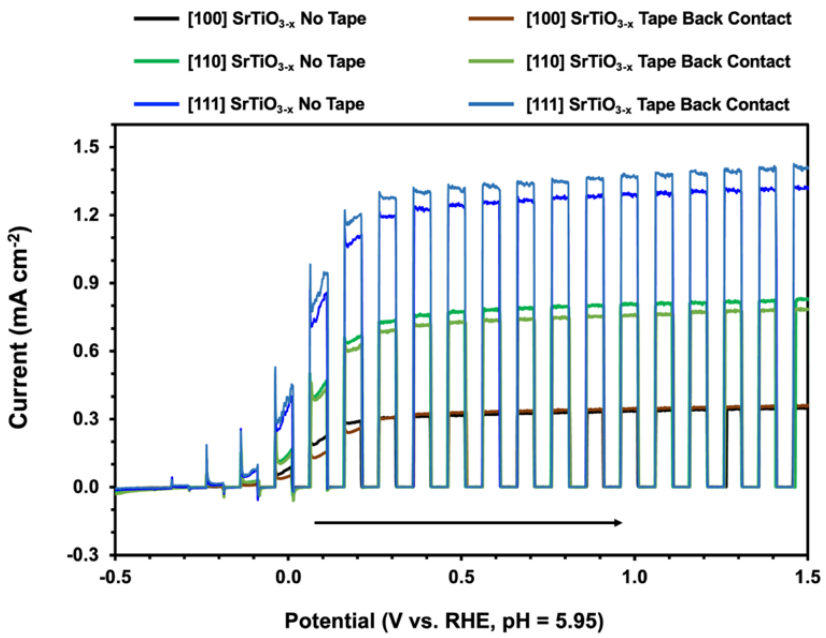

Figure 4.18. PEC comparison for H_2-annealed $SrTiO_3$ single crystals to evaluate the effect of polyester tape at the back contact. Conditions: InGa contact, 0.50 M Na_2SO_4 aqueous solution under UV illumination 60 mW cm^{-2} Xe lamp. The addition of tape to the back side only slightly reduces the photocurrent. This shows that most of the photocurrent is generated at the front side. Scan direction is from negative to positive potential as shown by the horizontal arrow.

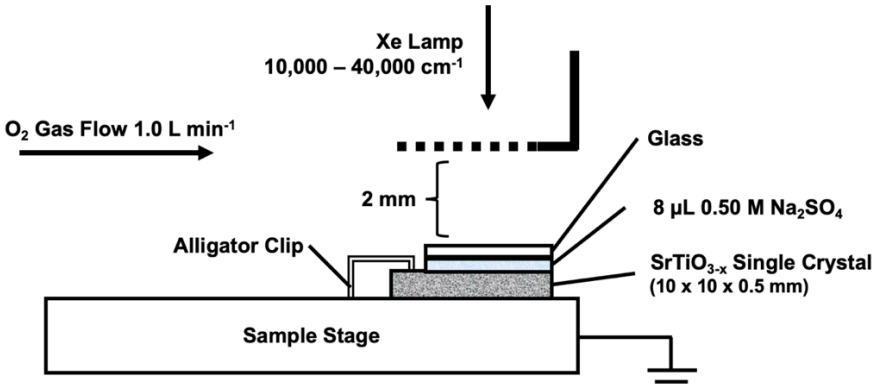

Figure 4.19. Surface photovoltage spectroscopy scheme.

Table 4.4. Values obtained from Mott Schottky experiment and calculations for free electron density, N_D, flat band potential, E_{FB}, and conduction band edge, E_{CB}.

	[100] $SrTiO_{3-x}$			**[110] $SrTiO_{3-x}$**			**[111] $SrTiO_{3-x}$**		
Band Gap (eV)	3.2			3.2			3.2		
Dielectric Constant (ε)	300			300			300		
Thickness (m)	0.0005			0.0005			0.0005		
Area (A / m^{-2})	0.0001			0.0001			0.0001		
Effective Density of States (N_{CB} / cm^{-3})	8.00×10^{20}			8.00×10^{20}			8.00×10^{20}		
Frequency (Hz)	100	125	150	100	125	150	100	125	150
Potential (x-intercept)	-0.570	-0.542	-0.579	-0.666	-0.687	-0.699	-0.725	-0.712	-0.720
Flatband Potential (E_{FB} / V vs RHE)	-0.596	-0.567	-0.605	-0.692	-0.713	-0.725	-0.751	-0.738	-0.745
Slope ($C^{-2} \times 10^9$)	26.467	18.233	22.800	96.329	92.204	86.322	3.831	3.615	3.724
Free Electron Density (N_D / m^{-3})	1.78×10^{25}	2.58×10^{25}	2.06×10^{25}	4.88×10^{24}	5.10×10^{24}	5.44×10^{24}	1.23×10^{26}	1.30×10^{26}	1.26×10^{26}
Free Electron Density (N_D / cm^{-3})	1.78×10^{19}	2.58×10^{19}	2.06×10^{19}	4.88×10^{18}	5.10×10^{18}	5.44×10^{18}	1.23×10^{20}	1.30×10^{20}	1.26×10^{20}
Conduction Band	-0.69	-0.66	-0.70	-0.82	-0.84	-0.85	-0.80	-0.78	-0.79

Edge (E_{CB} / V vs RHE)									
Valence Band Edge (E_{VB} / V vs RHE)	2.51	2.54	2.50	2.38	2.36	2.35	2.40	2.42	2.41
Junctions	$SrTiO_3$ / O_2/H_2O			$SrTiO_3$ / O_2/H_2O			$SrTiO_3$ / O_2/H_2O		
E^0 (V vs RHE)	1.23			1.23			1.23		
Built-in Potential, V_{bi} (V)	1.83	1.80	1.83	1.92	1.94	19.5	1.98	1.97	1.97
Depletion layer width (nm)	58.39	48.09	54.33	114.29	112.43	109.12	23.14	22.41	22.78

Mott-Schottky measurements were performed using a Gamry Reference 600 Potentiostat at an applied frequency of 100-150 Hz. The space charge capacitance, C, varies with the applied potential over the depletion layer as determined by the Mott-Schottky equation:

$$\frac{1}{C^2} = (\frac{2}{\varepsilon\varepsilon_0 A^2 e N_D})(\mathrm{V} - E_{FB} - \frac{k_B T}{e})$$

Here, *e* is the electron charge, ε is the dielectric constant, ε_0 is the permittivity of a vacuum, N_D is the free electron density, V is the applied bias, E_{FB} is the flatband potential, k is the Boltzmann constant, T is the temperature, and A is the surface area of the film in contact with the electrolyte. Therefore, a plot of C^{-2} versus V yields a straight line with a slope than can be used to determine N_D.

Slope = $(2/e\ \varepsilon\ \varepsilon_0 N_D A^2)$; Given ε of $SrTiO_3$ = 300, [48] A = 0.0001 m^2, $\varepsilon_0 = 8.8541 \times 10^{-12}$ C m^{-1} V^{-1}, and e = 1.60×10^{-19} C, for [111] $SrTiO_{3-x}$ at 100 Hz, the slope = 3.83×10^9 C^{-2} F^2 and the calculated N_D value of 1.23×10^{20} cm^{-3} was obtained. Using the Mott-Schottky equation, the flatband potential is determined from

the intercept with the x-axis on the linear plot of C^{-2} versus V and converted from SCE to RHE. The x-axis intercept was -0.725 V RHE at pH = 5.95, and therefore E_{FB} is -0.751 V vs RHE.

The conduction band position, E_{CB}, is determined from the equation for a n-type semiconductor: $E_{CB} = E_{FB} + k_BT \times \ln (N_D / N_{CB})$ where the effective density of states, N_{CB}, for doped $SrTiO_3$ was found to be approximately 8.00×10^{20} cm^{-3}. [49] Therefore, for [111] $SrTiO_{3-x}$ at 100 Hz, E_{CB} = -0.80 V RHE.

Strontium titanate has a band gap value of 3.2 eV, [28] and the position of the valence band can be determined by adding the bandgap value to the conduction band position, E_{CB}. The conduction band position is therefore at approximately +2.40 V RHE at pH = 5.95.

The space charge region (SCR), or the depletion layer width, *w*, is calculated using the following formula:

$$w = \sqrt{\frac{2\varepsilon\varepsilon_0 V_{bi}}{eN_D}}$$

Here, *e* is the electron charge, ε is the dielectric constant, ε_0 is the permittivity of a vacuum, N_D is the free electron density, and V_{bi} is the built in potential.

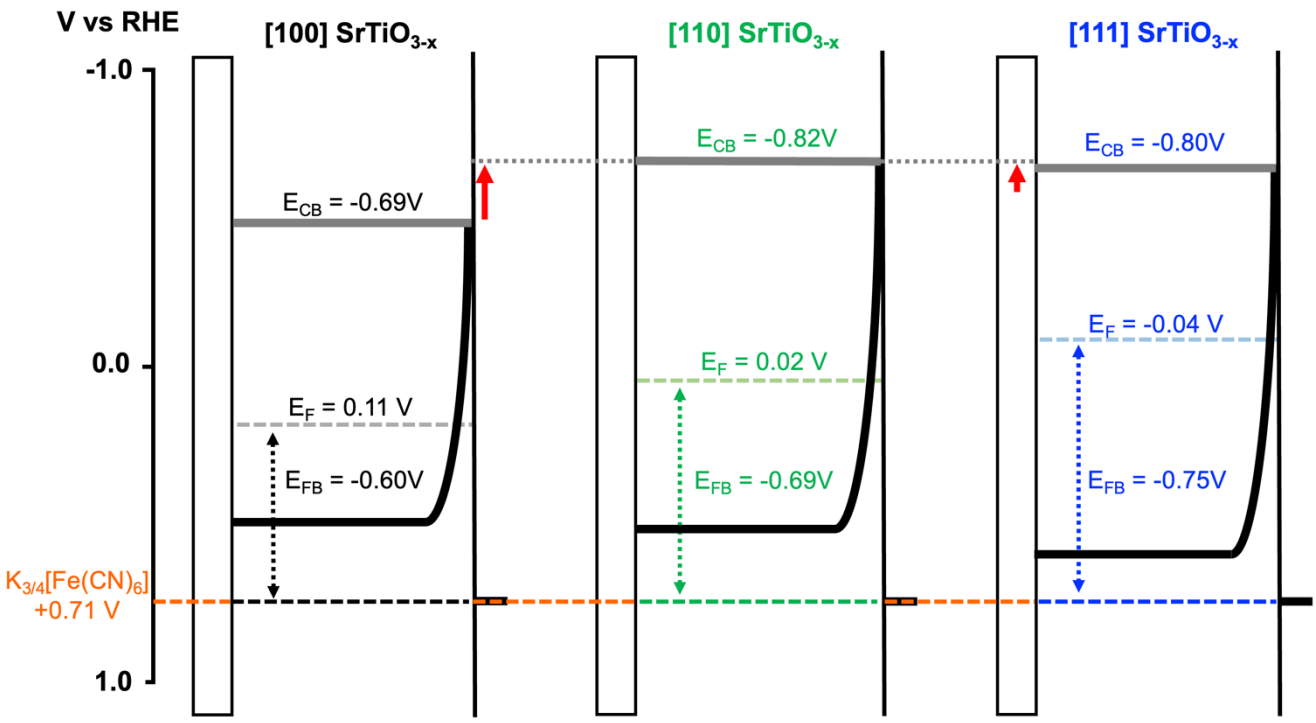

Figure 4.20. Band energy diagram for H_2-annealed $SrTiO_{3-x}$ single crystals with E_{CB}, E_F, and E_{FB}, positions based on Mott Schottky calculations in 50 mL 0.50 M Na_2SO_4 aqueous solution with 50 mM equimolar $K_3/_4[Fe(CN)_6]$ redox couple (E^0 = 0.71 V vs RHE at pH = 5.95). E_{CB} values for each facet of $SrTiO_{3-x}$ were obtained based on calculations explained in the subscript of **Table 4.4**. The flat band potential is defined as the potential required to remove the depletion layer at the semiconductor-electrolyte junction given the fermi level of the semiconductor equilibrates with the redox potential of the solution. Thus, the fermi level, E_F, can be calculated from the difference in the flatband potential, E_{FB}, from the redox potential of the solution, in this case E^0 $K_3/_4[Fe(CN)_6]$ = 0.71 V RHE at pH 5.95.

Bode and Nyquist Plots

To further characterize the electric properties of the $SrTiO_{3-x}$/liquid junction, electrochemical impedance spectroscopy (EIS) experiments were performed. The Bode plot (**Appendix 4.21**) shows symmetric phase

change corresponding to the frequency change. The corresponding Nyquist plot (**Appendix 4.22**) displays a semi-circle indicating that the system resembles a simplified Randles Circuit (shown next to plot). At high frequency, impedance is low and most current flows through the capacitor (Q_1). As frequency decreases, the impedance increases and most current moves through the resistor (R_1). At the lowest frequency, the capacitor has no current flow, and the observed resistance is from the charge transfer resistance, R_1. The charge transfer resistance (R_1) is defined by the diameter of the semi-circle (**Appendix 4.22a**). Accordingly, the [111] $SrTiO_{3-x}$ crystal has the lowest charge transfer resistance followed by [100] and [110] $SrTiO_{3-x}$ which mimics the order of relative N_D values in the series. The largest $N_D = 1.23 \times 10^{20}$ cm^{-3} for [111] $SrTiO_{3-x}$ followed by [100] $SrTiO_{3-x}$ (1.78×10^{19} cm^{-3}) and [110] $SrTiO_{3-x}$ (4.88×10^{18} cm^{-3}). [50]

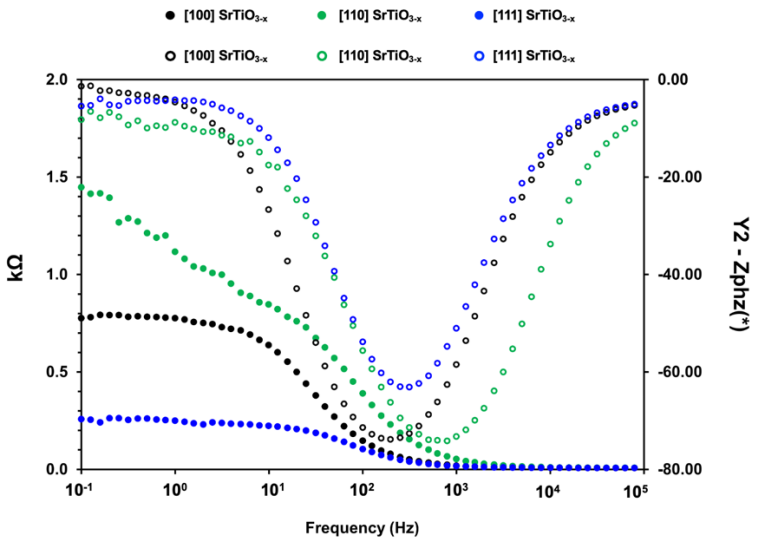

Figure 4.21. Bode plot of [100] $SrTiO_{3-x}$ (black), [110] $SrTiO_{3-x}$ (green), and [111] $SrTiO_{3-x}$ (blue) in 0.50 M Na_2SO_4 aqueous solution with $K_3/_4[Fe(CN)_6]$ under constant N_2 purging with no illumination. The working electrode consists of $SrTiO_{3-x}$ single crystals with InGa eutectic coating at the back contact, connected to a stainless steel alligator clip. Active area of the system is 1.0 cm^2 (both sides of the single crystal are in contact with the solution). Solid spheres are the impedance and the hollow spheres are the

phase.

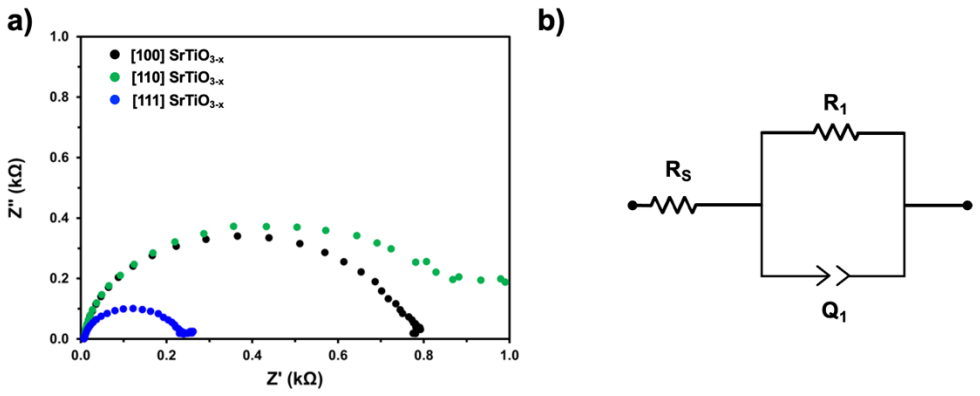

Figure 4.22. a) EIS measurement for [100] $SrTiO_{3-x}$ (black), [110] $SrTiO_{3-x}$ (green), and [111] $SrTiO_{3-x}$ (blue) in 0.50 M Na_2SO_4 aqueous solution with 50 mM $K_3/_4[Fe(CN)_6]$ under constant N_2 purging with no illumination. The working electrode consists of a $SrTiO_{3-x}$ single crystal with InGa eutectic coating connected to the stainless steel alligator clip. b) Randles circuit model for the Nyquist plot where the Faradaic (charge transfer resistance, R_1) and the non-Faradaic (double-layer capacitance, Q_1) current flow through the solid/electrolyte interface, and R_S accounts for all resistances associated with solution resistance, wires, clips, or other contacts. Non-Faradaic processes include molecular adsorption and desorption at electrode-solution interface which affects the potential but does not involve charge transfer between the junctions.

4.6 References

1. Chen S., Takata T., and Domen K.; *Nature Reviews Materials*, **2017**, *2*, 17050.

2. Wang Q., Domen K.; *Chemical Reviews*, **2020**, *120*, 2, 919-985.

3. Wang Z., Li C., Domen K..; *Chemical Society Reviews*, **2019**, *48* (7), 2109-2125.

4. Chen S., Takata T., Domen, K.; *Nature Reviews Materials*, **2017**, *2* (10), 17050.

5. Takanabe K.; *ACS Catalysis*, **2017**, *7* (11), 8006-8022.

6. Zhao T., Yanagi R., Xu Y., He Y., Song Y., Yang M., Hu S.; *Proceedings of the National Academy of Sciences of the United States of America*, **2021**, *118* (7), e2023552118.

7. Yanagi R., Zhao T., Solanki D., Pan Z., Hu S.; *ACS Energy Letters*, **2022**, *7*, 1, 432-452.

8. Kudo A., and Miseki Y.; *Chemical Society Reviews*, **2009**, *38*, 253-278.

9. Yang J. H., Wang D. G., Han H. X., Li C.; *Accounts of Chemical Research*, **2013**, *46*, 1900-1909.

10. Gurlo A.; *Small*, **2010**, *6* (19), 2077−2079.

11. Yang Q., Dong L., Su R., Hu B., Wang Z., Jin Y., Wang Y., Besenbacher F., Dong M.; *Applied Materials Today*, **2019**, *17*, 159−182.

12. Zhang A.-Y., Wang W.-Y., Chen J.-J., Liu C., Li Q.-X., Zhang X., Li W.-W., Si Y., Yu H.-Q.; *Energy and Environmental Science*, **2018**, *11* (6), 1444−1448.

13. Luo Y., Suzuki S., Wang Z., Yubuta K., Vequizo J. J. M., Yamakata A., Shiiba H., Hisatomi T., Domen K., Teshima K.; *ACS Applied Materials and Interfaces*, **2019**, *11* (25), 22264−22271.

14. Li R., Zhang F., Wang D., Yang J., Li M., Zhu J., Zhou X., Han H., Li C.; *Nature Communications*, **2013**, *4*, 1432.

15. Kashiwaya S., Toupance T., Klein A., and Jaegermann W.; *Advanced Energy Materials*, **2018**, *8*, 1802195.

16. Avcıoğlu C., Avcıoğlu S., Bekheet M. F., and Gurlo A.; *ACS Applied Energy Materials*, **2023**, *6*, 1134 - 1154.

17. Kato H., Kobayashi M., Hara M., Kakihana M.; *Catalysis Science and Technology*, **2013**, *3* (7), 1733.

18. Mu L., Zhao Y., Li A., Wang S., Wang Z., Yang J., Wang Y., Liu T., Chen R., Zhu J., Fan F., Li R., and Li C.; *Energy and Environmental Science*, **2016**, *9*, 2463.

19. Takata T., Jiang J., Sakata Y., Nakabayashi M., Shibata N., Nandal V., Seki K., Hitasomi T., Domen K.; *Nature*, **2020**, *581*, 411–414.

20. Biswas A., Rossen P. B., Yang C.-H., Siemons W., Jung M.-H., Yang I. K., Ramesh R., and Jeong Y. H.; *Applied Physics Letters*, **2011**, *98*, 051904.

21. Aballe L., Matencio S., Foerster M., Barrena E., Sánchez F., Fontcuberta J., Ocal C.; *Chemistry of Materials*, **2015**, *27* (18), 6198−6204.

22. Holmström E., Spijker P., Foster A. S.; *Proceedings of the Royal Society A*, **2016**, *472* (2193), 20160293.

23. Alexandrov V. E., Kotomin E. A., Maier J., Evarestov R. A.; E*uropean Physical Journal B*, **2009**, *72* (1), 53−57.

24. Wang C., Wu D., Wang P., Ao Y., Hou J., Qian J.; *Applied Surface Science*, **2015**, *325*, 112-116.

25. Lv Y., Liu Y., Zhu Y., Zhu Y.; *Journal of Materials Chemistry A*, **2014**, *2*, 1174-1182.

26. Tan H., Zhao Z., Zhu W.-B., Coker E. N., Li B., Zheng M., Yu W., Fan H., and Sun Z.; *ACS Applied Materials and Interfaces*, **2014**, *6*, 21, 19184-19190.

27. Dong G., Wang X., Chen Z., and Lu Z.; *Photochemistry and Photobiology*, **2018**, *94*: 472-483.

28. Mavroides J. G., Kafalas J. A., Kolesar D. F.; *Applied Physics Letters*; **1976**, *28* (5), 241-243.

29. Yamada H., Miller G. R.; *Journal of Solid State Chemistry*, **1973**, *6*, 169-1777.

30. Xie K., Umezawa N., Zhang N., Reunchan P., Zhang Y., Ye J.; *Energy and Environmental Science*, **2011**, *4*, 4211-4219.

31. Wang C., Koirala P., Stair P., Marks L.; *Applied Surface Science*, **2017**, *422*, 661-665.

32. Hrabovsky D., Berini B., Fouchet A., Aureau D., Keller N., Etcheberry A., Dumont Y.; *Applied Surface Science*, **2016**, *367*, 307-311.

33. Vasquez R. P.; *Journal of Electron Spectroscopy and Related Phenomena*, **1991**, *56*, 217-240.

34. Chen H., Zhang F., Zhang W., Du Y.; *Applied Physics Letter*, **2018**, *112*, 013901.

35. Fu Y., Du H., Zhang S., Huang W.; *Material Science and Engineering A*, **2005**, *403*, 25–31.

36. Zhao Z.; *Energy and Environmental Science*, **2019**, *5*, 6081-6088.

37. Baek J. Y., Duy L. T., Lee S. Y., Seo H.; *Journal of Materials Science and Technology*, **2020**, *42*, 28-37.

38. Wang X., Huang K., Qian J., Cong Y., Ge C., Feng S.; *Science Bulletin*, **2017**, *62*, 658-664.

39. Crumlin E. J., Mutoro E., Liu Z., Grass M. E., Biegalski M. D., Lee Y.-L., Morgan D., Christen H. M., Bluhm H., and Shao-Horn Y.; *Energy and Environmental Science*, **2012**, *5*, 6081-6088.

40. Young V., Otagawa T.; *Applications of Surface Science, **1985**, 20*, 228-248.

41. Liu X., Cao Y., Pal B., Middey S., Kareev M., Choi Y., Shafer P., Haskel D., Arenholz E., and Chakhalian J.; Physical Review Materials, 2017, 1, 075004.

42. Kronik L., Shapira Y.; *Surface Science Reports*, **1999**, *37*, 1–206.

43. Dittrich T., and Fengler S.; Surface Photovoltage Analysis of Photoactive Materials; World Scientific Publishing Europe Ltd: **2020**.

44. Doughty, R.M., Hodges B., Dominguez J., Han R., Zhao Z., Assavachin S., Osterloh F. E.; *The Journal of Physical Chemistry C*; **2020**, *124* (34), 18426-18435.

45. Doughty, R.M., Chowdhury F. A., Mi Z., Osterloh F. E.; *The Journal of Physical Chemistry C*; **2020**, *153* (14), 144707.

46. Cheng, Y., Xiao C., Mahmoudi B., Scheer R., Maijenburg A.W., and Osterloh F.E.; *EES Catalysis*, **2023**, *1*, 74-83.

47. Ma X., Cui X., Zhao Z., Melo M. A. Jr., Roberts E. J., Osterloh F. E.; *Journal of Materials Chemistry A*, **2018**, *6*, 5774-5781.

48. Weaver H. J.; *Journal of Physics and Chemistry of Solids*, **1959**, *11*, 274–277.

49. Wang Q., Hisatomi T., Suzuki Y., Pan Z., Seo J., Katayama M., Minegishi T., Nishiyama H., Takata T., Seki K., Kudo A., Yamada T., and Domen K.; *Journal of the American Chemical Society*; **2017**, *139*

(4), 1675-1683.

50. Mei B. A., Munteshari O., Lau J., Dunn B., and Pilon L.; *Journal of Physical Chemistry C*, **2018**, *122*, 194−206.

Chapter 5 - Ferroelectric Polarization in $BaTiO_3$ Nanocrystals controls Photoelectrochemical Water Oxidation and Photocatalytic Hydrogen Evolution

5.1 Introduction

Ferroelectric (FE) materials exhibit a spontaneous electric polarization that can be reversed through application of an external electric field. The ferroelectric (FE) effect was discovered in 1920 in potassium sodium tartrate tetrahydrate (the Rochelle salt) by Joseph Valasek, and later in $BaTiO_3$ and other materials ($PbTiO_3$, $BiFeO_3$, $LiNbO_3$, $KNbO_3$). [1-3] In some compounds, such as $BiFeO_3$, the ferroelectric polarization is due to changes in bonding, [4] while in others, such as barium titanate, it is due to the displacement of a Ti(4+) ion from its equilibrium position (**Figure 5.1**). [5] In $BaTiO_3$, this ion shift occurs below the ferroelectric Curie Temperature (110-120°C) [6-8] and is accompanied by a change from the cubic to the tetragonal crystal structure.

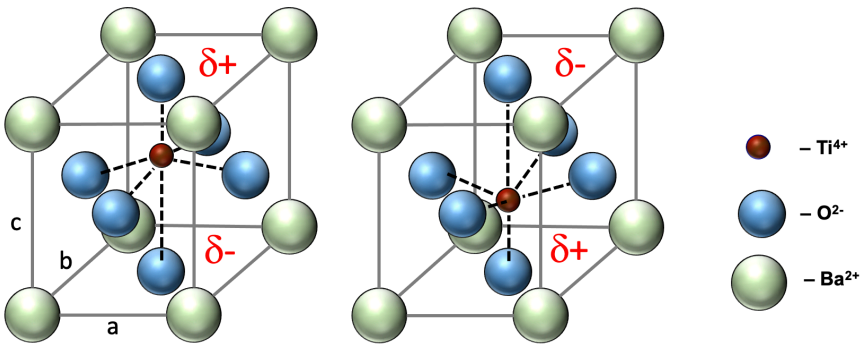

Figure 5.1. Unit cell of tetragonal $BaTiO_3$ with titanium center displacement leading to a ferroelectric dipole.

In ferroelectric semiconductors, the FE dipole may affect the direction of charge separation under illumination. [9-12] This can produce an anomalous (or bulk) photovoltaic effect, when the photovoltage exceeds the band gap of the semiconductor. [13] For example, ferroelectric $BiFeO_3$ films support photovoltages of 16 V and the short circuit currents densities of 0.12 mA cm^{-2} under certain conditions. [14] The high solar energy conversion efficiency of lead iodide perovskite photovoltaics ($CH_3NH_3PbI_3$) has also been attributed to an FE effect. [9, 15]

While the FE effect is well established in photovoltaics, there is less convincing proof for it in solar fuel photoelectrochemistry and photocatalysis. [10, 16-17] This is because photocatalysts for thermodynamically unfavorable fuel forming reactions, such as the water splitting reaction, [18-19] are influenced by many factors, including polar surface terminations, surface recombination, and kinetic overpotentials. This makes it very difficult to attribute observed activity variations solely to ferroelectric effects. [20-23] Also, many ferroelectric materials with visible band gaps, including $BiFeO_3$ and $PbTiO_3$, are not stable under water electrolysis conditions. Some of these challenges can be avoided by focusing on dye degradation reactions, [21, 24-26] however, because photocatalytic dye degradation reactions are thermodynamically downhill ($\Delta G < 0$) they do not provide information about the energy conversion efficiency of the catalysts. [27-28] Another problem is that ferroelectric photoelectrodes are often polarized electrically in the presence of electrolytes and air, [29-31] where they may be changed as a result of oxidation/reduction reactions under these conditions. [32]

Some of the most direct evidence for FE-controlled photoelectrochemistry was obtained for $BaTiO_3$ crystals in Rohrer's group. [33-34] When the crystals are illuminated, reductive silver photodeposition takes place preferentially on the positive FE domains, while oxidative PbO_2 deposition occurs on the negatively charged domains. A similar reactivity was also observed in $BiVO_4$ phases after doping with Na and Mo [35] and in TiO_2 coated $BiFeO_3$. [36] This confirms that the FE dipole in these metal oxides can guide the direction

of photogenerated charge carrier transport. Electrically polarized ferroelectric $BaTiO_3$ single crystals also have extended carrier lifetimes, [37] which was attributed to improved charge separation. In confirmation of this interpretation, the enhancement can be turned off by heating the crystal above the ferroelectric Curie Temperature T_C (110-120°C). [6-8] Very recently, Magnan et al. reported that $BaTiO_3$ films displayed electric polarization-dependent photocurrent for water oxidation. [32] However, doping of $BaTiO_3$ during electrochemical polarization in electrolyte could not be ruled out. Similarly, Liu et al, reported FE-controlled reductive and oxidative photodeposition of Cr_2O_3 and MnO_x onto a gold-modified $BaTiO_3$ single crystal. [38] Sub-micromolar amounts of H_2 and O_2 were detected when a Rh/Cr_2O_3 and CoOOH-modified $Au/BaTiO_3$ crystal was exposed to UV light, but it was not clear if gas evolution was catalytic and if it was promoted by a ferroelectric effect.

In continuation of our work on ferroelectric photocatalysts [39] we report here on the first observation of ferroelectrically enhanced photoelectrochemical water oxidation and hydrogen evolution with $BaTiO_3$ nanocrystals. Single crystals in the tetragonal ferroelectric form were obtained by hydrothermal reaction of TiO_2 and $Ba(OH)_2$. When the nanocrystals are deposited on tantalum substrates they are able to oxidize water to O_2 under UV illumination and with an applied bias. The photocurrent can be enhanced or suppressed reversibly through prior electric polarization of the films under inert conditions. A prior applied electric field also increases the photocatalytic H_2 evolution with Pt-modified $BaTiO_3$ nanocrystals by a factor of 1.5 and it directs photochemical silver deposition to the (001) facets. Importantly photocurrent and H_2 evolution activity are restored to their original value by heating the $BaTiO_3$ nanocrystals above their Curie temperature. These findings not only show that the photoelectrochemical properties of $BaTiO_3$ nanocrystals are controlled by a ferroelectric effect, but also that the effect can be utilized for the photoelectrochemical generation of H_2 fuel.

5.2 Results and Discussion

Figure 5.2 gives an overview over the synthesis of the $BaTiO_3$ nanocrystals and the fabrication of thin films and photocatalysts from them. The synthesis of $BaTiO_3$ was achieved by heating P25 TiO_2, $Ba(OH)_2$ and KOH in water to 180°C under hydrothermal conditions, similar to the published procedure. [40] After 72 h, the reaction is complete and provides barium titanate nanocrystals in 63 % yield (based on TiO_2).

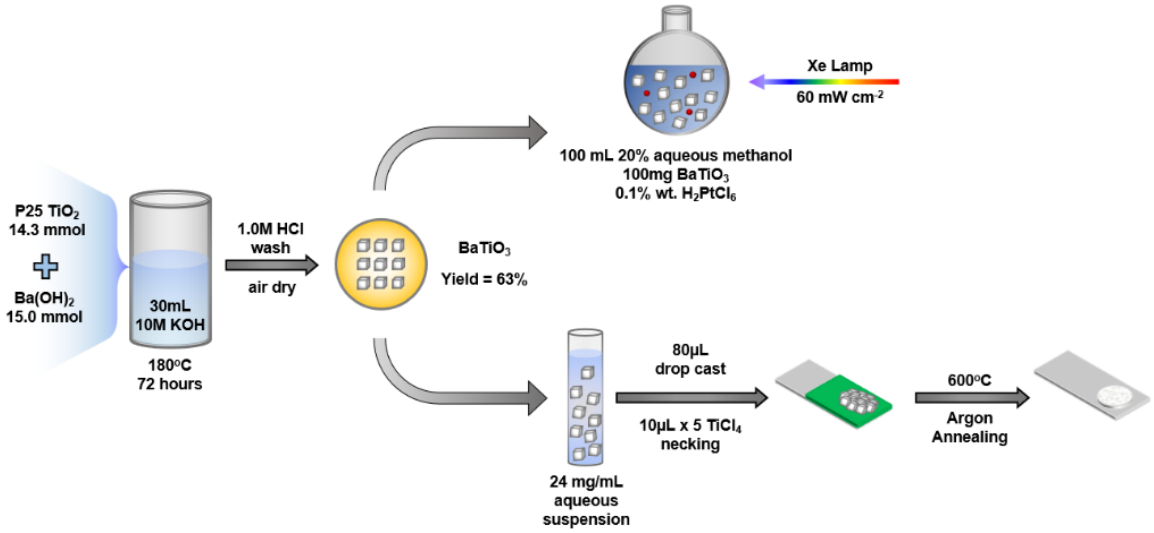

Figure 5.2. Hydrothermal synthesis of $BaTiO_3$ nanocrystals, thin films and Pt/$BaTiO_3$ photocatalysts.

According to SEM and TEM images in **Figure 5.3**, the crystals are 242 nm (±90.8 nm) in size (histogram in **Appendix 5.11**). The morphology of the crystals is dominated by the ⟨100⟩ family of facets and about 90 % of them appear tetragonal with one dimension expanded. Some of the crystals are truncated at the corners, exposing ⟨111⟩ facets there. The SAED pattern for a single nanocrystal in **Figure 5.3e** shows a single set of reflections that can be indexed to the tetragonal lattice of $BaTiO_3$. This confirms that the nanocrystals are single crystals. The powder XRD pattern in **Figure 5.4a** can be indexed to the tetragonal crystal structure of $BaTiO_3$. [41] Based on the absence of any impurity peaks, the obtained material is phase-

pure. Interestingly, the hydrothermal procedure by Tsumura et al. produces cubic $BaTiO_3$, which may be attributed to the lower synthesis temperature (150°C) compared to the conditions used here (180 °C). [40] The cubic to tetragonal transition temperature for $BaTiO_3$ is 120°C. [41] We also find that highly basic conditions are required to obtain a uniform product. The $BaTiO_3$ particles are obtained as a white powder, consistent with the diffuse reflectance spectrum in **Figure 5.4b**. Based on the absorption onset, the band gap is found at 3.1 eV, near literature values (3.0-3.3 eV). [19, 42]

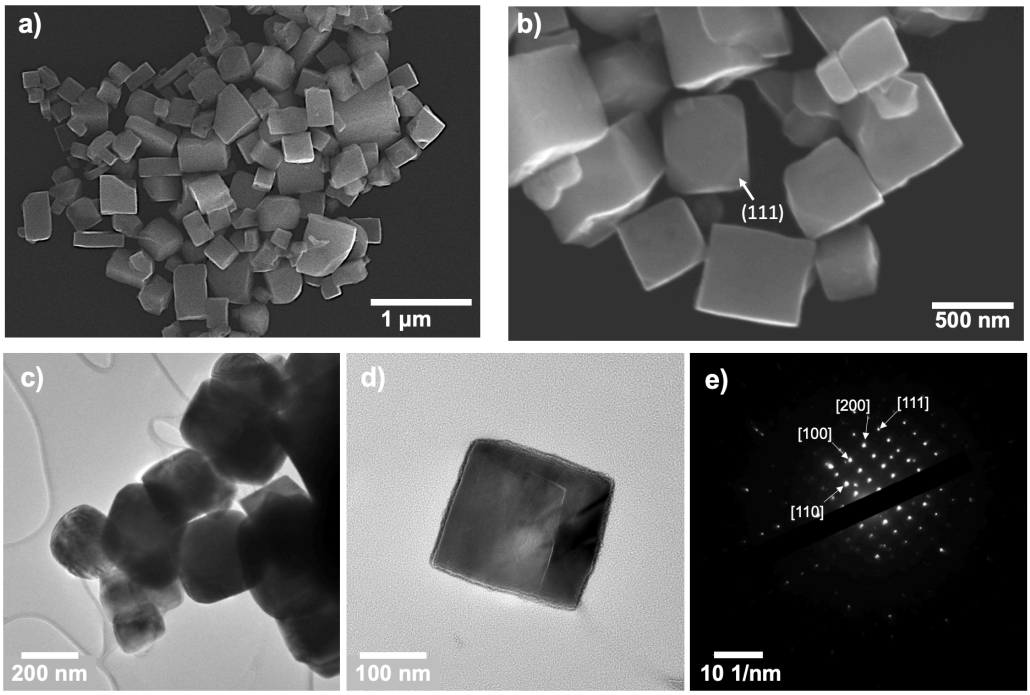

Figure 5.3. Electron micrographs of $BaTiO_3$. a,b) SEM images. c,d) TEM images. e) SAED pattern.

To evaluate the photoelectrochemical properties of the material, $BaTiO_3$ particle films were fabricated as shown in **Figure 5.2**, by drop-coating a $BaTiO_3$ particle suspension in deionized water onto a precleaned (10 % hydrofluoric acid) tantalum substrate. Tantalum was chosen because its low work function of 4.25 eV [43] favors an Ohmic contact with n-type $BaTiO_3$. The dried particle film was then treated with a 5 x 10

μL 20 mM $TiCl_4$ suspension in anhydrous methanol, followed by annealing at 600°C in argon. This 'necking method' produces a network of TiO_2 that enhances the conductivity in particle films. [44] Based on optical appearance and SEM images (**Figure 5.4c, d**), the resulting film is thin with most $BaTiO_3$ particles in direct contact with the Ta substrate.

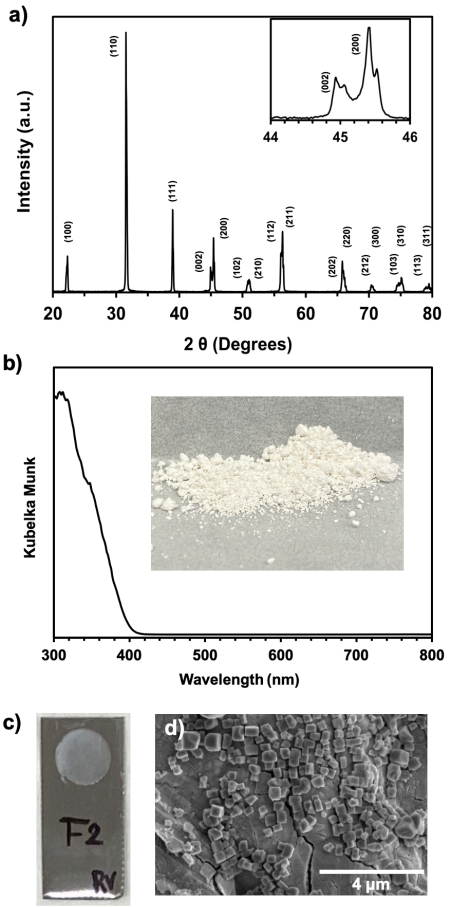

Figure 5.4. a) Powder XRD pattern of hydrothermal synthesized $BaTiO_3$. The pattern matches the 1507756 reference at the Crystallography Open Database (COD). The inset shows 002 and 200 peaks indicating the tetragonal crystal phase. Each reflection is split further, due to the splitting of the Cu-Kα emission, as reported previously. [45] b) Kubelka Munk spectrum of $BaTiO_3$ powder with photo as insert. c) Photo and d) SEM of $BaTiO_3$ film on tantalum.

The Ta/$BaTiO_3$ film was mounted inside of an electrochemical cell containing 0.50 M Na_2SO_4 aqueous solution (pH = 5.95), and used to record a linear sweep voltammogram under chopped UV light illumination (60 mW cm^{-2}) from a 300 W Xe lamp source (**Figure 5.5b**, experimental apparatus is shown in **Appendix 5.12**). The anodic photocurrent (0.141 mA cm^{-2} at 1.23 V RHE) is mainly from excitation of $BaTiO_3$ (**Appendix 5.13**) and comparable to a previous literature report. [46] The current is stable over a 1.0 h period and due to water oxidation, as evidenced by the formation of gas bubbles (**Appendix 5.14** and movie in Supporting Information). Overall, the current appears limited by the optical absorbance of the $BaTiO_3$ monolayer in the film.

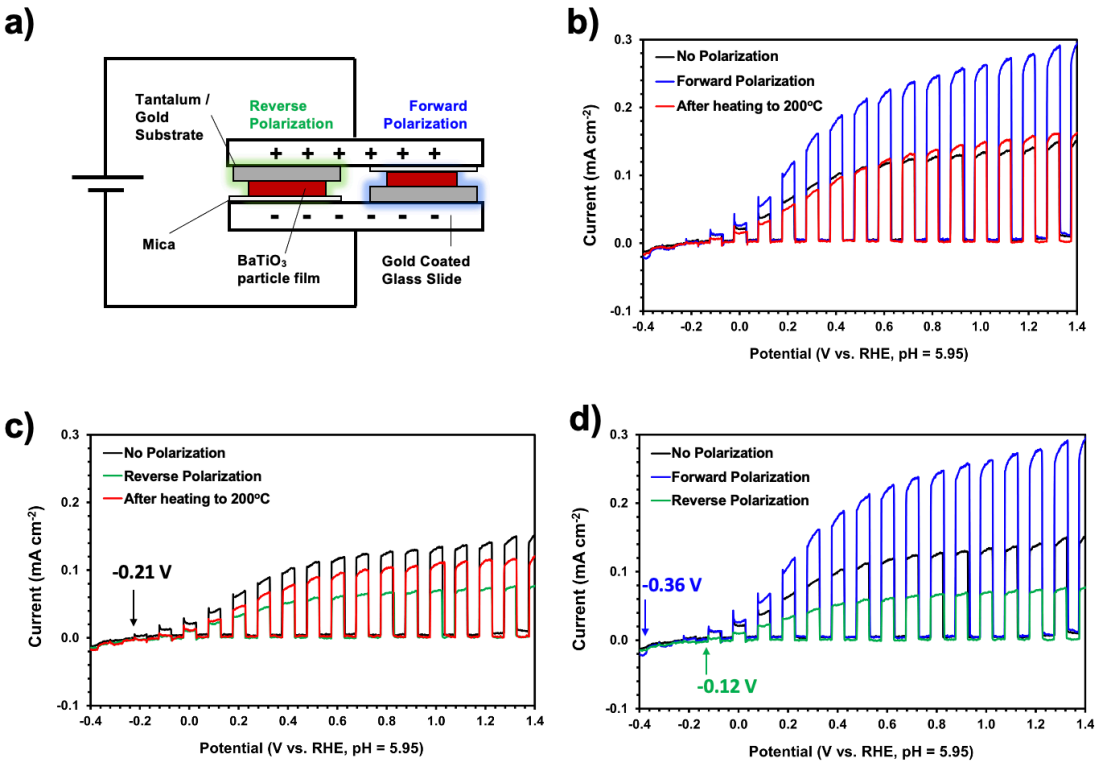

Figure 5.5. a) Polarization of the Ta/$BaTiO_3$ film at room temperature in high-purity argon atmosphere. In 'Forward polarization' the tantalum substrate was connected to the negative lead and in 'Reverse polarization' to the positive lead of the power supply. b) Photoelectrochemical scans of $BaTiO_3$ films before

polarization, after Forward polarization, and after heating to 200°C in argon, c) before polarization, after Reverse polarization, and after heating to 200°C in argon, and d), before and after Forward or Reverse polarization. Photocurrent onset potentials E_{on} are shown as numerical values. Conditions: 0.50 M Na_2SO_4 aqueous solution (pH = 5.95) under chopped UV light illumination (60 mW cm^{-2}) from a 300 W Xe lamp source. Voltametric scans were conducted from negative to positive applied potential. Repeat measurements on multiple samples and error analysis are presented in **Appendix 5.15** and **Tables 5.1/5.2**.

After the PEC scan, the Ta/$BaTiO_3$ film was removed, cleaned with deionized water, dried, and exposed to an electric field of 52.8 kV cm^{-1} for 1.0 h in Forward Polarization orientation as defined in **Figure 5.5a**. When the PEC scan was repeated, the photocurrent (0.276 mA cm^{-2} at 1.23 V RHE) increased by a factor of 1.95. The film was removed again, rinsed with water, and annealed at 200ºC for 30 minutes in air to reset the polarization in $BaTiO_3$ (the FE Curie Temperature is 110-120ºC for $BaTiO_3$). [6-8] When the PEC scan was repeated (**Figure 5.5b**), the anodic photocurrent (0.157 mA cm^{-2} at 1.23 V RHE) was nearly the same as observed for the non-polarized film. Next, the same film was rinsed, dried, and polarized in Reverse Polarization direction, and the PEC scan was repeated (**Figure 5.5c**), to reveal a photocurrent of 0.073 mA cm^{-2} at 1.23 V RHE (decreased by a factor of 1.93 compared to the non-polarized film). Finally, the film was washed, dried, and heated to 200°C, as before, to yield the PEC response in **Figure 5.5c**, with a photocurrent (0.114 mA cm^{-2} at 1.23 V RHE), restored to 81% of the original value. Overall, the Forward Polarization enhances the photocurrent by a factor of ~2 and reverse polarization diminishes it by the same factor (**Figure 5.5d**). This behavior was reproducible with four additional films (**Appendix 5.15**), resulting in a mean photocurrent increase of 1.97 ± 10.7% and decrease of 3.46 ± 28.3%, after forward and reverse polarization, respectively (**Appendix 5.15** and **Table 5.1/5.2**). Detailed experimental scheme for **Figure 5.5** is shown in **Appendix 5.16**.

As can be seen from **Figures 5.5c**, **d**, polarization also shifts the photocurrent onset potential as follows: -0.36 V (Forward P.) < -0.21 (No P.) < -0.12 V (Reverse P.) for the respective films. This shows that the polarization also affects the photovoltage of the Ta/$BaTiO_3$/liquid junction. These results agree with previous observations of anomalous photovoltages in ferroelectric $BaTiO_3$ thin films, [7-8] and suggest that the PEC behavior of $BaTiO_3$ nanocrystals is controlled by a ferroelectric effect.

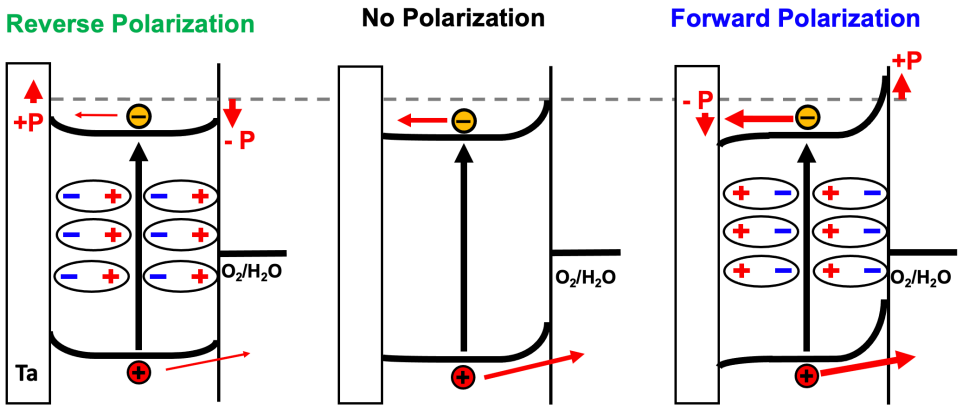

Figure 5.6. Effect of FE polarization on the photoelectrochemistry of $BaTiO_3$ /liquid contacts. +P and -P are the band energy shifts due to electric polarization.

The photoelectrochemical results can be explained with the energy diagram in **Figure 5.6** for the Ta/$BaTiO_3$/H_2O configuration. Without applied polarization, the $BaTiO_3$ crystals forms a depletion layer at the solid-liquid interface and a near ohmic contact with the tantalum substrate. The depletion layer promotes hole transfer into the solution (photoanode behavior) and allows electrons to transfer into the Ta substrate. Electric polarization induces a ferroelectric (FE) dipole in $BaTiO_3$ that modifies the band bending near the particle interfaces (inside the material the FE dipoles cancel out). Forward polarization raises the solid-liquid band edge position by an amount P, thereby increasing the potential drop across the depletion layer, and promoting photohole transfer into the liquid (photoanode behavior). The FE dipole also lowers the band

edge at the Ta/$BaTiO_3$ contact by the same amount P, to improve photoelectron transfer into the Ta substrate (photoanode behavior). Reverse polarization has the opposite effects (diminishes photoanode behavior). The size of the FE induced band shift P can be estimated from the photocurrent onset shift E_{on} (Polarized)-E_{on} (Non-Polarized) in the PEC scans in **Figure 5.5**. Accordingly, P = 0.15 eV for Forward polarization and 0.09 eV for Reverse polarization.

To verify the model, Vibrating Kelvin Probe Surface photovoltage spectra (VKP-SPS) were recorded on $BaTiO_3$ particle films in vacuum. VKP-SPS measures the contact potential difference (CPD) of a sample with a commercially available vibrating Kelvin probe (Besocke Delta Phi, see insert in **Figure 5.7**). Illumination through the semi-transparent probe disturbs the distribution of the charge carriers in the sample and produces a surface photovoltage signal SPV = CPD_{light} - CPD_{dark}. The sign and size of the SPV signal provides information about the direction of charge separation and the driving force. [47-48]

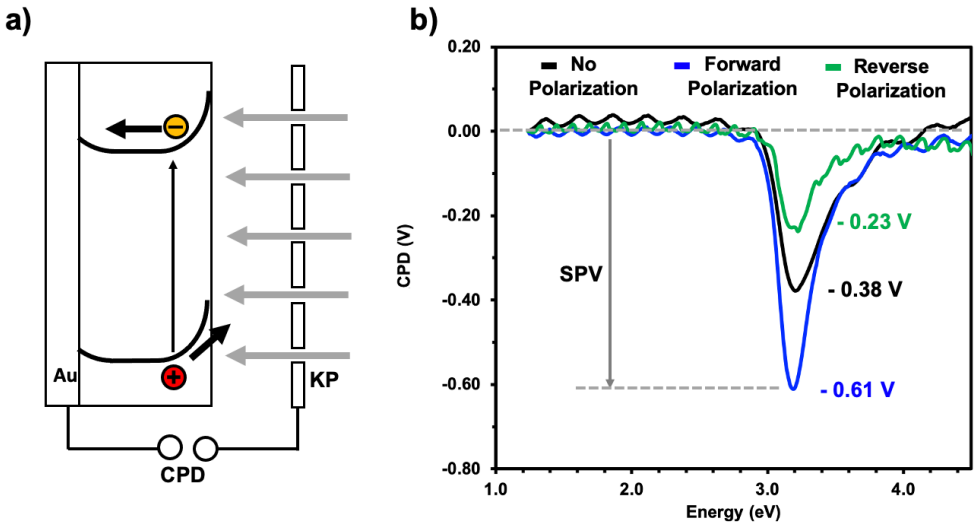

Figure 5.7. a) Surface photovoltage (SPV) measurement geometry and b) SPV spectra of $BaTiO_3$ particle film on gold substrate in vacuum, before and after electric polarization in a 52.8 kV/cm field. For detailed measurement configuration see **Appendix 5.17**.

As can be seen from **Figure 5.7**, all $BaTiO_3$ particle films yield negative SPV signals at 3.2 eV, near the optical band gap of the material. This confirms that the SPV signal is generated by charge carrier movement in the depletion layer at the surface, as shown in **Figure 5.7a**. The SPV signal (-0.61 V) is largest for the forward polarized $BaTiO_3$ film, followed by the non-polarized film (-0.38 V) and the reverse polarized film (-0.23 V). This agrees with the photocurrent trend in **Figure 5.5**. It confirms that photochemical charge transfer in $BaTiO_3$ is predominantly controlled by the surface FE dipoles shown in **Figure 5.6**.

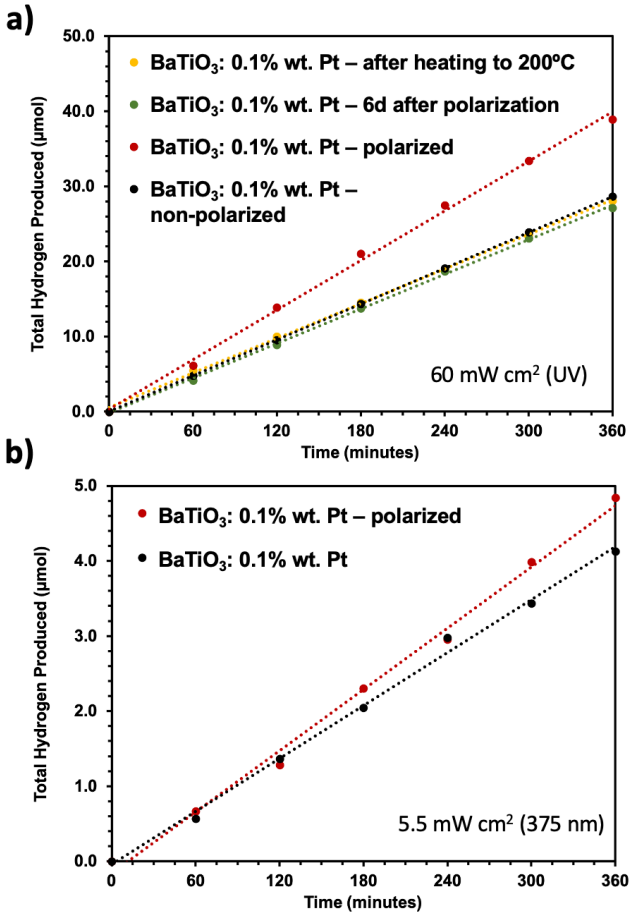

Figure 5.8. H_2 evolution from 100 mg of 0.1%wt Pt – loaded $BaTiO_3$ in 100 mL of 20% (vol) aqueous methanol under a) 60 mW cm^{-2} UV light irradiation, b) under 375 nm LED illumination (5.5 mW cm^{-2};

illumination area is 2.01 cm^2). The Apparent Quantum Yield (AQY) is 1.12 % for the non-polarized and 1.29 % for the polarized material.

To test if the FE polarization can be used to also control photocatalytic hydrogen evolution with a $BaTiO_3$ particle suspension, polarization experiments were carried out on the $BaTiO_3$ powder. For this purpose, 100 mg of dry $BaTiO_3$ powder was sandwiched between two mica crystals and subjected to a 6.32 kV cm^{-1} electric field for 1 h, as shown in **Appendix 5.18b**. Platinum cocatalyst was then deposited onto the freshly polarized $BaTiO_3$ powder, by irradiating it with UV light in the presence of 0.1% mass (based on $BaTiO_3$ weight) hexachloroplatinic acid and 20% aqueous methanol as sacrificial electron donor. Platinum photodeposition began immediately as indicated by a color change of the suspension from white to slightly grey.

Illumination was continued for 6 hours under 60 mW cm^{-2} UV light to observe H_2 evolution at a constant rate of 6.49 μmol h^{-1} (**Figure 5.8a**). Under 375 nm LED illumination, the rate was 0.81 μmol h^{-1}, corresponding to an apparent quantum yield (AQY) of 1.29% (**Figure 5.8b**). In comparison, the H_2 production rate of a $Pt/BaTiO_3$ sample prepared without prior electric polarization, was only 4.77 μmol h^{-1} (AQY of 1.12 % at 375 nm, rate = 0.69 μmol h^{-1}). These observations were reproducible in three separate batches of $BaTiO_3$ (**Appendix 5.19** and **Table 5.3**). Based on this data, electric polarization enhances the H_2 evolution activity 1.53 times compared to a non-polarized sample. While the absolute activities are low, they are comparable to an earlier report. [19]

Lastly, to determine the effect of heat treatment on the FE polarization, another fresh sample of polarized $BaTiO_3$ was heated to 200°C in air for 20 min prior to Pt photodeposition. As expected, the annealed $BaTiO_3$ shows a hydrogen production rate of 4.68 μmol h^{-1}, almost identical to the non-polarized material (**Figure**

5.8a). Overall, the results in **Figure 5.8** confirm that the photocatalytic activity can be aided by electric polarization and removed by annealing above the Curie temperature, as expected from the theory. Detailed experimental scheme for H_2 evolution particle suspension system is shown in **Appendix 5.20**.

Because the amount of photodeposited platinum in the $Pt/BaTiO_3$ photocatalyst particles was too small for imaging, silver photolabeling was employed to determine the effect of the FE on charge separation in the $BaTiO_3$ particles. [33] For the experiment, $BaTiO_3$ powders were suspended in 0.1 M $AgNO_3$ solution and illuminated with 10 mW cm^{-2} UV light for 2 minutes. Photodeposition of silver occurred over the course of seconds, as indicated by a grey color appearance of the suspension. Particles were removed, washed and then imaged by SEM.

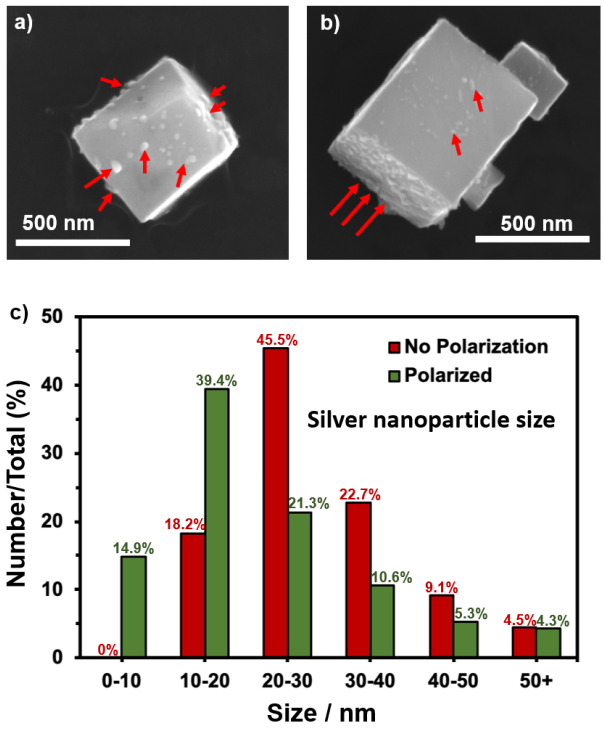

Figure 5.9. SEM images of $Ag/BaTiO_3$ after photodeposition of 1% wt. Ag from $AgNO_3$ in 20% aqueous methanol suspension with 10 mW cm^{-2} UV light irradiation in 2 minutes. a) Non-polarized $BaTiO_3$ particles. b) $BaTiO_3$ particles polarized at 6.32 kV cm^{-1} for 1 hour. c) Ag nanoparticle size distribution from SEM.

As can be seen in **Figure 5.9**, polarization changes both the sizes and locations of the photodeposited silver particles. For non-polarized $BaTiO_3$, silver particles are 28.8 ± 10.6 nm (n = 44) in size and grow randomly on all facets of the $BaTiO_3$ crystals (see also **Appendix 5.21**). For polarized $BaTiO_3$, on the other hand, the silver particles are smaller (22.5 ± 14.4 nm, n = 94) and located predominantly on the (001) facets.

These observations can be explained with the model in **Figure 5.10**. $BaTiO_3$ nanocrystals that were polarized along the c-axis (the axis of polarization) are expected to shift their bands as in **Figure 5.6**, allowing for accumulation of holes and electrons on opposing (001) facets. This explains the observation of increased H_2 evolution activity in **Figure 5.8** and the facet-selective silver deposition in **Figure 5.9**. The smaller size and greater number of (001) facet photodeposited Ag particles can be understood based on the Nucleation Theory. [49] The more reducing the electrochemical potential, the smaller the critical nucleation radius, and the smaller and more numerous the Ag particles. Non-polarized $BaTiO_3$ particles, on the other hand, do not have designated electron accumulation site and therefore the Ag particles are larger and fewer. Because the ferroelectric Ti^{4+} displacement in $BaTiO_3$ occurs only along the c-axis (**Figure 5.1**), particles exposed to an electric field along the a or b axis cannot develop a FE polarization. These particles will behave like $BaTiO_3$ particles that were never exposed to an electric field, or like particles that were heated to above their Curie temperature. The non-polarized particles may still have FE domains, but their size is smaller and the dipoles in adjacent domains cancel each other, resulting in a net zero polarization. This explains the lower proton reduction rate and the lower facet selectivity for Ag deposition.

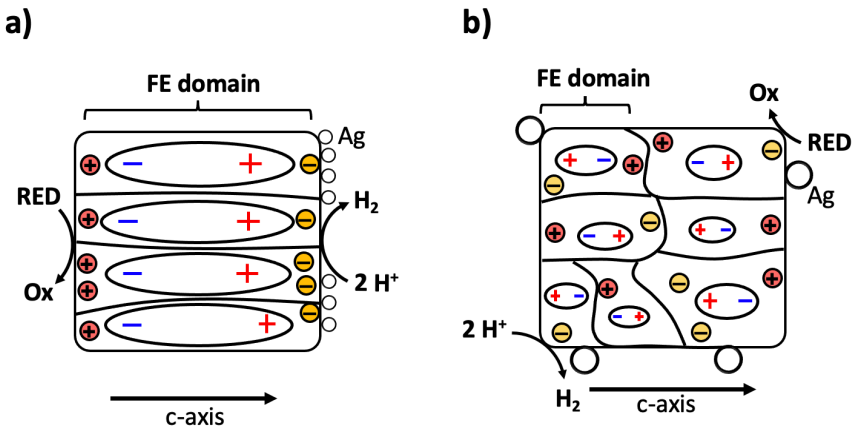

Figure 5.10. FE domain model for $BaTiO_3$ particles. a) large, oriented FE domains form after electric polarization along the c-axis. Increased FE domain size improves photocatalytic H_2 evolution activity / photochemical silver deposition. b) small, non-oriented FE domains form after electric field polarization perpendicular to the c-axis, or when particles are heated to above their Curie temperature T_C.

The model in **Figure 5.10** also explains the relatively modest increase in water oxidation and H_2 evolution activity after electric field exposure. First of all, the $BaTiO_3$ nanocrystals are small (average 242 nm), which limits the number and the size of oriented FE domains and the corresponding photovoltage from them. [7, 14] Furthermore, because the $BaTiO_3$ crystals are randomly oriented in the electric field, only up to 33% of them (particles with the c-axis aligned with the field) can develop a polarization. This limits the overall FE enhancement that can be expected in the sample. The greater activity increase (factor of 2) seen for the $BaTiO_3$ photoelectrodes is attributed to the higher electric field (52.8 kV cm^{-1}) acting on the thinner film compared to the powdered sample (6.32 kV cm^{-1}). Overall, the models in **Figure 5.6** and **Figure 5.10** provide an explanation for the observed reactivity trends in $BaTiO_3$ films and Pt/$BaTiO_3$ photocatalysts.

Lastly, to evaluate the lifetime of the polarization, repeat PEC measurements were conducted 3 and 6 days after the initial polarization (**Appendix 5.22**). The data shows that the 98 % of the polarization enhancement

(100% of the suppression) is retained in samples stored in ambient conditions for 3 days. However, after 6 days the effect disappears completely and the photocurrent of both Forward and Reverse polarized samples returns to 82% of the value for the non-polarized samples. The detailed reasons for the quenching are not clear, although we hypothesize that the small size of the $BaTiO_3$ nanocrystals (diameter of 242 nm) restricts the size and stability of the FE domains. In $BaTiO_3$ single crystals, FE domains can exceed 15 μm in size, [33] while the lower size limit for FE domains is seen in 5 nm $BaTiO_3$ films. [50] Future studies on the size-dependence of the FE polarization in $BaTiO_3$ crystals will bring further insight into this issue.

5.3 Conclusion

In summary, we demonstrate that prior electric polarization controls the photoelectrochemical water oxidation ability and photovoltage of nanosized tetragonal $BaTiO_3$ single crystals and their photocatalytic H_2 evolution activity in aqueous methanol. Both, activity enhancement and reduction can be observed, depending on the polarity of the applied electric field. Heating the material above the ferroelectric Curie temperature removes polarization effects and restores the original activity. The modulation of the photoelectrochemistry can be explained with FE dipole-induced changes of the potential drop in the depletion layer of the $BaTiO_3$-liquid and Ta/$BaTiO_3$ junctions. The FE dipole modifies the photovoltage of the junctions by +0.15 V or -0.09 V, depending on the electric field direction during polarization. This increases the photocurrent by a factor of 2.0 ± 0.21 or diminishes it by a factor of 3.5 ± 0.98 respectively, relative to a non-polarized film, and it raises the photocatalytic H_2 evolution activity 1.53 times. Fundamentally, the size of the observed effect is limited by the random orientation of the $BaTiO_3$ nanocrystals in the homogeneous electric field. Because the electric polarization in $BaTiO_3$ is restricted to its crystallographic c-axis (the easy axis), no more than one third of the nanocrystals can be polarized. The stability of the polarization is limited to 3 days, which is attributed to the small size of the nanocrystals.

Potentially, these problems may be overcome by growing $BaTiO_3$ films with preferred crystallographic orientation, and by synthesizing larger $BaTiO_3$ crystals which could support a greater number of FE domains.

5.4 Experimental Section

Barium hydroxide ($Ba(OH)_2$, 98 % Acros Organics),), titanium (IV) oxide (Aeroxide P25, Acros Organics), potassium hydroxide (KOH 99.9 %, Sigma Aldrich). Water was purified to 18 MΩcm resistivity using a Nano-pure system. Titanium (IV) chloride ($TiCl_4$, 99.9 % Acros Organics), anhydrous methanol (CH_3OH, 99.9% Alfa Aesar), gold-coated glass (Thermo Scientific), tantalum foil (99.95 % metal basis, Alfa Aesar), hydrofluoric acid (HF, 48-51 % solution in water, Acros Organics), muscovite mica (25 x 25 mm, thickness 0.26-0.31 mm, Electron Microscopy Sciences), sodium sulfate (Na_2SO_4, ≥ 99.0 % Sigma Aldrich), hexachloroplatinate (IV) hexahydrate (99.9 %, Alfa Aesar).

Hydrothermal Synthesis of Barium Titanate Nanoparticles

Barium titanate nanoparticles were synthesized with a hydrothermal reaction where 15 mmol (4.7319 g) barium hydroxide octahydrate, 14.3 mmol (1.14 g) P25 titanium dioxide, 0.30 mol (16.83 g) potassium hydroxide, and 30 mL of nanopure water are mixed and transferred into a 45 mL PTFE lined autoclave. The autoclave is then sealed and heated in an oven at 180ºC for 72 hours. After cooling to room temperature, the white precipitate is washed with 1.0 M hydrochloric acid three times and then water to remove unreacted starting materials and dried in air. Yield = 63 %.

Particle Film Fabrication

Barium titanate particle films were obtained by drop coating 80 μL of 24 mg/mL $BaTiO_3$ aqueous suspension onto either a pre-cleaned gold substrate or pre-cleaned tantalum substrate covered with polyester masking tape (hole diameter = 0.8 cm). The $BaTiO_3$ aqueous suspension was sonicated for 10 minutes prior to drop coating. Gold substrates were cleaned in 30% hydrogen peroxide and potassium hydroxide solution for 1 minute, then acetone for 30 minutes, and washed with nanopure water and dried in air. The tantalum substrate was cleaned with 10 % hydrofluoric acid aqueous solution for 10 minutes (Caution: Toxic, Corrosive) and then washed with anhydrous methanol. For the gold substrate, the drop-coated film was left to dry in air in the dark overnight before being annealed in argon at 450ºC for 120 minutes, with a ramp rate of 2ºC/min. The obtained film thickness is approximately 3.0 μm. For the tantalum substrate, necking treatment was accomplished by adding 5 x 10 μL of 20 mM $TiCl_4$ in anhydrous methanol, followed by 30 min drying in air before annealing in argon at 600ºC for 120 minutes, at a ramp rate of 2ºC/min.

Diffuse Reflectance Spectroscopy

Kubelka-Munk optical spectra were recorded on a barium titanate powder pellet (3 g) using a Thermo Scientific Evolution 220 Spectrometer equipped with an integrating sphere. A barium sulfate standard was used to obtain a diffuse reflectance background.

Electric Polarization

Electrical polarization of particle films and powders was accomplished as shown in **Appendix 5.18**. The particle film was sandwiched between two 2 x 4 cm^2 gold coated glass slides covered by Muscovite mica crystals (≤65 μm thick) for electrical insulation. The sandwich was then placed inside a quartz tube with continuous argon gas purging (1.0 L min^{-1}) and connected to a 359 V DC applied voltage source for one hour at room temperature. Voltage was measured with a digital multimeter and using a voltage divider consisting of 0.499 MΩ and 49.3 kΩ resistors in series. Based on the electrode distance (0.0003 cm + 0.0065

cm), the electric field for polarization was 52.8 kV cm^{-1}. The high DC voltage was produced with a DC-HVDC Converter, FS Series, XP Power ®. Heating was performed in air for 30 minutes at 200ºC, above the Curie Temperature (110-120ºC), by placing samples into a preheated oven.

Photoelectrochemistry Measurements

Photoelectrochemistry measurements were conducted using a Gamry Reference 600 Potentiostat connected to a three-electrode system consisting of the working electrode, a calomel reference electrode (3.5 M KCl), and a Pt counter electrode in 0.50 M Na_2SO_4 aqueous electrolyte solution (pH = 5.95). Chopped light linear sweep scans were accomplished with UV-light illumination from a 300W Xe lamp source with an intensity of 60 mW cm^{-2} at the sample (**Appendix 5.12**). The chopped light scan interval was 5 seconds with scan rate of 10 mV/s and scan step of 1 mV. Calibration was performed with $K_{3/4}[Fe(CN)_6]$ and using fluorine doped tin oxide (FTO) as the working electrode. All potentials were converted to RHE where RHE = NHE + pH x 0.059V. The one-hour PEC experiment in **Appendix 5.14** was performed using light from a 200 W Hg lamp.

Surface Photovoltage Spectroscopy

Surface Photovoltage Spectroscopy (SPS) measurements were accomplished using a vibrating gold mesh Kelvin probe (Delta PHI Besocke) mounted inside a vacuum chamber held at 1.0 x 10^{-4} bar. The sample was mounted as shown in **Appendix 5.17** with an alligator clip back contact and the Kelvin probe was positioned ~1 mm over the film surface. Samples were left to equilibrate until a stable baseline is obtained. The CPD signal was recorded in the 10,000 – 40,000 cm^{-1} interval using 100 cm^{-1} illumination increments every 5 seconds. A 300 W Xe lamp served as the light source.

Photochemical Hydrogen Evolution

Photochemical H_2 evolution measurements were accomplished by dispersing 100 mg of 0.1% wt. $Pt/BaTiO_3$ photocatalyst in 100 mL of 20 % aqueous methanol solution at neutral pH. Irradiation was performed in a round bottom quartz flask using a 300 W Xe arc lamp with UV intensity at the flask of 60 mW cm^{-2}. The quartz flask was connected to a gas chromatograph (Varian 3800) by an air-tight circulation system that allowed the sample flask to be evacuated and purged with argon before taking measurements. Photodeposition of the platinum co-catalyst was performed by adding chloroplatinic acid to the reaction solution (0.1 mg in 100 mL) and irradiated with UV light for 10 minutes to ensure complete deposition. Data collection was performed every hour over a 6-hour period. Electric polarization experiments were performed in the sequence shown in **Appendix 5.20**.

Silver Photodeposition

Photochemical silver deposition was accomplished by adding 1% weight $AgNO_3$ to a 20 mg $BaTiO_3$ 20% aqueous methanol suspension (20 mL) and by illuminating with UV light (Xe lamp, 20 mW cm^{-2}) for 2 minutes.

5.5 Appendix

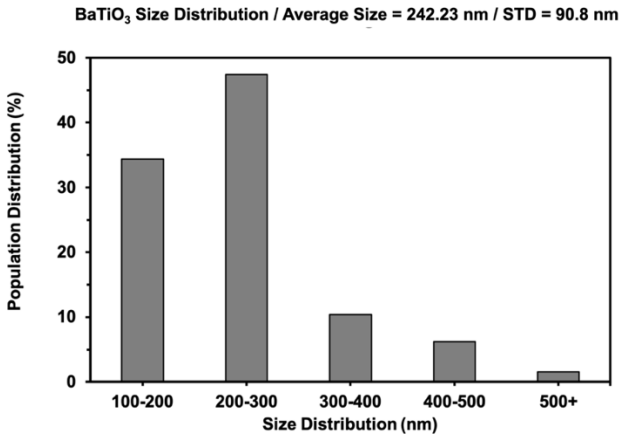

Figure 5.11. Size distribution of $BaTiO_3$ particles obtained from hydrothermal synthesis.

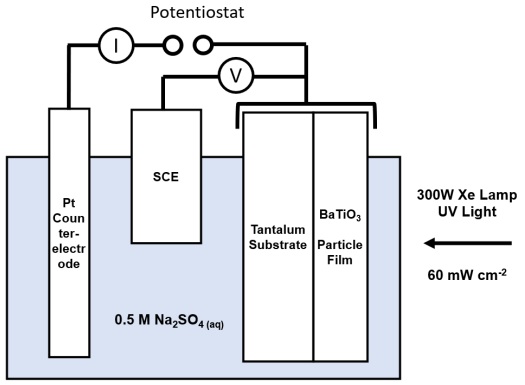

Figure 5.12. Photoelectrochemistry scheme in a three-neck flask system in quartz flask.

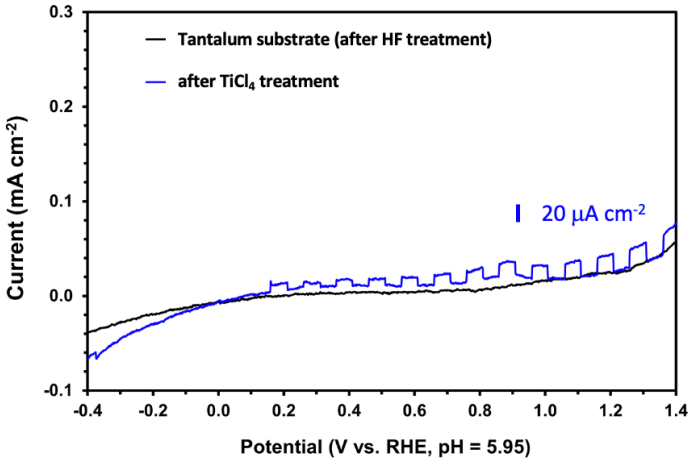

Figure 5.13. a) IV scan for tantalum substrate after 10% HF wash and after $TiCl_4$ treatment in 0.50 M Na_2SO_4 aqueous solution under 60 mW cm^{-2} chopped UV illumination. Voltametric scans were conducted from positive to negative applied potential.

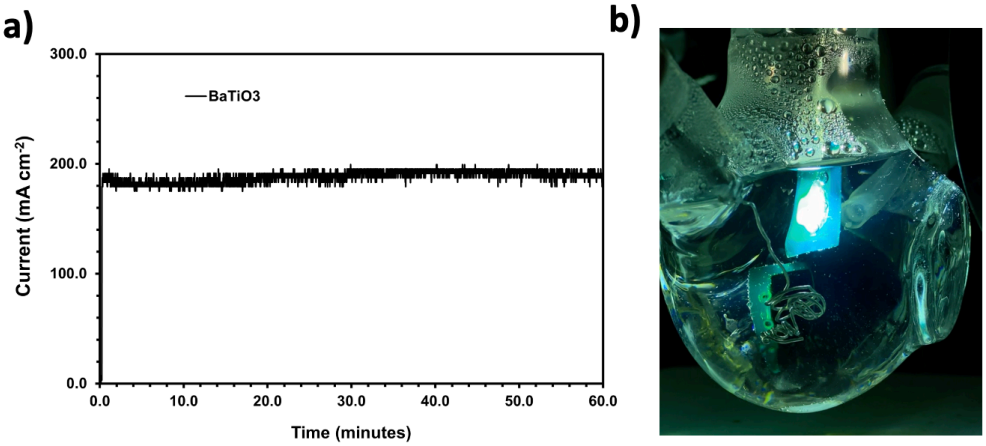

Figure 5.14. a) Photoelectrochemical scans of non-polarized Ta/$BaTiO_3$ film under 1.27 V RHE applied bias in 0.50 M Na_2SO_4 aqueous solution (pH = 5.95) with UV light illumination from a 200 W Hg lamp with 330 nm long pass filter. b) Gas bubbles from Ta/$BaTiO_3$ film under the same conditions. Movie in Supporting Information.

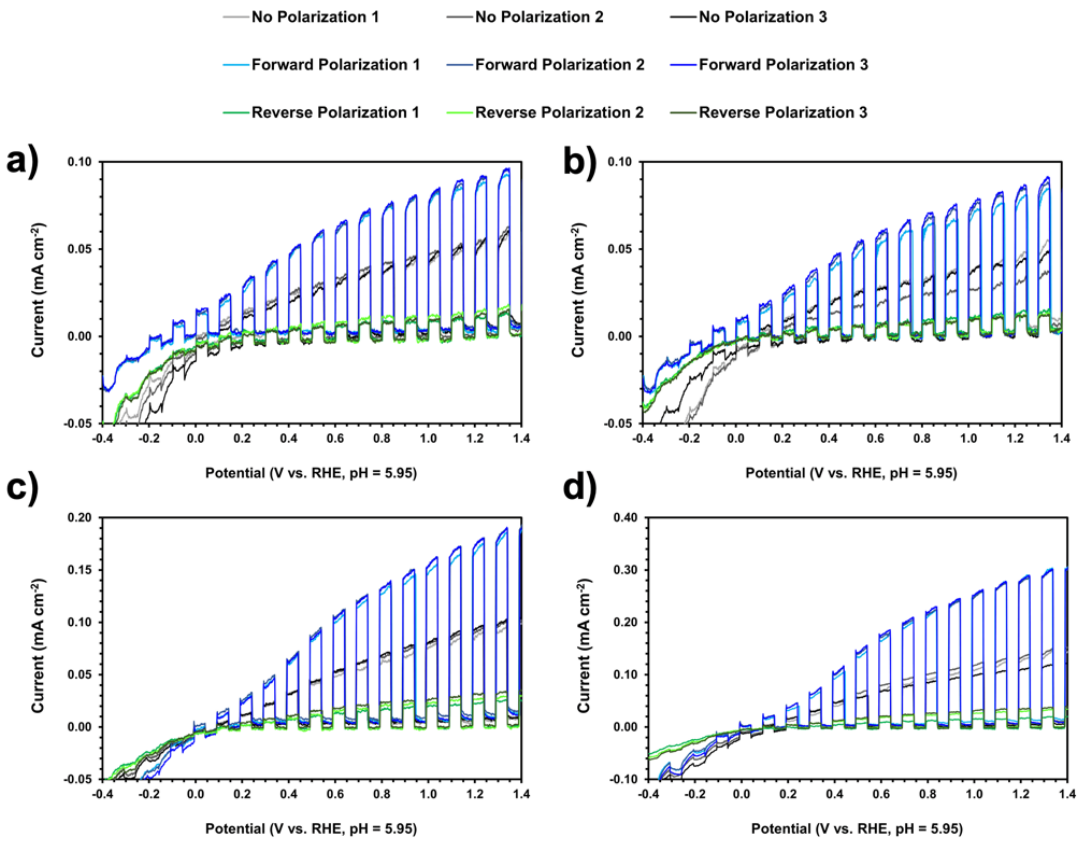

Figure 5.15. PEC for 80 µL drop-coated 24 mg/mL $BaTiO_3$ particle films, prepared as described in experimental section. Condition: 0.50 M Na_2SO_4 aqueous solution under UV illumination (60 mW cm^{-2}) with scan direction from negative to positive potential and 5 s light on/off intervals with constant stirring. a) Film 1 b) Film 2 c) Film 3 d) Film 4.

Table 5.1. Statistical Error analysis of photocurrent data for each film samples corresponding to **Appendix 5.15**.

Film 1		Photocurrent (mA cm^{-2}) at 1.23 V vs RHE	Mean (mA cm^{-2})	Standard Deviation (mA cm^{-2}, %)
No Polarization	Trial 1	0.052	0.053	0.001, 1.89
	Trial 2	0.053		
	Trial 3	0.053		
Forward Polarization	Trial 1	0.087	0.090	0.002, 2.22
	Trial 2	0.090		
	Trial 3	0.092		
Reverse Polarization	Trial 1	0.011	0.013	0.002, 15.4
	Trial 2	0.014		
	Trial 3	0.013		
Film 2		Photocurrent (mA cm^{-2}) at 1.23 V vs RHE	Mean (mA cm^{-2})	Standard Deviation (mA cm^{-2}, %)
No Polarization	Trial 1	0.046	0.040	0.008, 20.0
	Trial 2	0.031		
	Trial 3	0.043		
Forward Polarization	Trial 1	0.080	0.083	0.003, 3.61
	Trial 2	0.084		
	Trial 3	0.085		
Reverse Polarization	Trial 1	0.015	0.012	0.002, 16.7
	Trial 2	0.011		
	Trial 3	0.011		
Film 3		Photocurrent (mA cm^{-2}) at 1.23 V vs RHE	Mean (mA cm^{-2})	Standard Deviation (mA cm^{-2}, %)
No Polarization	Trial 1	0.090	0.094	0.003, 3.19
	Trial 2	0.094		
	Trial 3	0.097		
Forward Polarization	Trial 1	0.175	0.178	0.002, 1.12
	Trial 2	0.179		
	Trial 3	0.179		
Reverse Polarization	Trial 1	0.023	0.027	0.004, 14.8
	Trial 2	0.027		
	Trial 3	0.032		
Film 4		Photocurrent (mA cm^{-2}) at 1.23 V vs RHE	Mean (mA cm^{-2})	Standard Deviation (mA cm^{-2}, %)
No Polarization	Trial 1	0.132	0.127	0.014, 11.0
	Trial 2	0.137		
	Trial 3	0.112		
Forward Polarization	Trial 1	0.289	0.288	0.002, 0.69
	Trial 2	0.285		
	Trial 3	0.289		
Reverse Polarization	Trial 1	0.018	0.028	0.009, 32.11
	Trial 2	0.031		
	Trial 3	0.035		
Film Figure 4.5				
No Polarization		0.141		
Forward Polarization		0.276		
Reverse Polarization		0.073		

Table 5.2. Statistical Error analysis of photocurrent across film samples corresponding to **Appendix 5.15**.

	Film 1	Film 2	Film 3	Film 4	Film Figure 4.5	Mean	Standard Deviation (absolute, %)
Photocurrent Change Factor at 1.23 V vs RHE, % from Non- to FORWARD Polarized	1.70	2.08	1.89	2.26	1.95	1.97	0.21, 10.7
Photocurrent Change Factor at 1.23 V vs RHE, % from Non- to REVERSE Polarized	4.08	3.33	3.48	4.50	1.93	3.46	0.98, 28.3

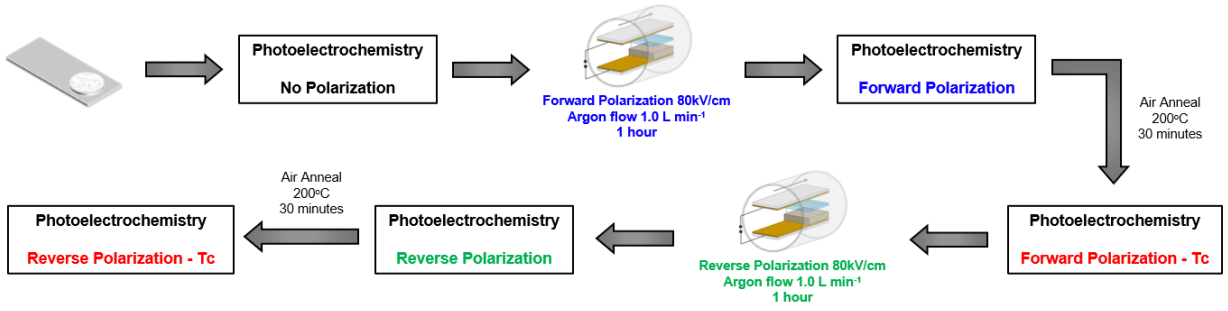

Figure 5.16. Process flow chart for electric polarization and PEC testing of $BaTiO_3$ particle film. PEC data is shown in **Figure 5.5**.

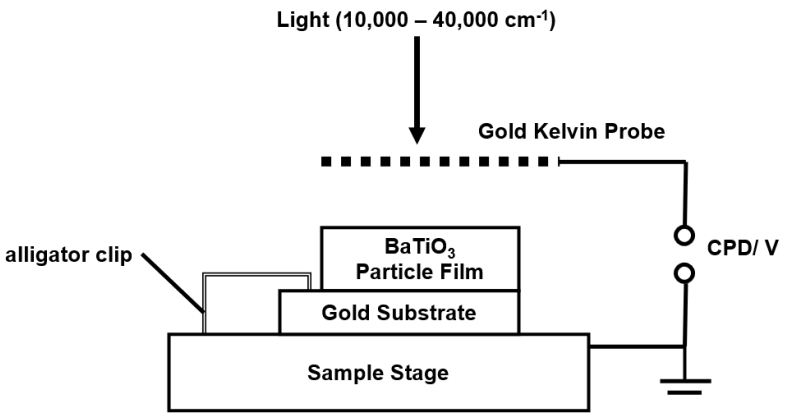

Figure 5.17. Surface photovoltage spectroscopy scheme under vacuum.

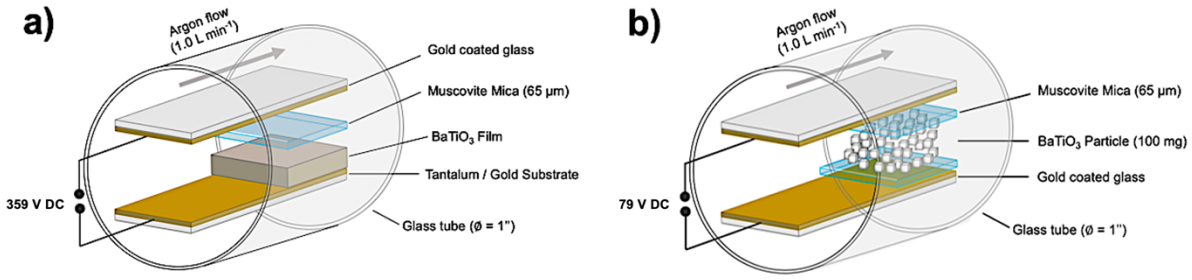

Figure 5.18. Polarization scheme of $BaTiO_3$ a) particle film and b) particles. For forward polarization, the $BaTiO_3$ electrode was contacted with the negative lead of the electric power supply. For reverse polarization, the $BaTiO_3$ electrode was contacted with the positive lead of the electric power supply. For powder polarization, there is no forward or reverse polarization since the direction are relative to how the powders are oriented.

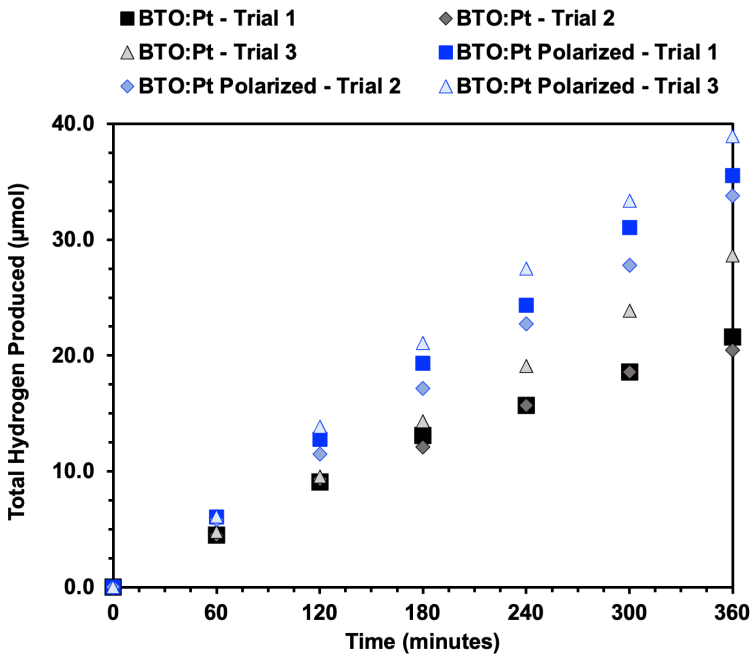

Figure 5.19. H_2 evolution from three trials of 100 mg $BaTiO_3$:Pt 0.1 % (wt) with or without polarization in 100 mL aqueous 20 % methanol under 60 mW cm^{-2} UV light irradiation (trial 3 corresponds to the data shown in **Figure 5.8** in main text).

Table 5.3. H_2 evolution rate (µmol h^{-1}) statistic calculations corresponding to the data in **Appendix 5.19**.

	$BaTiO_3$: Pt 0.1% wt	**$BaTiO_3$: Pt 0.1% wt - polarized**
Trial 1 (µmol H_2 h^{-1})	3.60	5.92
Trial 2 (µmol H_2 h^{-1})	3.41	5.63
Trial 3 (Figure 5.8) (µmol H_2 h^{-1})	4.77	6.49
Mean (µmol H_2 h^{-1})	3.93	6.01
Standard Deviation (µmol H_2 h^{-1}, %)	0.74, 18.8%	0.44, 7.3%

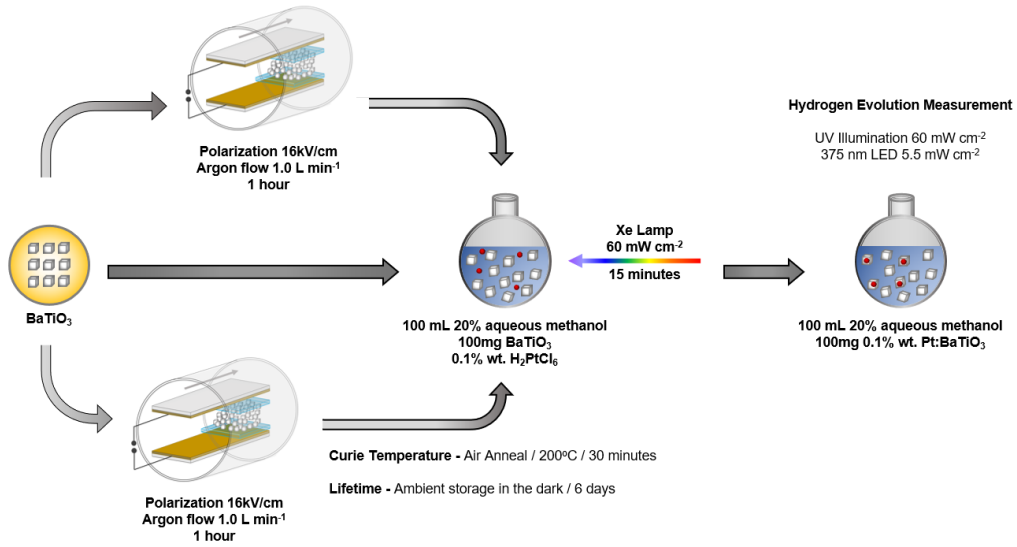

Figure 5.20. Process flow chart for electric polarization and photocatalytic testing of $BaTiO_3$. The photocatalytic H_2 evolution results are shown in **Figure 5.8**.

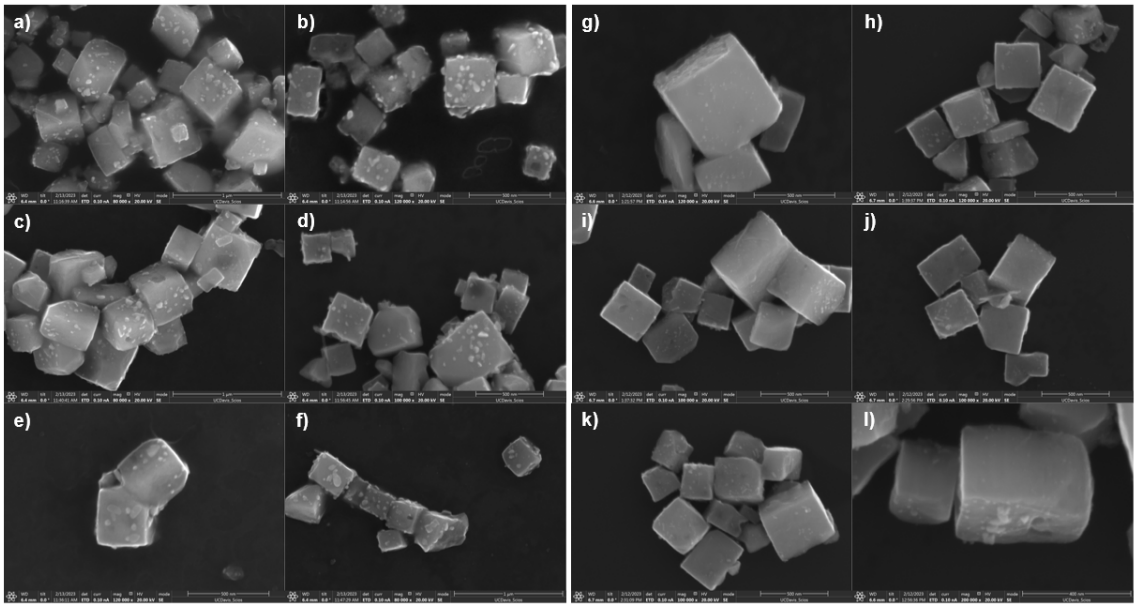

Figure 5.21. SEM images of a-f) silver-deposited $BaTiO_3$ particles. g-l) silver-deposited $BaTiO_3$ particles after polarization at 6.32 kV cm^{-1} for 1 hour.

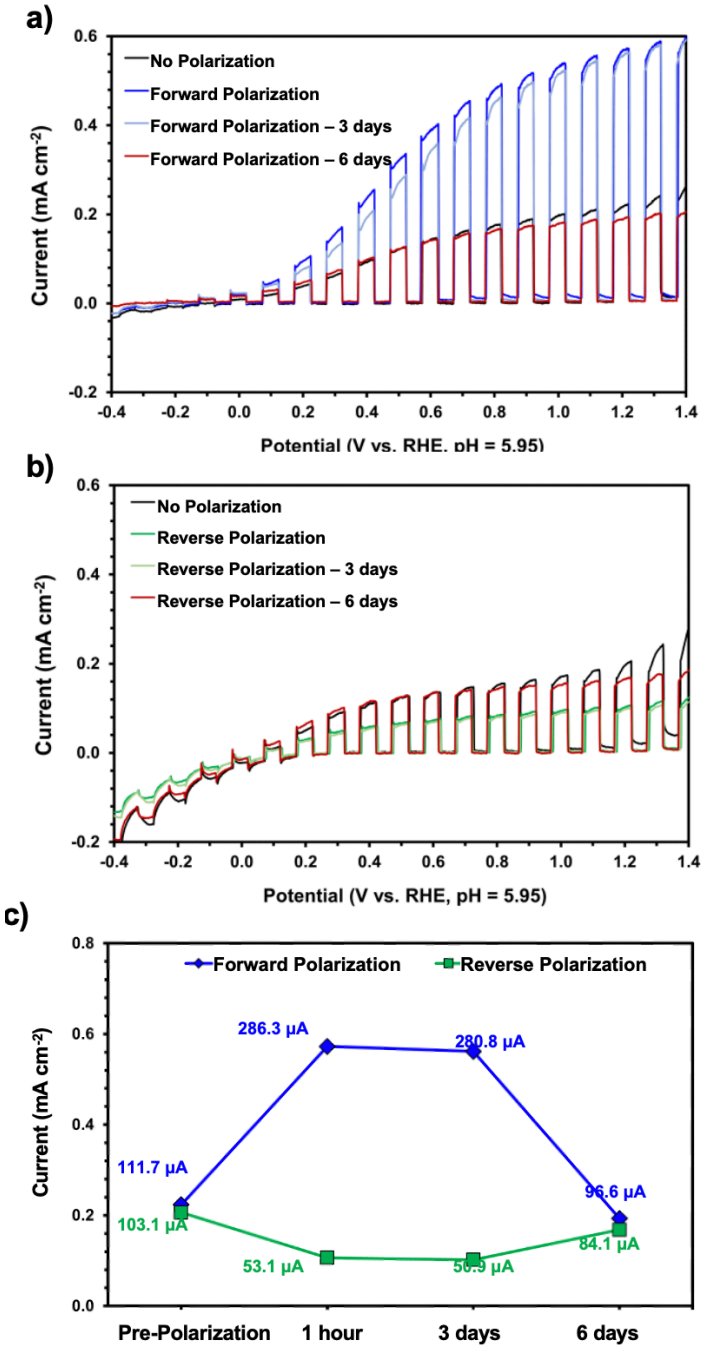

Figure 5.22. Photocurrent 1 hour, 3 days, and 6 days after initial polarization. a) Forward polarization. b) Reverse polarization. c) Photocurrent change over time. Samples were stored in air and in the dark.

5.6 References

1. Valasek J.; *Physical Review*, **1921**, *17* (4), 475-481.

2. Martin L. W., Rappe, A. M.; *Nature Reviews Materials*, **2016**, *2*, 16087.

3. Ahn C. H., Rabe K. M., Triscone, J.-M.; *Science*, **2004**, *303* (5657), 488-491.

4. Neaton J. B., Ederer C., Waghmare, U. V., Spaldin, N. A., Rabe, K. M.; *Physical Review B*, **2005**, *71* (1), 014113.

5. Merz W. J.; *Physical Review*, **1954**, *95* (3), 690-698.

6. Merz W. J.; *Physical Review*, **1953**, *91* (3), 513-517.

7. Käppler W., Arlt G.; *Physica Status Solidi (A)*, **1981**, *63* (2), 475-480.

8. Brody P. S.; *Solid State Communications,* **1973**, *12* (7), 673-676.

9. Butler K. T., Frost J. M., Walsh A.; *Energy and Environmental Science*, **2015**, *8* (3), 838-848.

10. Lopez-Varo P., Bertoluzzi L., Bisquert J., Alexe M., Coll M., Huang J., Jimenez-Tejada J. A., Kirchartz T., Nechache R., Rosei F., Yuan Y.; *Physics Reports*, **2016**, *653*, 1-40.

11. Yuan G.-L., Wang J.; *Applied Physics Letters*, **2009**, *95* (25), 252904.

12. Nechache R., Harnagea C., Li S., Cardenas L., Huang W., Chakrabartty J., Rosei F.; *Nature* Photonics, **2015**, *9* (1), 61-67.

13. Fan D., Zhu J., Wang X., Wang S., Liu Y., Chen R., Feng Z., Fan F., Li C.; *ACS Applied Materials &* Interfaces, **2016**, *8* (22), 13857-13864.

14. Yang S. Y., Seidel J., Byrnes S. J., Shafer P., Yang C. H., Rossell M. D., Yu P., Chu Y. H., Scott J. F., Ager J. W., Martin L. W., Ramesh R.; *Nature Nanotechnology*, **2010**, *5* (2), 143-147.

15. Kutes Y., Ye L., Zhou Y., Pang S., Huey B. D., Padture N. P.; *The Journal of Physical Chemistry Letters*, **2014**, *5* (19), 3335-3339.

16. Li Y., Li J., Yang W. G., Wang X. D.; *Nanoscale Horizons*, **2020**, *5* (8), 1174-1187.

17. Yu Y., Wang X.; *Advanced Materials*, **2018**, *30* (43), 1800154.

18. Takata T., Jiang J., Sakata Y., Nakabayashi M., Shibata N., Nandal V., Seki K., Hisatomi T., Domen K.; *Nature*, **2020**, *581* (7809), 411-414.

19. Maeda K.; *ACS Applied Materials &* Interfaces, **2014**, *6* (3), 2167-2173.

20. Li L., Salvador, P. A., Rohrer G. S.; *Nanoscale*, **2014**, *6* (1), 24-42.

21. Khan M. A., Nadeem M. A., Idriss H.; *Surface Science Reports*, **2016**, *71* (1), 1-31.

22. Inoue Y., Okamura M., Sato K.; *Journal of Physical Chemistry C*, **1985**, *89* (24), 5184-5187.

23. Deng J., Banerjee S., Mohapatra S. K., Smith Y. R., Misra M.; *Journal of Fundamentals of Renewable Energy and Applications*, **2011**, *1*, 10.

24. Senthilkumar P., Jency D. A., Kavinkumar T., Dhayanithi D., Dhanuskodi S., Umadevi M., Manivannan S., Giridharan N. V., Thiagarajan V., Sriramkumar M., Jothivenkatachalam K.; *ACS Sustainable Chemistry & Engineering*, **2019**, *7* (14), 12032-12043.

25. Cao D., Wang Z.; Nasori; Wen L., Mi Y., Lei Y.; *Angewandte Chemie*, **2014**, *126* (41), 11207-11211.

26. Cui Y., Briscoe J., Dunn S.; *Chemistry of Materials*, **2013**, *25* (21), 4215-4223.

27. Osterloh F. E.; *ACS Energy Letters*; **2017**, *2*, 445-453.

28. Bae S., Kim S., Lee S., Choi W.; *Catalysis Today*, **2014**, *224*, 21-28.

29. Yang W., Yu Y., Starr M. B., Yin X., Li Z., Kvit A., Wang S., Zhao P., Wang X.; *Nano Lett*ers, **2015**, *15* (11), 7574-7580.

30. Park S., Lee C. W., Kang M.-G., Kim S., Kim H. J., Kwon J. E., Park S. Y., Kang C.-Y., Hong K. S., Nam K. T.; *Physical Chemistry Chemical Physics*, **2014**, *16* (22), 10408-10413.

31. Fu Q., Wang X., Li C., Sui Y., Han Y., Lv Z., Song B., Xu P.; *RSC Advances*, **2016**, *6* (110), 108883-108887.

32. Magnan H., Deleuze P. M., Brehin J., Plays T., Stanescu D., Flavell W. R., Silly M. G., Domenichini B., Barbier A.; *Journal of Physical Chemistry C*, **2020**, *124* (19), 10315-10323.

33. Giocondi J. L., Rohrer G. S.; *Chemistry of Materials*, **2001**, *13* (2), 241-242.

34. Giocondi J. L., Rohrer G. S.; *Journal of Physical Chemistrry B*, **2001**, *105* (35), 8275-8277.

35. Munprom R., Salvador P. A., Rohrer G. S.; *Journal of Materials Chemistry A*, **2016**, *4* (8), 2951-2959.

36. Zhang Y., Schultz A. M., Salvador P. A., Rohrer G. S.; *Journal of Materials Chemistry*, **2011**, *21* (12), 4168-4174.

37. Morris M. R., Pendlebury S. R., Hong J., Dunn S., Durrant J. R.; *Advanced Materials*, **2016**, *28* (33), 7123-7128.

38. Liu Y., Zhang M., Wang Z., He J., Zhang J., Ye S., Wang X., Li D., Yin H., Zhu Q., Jing H., Weng Y., Pan F., Chen R., Li C., Fan F.; *Nature Communications*, **2022**, *13* (1), 4245.

39. Assavachin S., Nail B. A., Goncalves R. V., Mulcahy J. R., Lloyd S. E., Osterloh F. E.; *Materials Advances*, **2020**, *1* (5), 1382-1389.

40. Tsumura T., Matsuoka K., Toyoda M.; *Journal of Materials Science & Technology*, **2010**, *26* (1), 33-38.

41. Evans H. T. Jr.; *Acta Crystallographica*, **1961**, *14* (10), 1019-1026.

42. Maruska H. P., Ghosh A. K.; *Solar Energy*, **1978**, *20* (6), 443-458.

43. Michaelson H. B.; Electron Work Function of the Elements. In CRC Handbook of Chemistry and Physics, *88* (Internet Version **2008**) ed.; Lide D. R., Ed. CRC Press/Taylor and Francis: Boca Raton, FL, **2008**.

44. Wang Z., Qi Y., Ding C., Fan D., Liu G., Zhao Y., Li C.; *Chemical Science*, **2016**, *7* (7), 4391-4399.

45. Shi C., Billinge S. J. L., Puma E., Bang S. H., Bean N. J. H., de Sugny J.-C., Gambee R. G., Haskell R. C., Hightower A., Monson T. C.; *Physical Review B*, **2018**, *98* (8), 085421.

46. Yoon K. H., Chung K. S.; *Journal of Applied Physics*, **1992**, *72* (12), 5743-5749.

47. Doughty R. M., Hodges B., Dominguez J., Han R., Zhao Z., Assavachin S., Osterloh F. E.; *The Journal of Physical Chemistry C*, **2020**, *124* (34), 18426-18435.

48. Doughty R. M., Chowdhury F. A., Mi Z., Osterloh F. E.; *The Journal of Chemical Physics*, **2020**, *153* (14), 144707.

49. Cao G.; Nanostructures and Nanomaterials: Synthesis, Properties and Applications. World Scientific Publishing Company: **2011**; p 63.

50. Kim Y. S., Kim D. H., Kim J. D., Chang Y. J., Noh T. W., Kong J. H., Char K., Park Y. D., Bu S. D., Yoon J.-G., Chung J.-S.; *Applied Physics Letters*, **2005**, *86* (10).